









HYDROSTATIC TESTING AND ANALYSIS  
OF GRAPHITE-EPOXY CYLINDERS

by

ZAN E. MILLER

B.S. Maritime Systems Engineering  
Texas A&M University  
(1984)

Submitted to the Department of Ocean Engineering  
in Partial Fulfillment of the  
Requirements for the Degrees of

NAVAL ENGINEER

and

MASTER OF SCIENCE IN MATERIALS SCIENCE AND ENGINEERING

at the

MASSACHUSETTS INSTITUTE OF TECHNOLOGY

June 1992

© Zan E. Miller, 1992. All rights reserved.

The author hereby grants to M.I.T. and to the U.S. Government  
permission to reproduce and distribute copies of this  
thesis document in whole or in part.

c 1



# HYDROSTATIC TESTING AND ANALYSIS OF GRAPHITE-EPOXY CYLINDERS

by

Zan E. Miller

Submitted to the Department of Ocean Engineering and the Department of Materials Science and Engineering on May 8, 1992, in partial fulfillment of the requirements for the Degrees of Naval Engineer and Master of Science in Materials Science and Engineering.

## ABSTRACT

An experimental study was conducted to investigate the use of advanced composite materials in unstiffened thin-walled cylindrical structures subjected to hydrostatic pressure. Specifically, graphite/epoxy was looked at for potential application for small submersible pressure hulls. The investigation concentrated on the fabrication, instrumentation, testing, and evaluation of several 12-ply graphite/epoxy cylinders of four different laminate configurations.

The test specimens were 18 inches long with radii of 2.76 inches, and each was instrumented with 8 circumferentially and 2 axially mounted strain gages. Data collected from the strain gages throughout the tests were used in a modified Southwell type analysis and an analysis to deduce the buckling mode shape. The Southwell analysis method was shown to have a valid applicability to the buckling of laminated fiber-reinforced composite pressure vessels. A method was developed to use the bending strain data at locations around the centerline of the specimen to deduce the number of circumferential buckling waves.

In addition, 1/2 inch ring specimen were cut from the excess ends of each specimen and tested under two-point compression, yielding information about the material properties of the laminates as fabricated.

The hydrostatic tests were designed to verify the results of an analytical and numerical study that was conducted to determine the optimal laminate stacking sequences for buckling considerations. The test results indicate that the classical solution method presented by R.M. Jones produced accurate predictions of buckling strengths and correct relative rankings of the different laminate types.

Thesis Supervisor: Professor John Dugundji  
Professor of Aeronautics and Astronautics



## ACKNOWLEDGEMENTS

Above all else, I give thanks to God for endowing me with perseverance, wisdom, and, most importantly, a sense of humor, without which this thesis would not have been possible.

Many people are deserving of thanks in connection with this thesis. I take this opportunity to express my appreciation to those most noteworthy.

o James Gorman, of Draper Labs, who granted me the opportunity to work on this project, for his support and advisement. His motivation and friendship enhanced my academic and professional development.

o Professor John Dugundji, who graciously served as my thesis advisor even though I was not enrolled in Course XVI, for his guidance and support that were a continual source of inspiration.

o To Jack Smith and the technicians in Draper's Thermal Lab for their assistance and patience with my questions and concerns.

o To my parents for instilling in me the confidence to strive for everything I want out of life. Their love, prayers and encouragement were strongly felt across those many miles.

o To my wife's parents for the innumerable things they did for us in the last few months, that enabled me to devote time to completing this research. Be assured that nothing went unnoticed or unappreciated.

An extra special thanks to my bride, Laurie, whose love, patience, and understanding through these, our newlywed months, were self-sacrificing gestures from a truly extraordinary person.

### DEDICATION:

To Adam, who has unfortunately been denied the father and son companionship we both long to share.



## TABLE OF CONTENTS

ABSTRACT . . . . .	2
ACKNOWLEDGEMENTS . . . . .	3
NOMENCLATURE . . . . .	6
LIST OF FIGURES . . . . .	7
1. INTRODUCTION . . . . .	9
1.1. Potential Benefits of Composite Pressure Hulls . . . . .	9
1.2. Purpose of Hydrostatic Testing . . . . .	14
2. ANALYTICAL BACKGROUND . . . . .	18
2.1. Compressive Strength of Composite Laminates . . . . .	20
2.2. Classical Laminate Theory . . . . .	27
2.3. Axisymmetric Compression of Cylindrical Shells . . . . .	31
2.4. Elastic Stability of Long Cylindrical Shells . . . . .	34
2.5. Classical Buckling Analysis of Composite Shells . . . . .	42
2.6. Finite Elements Analysis of Composite Shells . . . . .	51
2.7. Southwell-type Analysis of Elastic Stability . . . . .	53
2.8. Buckling Mode Shape Analysis . . . . .	60
3. EXPERIMENTAL PROCEDURE . . . . .	62
3.1. Cylindrical Test Specimens . . . . .	64
A. Fabrication Method . . . . .	65
B. Laminates Tested . . . . .	68
3.2. Hydrostatic Pressure Tests . . . . .	71
A. Test Set-up and Instrumentation . . . . .	71
B. Test Procedure . . . . .	72
3.3. Ring Tests . . . . .	74
4. RESULTS and DISCUSSION . . . . .	75
4.1. Ring Tests . . . . .	75
4.2. Cylinder Tests . . . . .	77
A. Critical Buckling Pressures . . . . .	79
B. Axial Strain Response . . . . .	88
C. Circumferential Strain Response . . . . .	88
D. Average Circumferential Strain . . . . .	89
E. Modified Southwell Analysis . . . . .	92



F. Mode Shape Deduction from Bending Strains . . . . .	93
G. Failure Progression . . . . .	94
5. SUMMARY AND CONCLUSIONS . . . . .	95
6. RECOMMENDATIONS . . . . .	97
REFERENCES . . . . .	99
APPENDIX A: Circumferential and Axial Strains . . . . .	102
APPENDIX B: Southwell-type Analysis of Strains . . . . .	111
APPENDIX C: Bending Strains and Mode Shape Analysis . . . . .	120
APPENDIX D: Spreadsheets of Strain Gage Readings . . . . .	129
APPENDIX E: ABD Stiffness Matrices . . . . .	138
APPENDIX F: Photographs of the Failed Specimens . . . . .	143



## NOMENCLATURE

The following is a list of the special symbols and nomenclature used in this report.

$N_x, N_y, N_{xy}$  = force resultants per unit length [lbs/in]  
 $A_{ij}$  = laminate extensional stiffness matrix [lbs/in]  
 $B_{ij}$  = laminate extension/bending coupling matrix [lbs]  
 $D_{ij}$  = laminate bending stiffness matrix [lbs in]  
 $\epsilon$  = strain [in/in]  
 $\kappa$  = curvature [1/in]  
 $M_x, M_y, M_{xy}$  = moment resultants per unit length [lbs]  
 $\sigma$  = stress [lbs/in<sup>2</sup>]  
 $\bar{E}$  = equivalent modulus [lbs/in<sup>2</sup>]  
 $R$  = mean radius [in]  
 $t$  = wall thickness [in]  
 $E$  = Young's Modulus [lbs/in<sup>2</sup>]  
 $\nu$  = Poisson's ratio  
 $p$  = hydrostatic pressure (positive external) [psi]  
 $w$  = radial deflection (positive inwards) [in]  
 $L$  = length of the cylinder [in]  
 $n$  = number of circumferential buckling waves  
 $m$  = number of axial buckling waves  
 $x, y, z$  = axial, circumferential and radial coordinates  
 $u, v, w$  = axial, circumferential and radial displacements  
CLT = Classical Laminate Analysis  
GRP = glass reinforced plastic  
GFRP = graphite fiber reinforced plastic (also CFRP)  
W/D = weight to displacement ratio  
AUV = autonomous underwater vehicle (also UUV)  
CTE = coefficient of thermal expansion [in/in<sup>0</sup>F]  
FEA = finite element analysis



## LIST OF FIGURES

Figure 1.1. Relationship of weight to depth ratio to collapse depth for several material systems. . . . .	10
Figure 2.1. Diagram of the coordinate system used in the analysis. . .	19
Figure 2.2. Compression failure modes of unidirectional composites according to Greszczuk [11]. . . . .	23
Figure 2.3. (a) Compression failure modes of fibers, matrices and unidirectional composites according to Hahn and Williams; (b) kink band geometry according to Chaudhuri [11]. . . . .	23
Figure 2.4. A ring of radius R compressed by two forces P acting along a diameter. . . . .	35
Figure 2.5. Typical plot of circumferential strain versus applied hydrostatic pressure, showing extraction of bending and nonlinear strains. . . . .	56
Figure 2.6. Plot of $1/\epsilon_{\text{bending}}$ versus pressure to determine a cylinder's critical buckling pressure. . . . .	57
Figure 2.7. Plot of $1/\epsilon_{\text{non-linear}}$ versus pressure to determine a cylinder's critical buckling pressure. . . . .	58
Figure 3.1. The elastomeric tooling fixture used to manufacture the cylindrical test specimens. . . . .	66
Figure 3.2. . . . .	69
Figure 3.3. . . . .	69
Figure 3.4. . . . .	69
Figure 3.5. . . . .	69
Figure 3.6. Details of cylinder potted in endcap. . . . .	72
Figure 3.7. Diagram of experimental set-up, showing pressure chamber and instrumentation. . . . .	73
Figure 4.1. Laminate ranking using Jones' Equation. . . . .	82
Figure 4.2. Laminate ranking using ABAQUS. . . . .	82
Figure 4.3. Laminate ranking using Southwell-type analysis. . . . .	83
Figure 4.4. Laminate ranking using the results of hydrostatic testing. . . . .	83
Figure 4.5. Critical buckling pressures for 1:1 Specially Orthotropic laminates. . . . .	86
Figure 4.6. Critical buckling pressures for 2:1 Specially Orthotropic laminates. . . . .	86
Figure 4.7. Critical buckling pressures for Quasi-isotropic laminates. . . . .	87
Figure 4.8. Critical buckling pressures for Interleaved Orthotropic laminates. . . . .	87



Figure 4.9. Axisymmetric circumferential membrane strain response for the 1:1 specially orthotropic cylinders. . . . .	90
Figure 4.10. Axisymmetric circumferential membrane strain response of the 2:1 specially orthotropic cylinders. . . . .	90
Figure 4.11. Axisymmetric circumferential membrane strain response for the quasi-isotropic cylinders. . . . .	91
Figure 4.12. Axisymmetric circumferential membrane strain response for the interleaved orthotropic cylinder. . . . .	91



## 1. INTRODUCTION

### 1.1. Potential Benefits of Composite Pressure Hulls

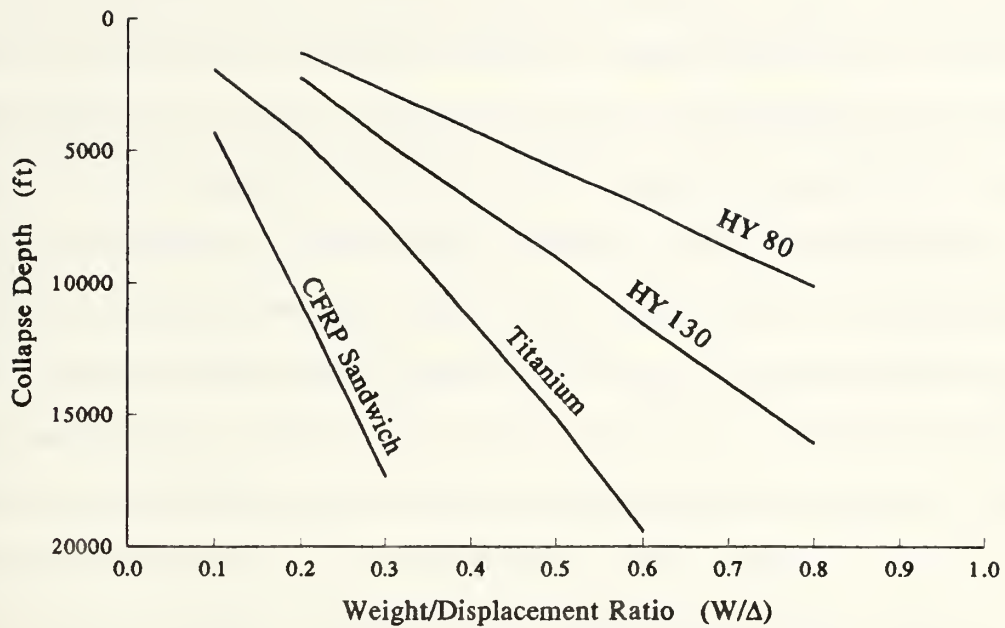
Since the 1960's fiber reinforced composite materials have been proposed for the construction of submersible pressure hulls. The potential benefits that can be offered by composite materials over metals include:

- o structural weight reductions;
- o fabrication of novel hull geometries;
- o incorporation of acoustic silencing;
- o electromagnetic signature reduction;
- o virtual elimination of corrosion.

The purpose of this project is to gain insight into the use of graphite/epoxy for this application, through the systematic testing to hydrostatic pressure collapse and subsequent analysis of several thin-walled laminated composite cylinders, of various laminate types.

Weight Reduction. Composite materials offer the opportunity to make reductions in the portion of a submersible's weight that has to be devoted to the hull structure. In fact, submersible designers use as a measure of hull efficiency the ratio of the hull weight to the weight of the water the hull displaces. This ratio is referred to as the "W/D". It must be less than one for the submersible to float, and a smaller "W/D" means that the hull is more efficient,





4

Figure 1.1. Relationship of weight to depth ratio to collapse depth for several material systems.

because for a given depth it can either carry more payload or use less energy. Values approaching 0.30 are required for the design of small vehicles with adequate allowances for mission capabilities. Figure 1.1 shows graphically the relationship of W/D to collapse depth for several materials [1]. From this figure it is seen that composite materials can offer substantial increases in collapse depth at any given W/D, or that for a specified collapse depth requirement composites enable large reductions in structural weight [2].

The major structural weight savings obtained via use of composite material construction can be directly utilized in other mission enhancing areas. Table 1.1 compares the typical weight allocations for an Autonomous Underwater Vehicle (AUV)



[1] with current U.S. Navy attack submarine (SSN) and fleet ballistic missile submarine (SSBN) design practices. Small submersibles are very volume critical, and designers always have more and larger payloads than they are capable to carry. Weight reductions in the hull structure can be translated into increased payload weight and volume capacity. For the many small submersibles where speed or range increases would be more beneficial, portions of the structural weight savings could be channeled into larger propulsion machinery or fuel carrying capacity. For submersibles that require the capability to reach greater safe operating depths, the incorporation of composite materials could make the hull structure stronger without giving up established payload, propulsion and fuel allotments.

CATEGORY	AUV	SSN	SSBN
1. Hull Structure	30.6	34	32
2. Variable Ballast	3.7	12	12
3. Propulsion	32.3	25	13
4. Payload	13.4	2	17
5. Fixed Ballast	1.5	5	12
6. All Others	18.5	22	14

Table 1.1. Typical weight allocations of submersibles.

Novel Hull Shapes. The methods of fabricating composite material hull structures make it easier for the designer to create complex geometrical shapes and incorporate advanced



sandwich and double hull structural configurations. The use of novel structural geometries such as figure-eight and swedge hull shapes, allow for improved structural efficiency by optimizing the usage of space and volume as compared to traditional cylindrical and spherical hullforms [3]. Filament winding fabrication techniques allow for complex streamlined axisymmetric shapes to be constructed with relative ease.

Signature Control. A major advantage of laminated composite pressure hulls is in the reduction of acoustic and non-acoustic signatures. This can be crucial in missions such as mine hunting and covert reconnaissance. Composites have seen years of usage as sonar windows due to their inherent acoustic transparency [4]. Also, by innovative utilization of low density sandwich cores and other acoustic damping and decoupling lamina and anechoic coatings, internal noises from machinery and electronics can be silenced to provide improved stealth. Because they are non-metallic, these materials are also non-magnetic and electrically non-conductive, greatly lowering a submersible's susceptibility to enemy weapons and sensors.

Corrosion Control. Corrosion, which is a major problem for metals in the marine environment, can be virtually eliminated with properly selected composite material systems. However, in completeness, it must be mentioned that initial attempts at utilizing composites, specifically glass



reinforced plastic (GRP), found that seals around hull penetrations, hatches and viewports were susceptible under cyclic loading. The high deformation of the GRP as compared to metallic inserts left cut fibers vulnerable to exposure to water at high pressure. Because of this designs have been developed where cylindrical composite pressure hulls are used in conjunction with specially designed titanium end closures. In these designs all penetrations are made through the titanium end closures thus avoiding the difficult problem of penetrating the laminated composite pressure hull. Due to the weight of the metal end closures and because the unstiffened hulls are buckling critical, the overall hull weight may not show as significant reductions as predicted for all-composite hulls. Notwithstanding this, all the benefits presented by composite materials and the fact that any weight reduction is precious to a submersible designer, these advanced materials are well suited for utilization in pressure vessel design and construction. Graphite fiber reinforced plastics (GFRP) because of their higher modulus, lighter weight, and extraordinary fatigue properties generally offer more long term benefits than GRP.



## 1.2. Purpose of Hydrostatic Testing

Four areas of major concern in the design of laminated composite pressure hulls are:

- o fabrication procedures,
- o repairability and serviceability,
- o inspection and certification,
- o in-service hull monitoring.

The present investigation, consisting mainly of the hydrostatic testing of 12-ply graphite/epoxy cylindrical specimens of various layups, is aimed at providing data and techniques to better facilitate the addressing of these concerns.

Prior to and concurrent with this test program, an analysis, both classical and numerical, was performed to predict the buckling characteristics of the graphite/epoxy cylinders that were tested here [5]. In this analysis, closed form solutions were able to be used for the cylinders constructed of orthotropic laminates. These laminates do not exhibit any coupling between extension and shear or bending and twisting stiffnesses (i.e. they have no  $A_{16}$ ,  $A_{26}$ ,  $B_{16}$ ,  $B_{26}$ ,  $D_{16}$ , or  $D_{26}$  terms in their ABD matrices, which relate stress to strain). Finite element analysis was also conducted on these orthotropic laminates and additionally on laminates with angle plies. These angle-ply laminates generally have some coupling between extension and shear or bending and twisting due to the



presence of these additional stiffness terms.

Each specimen was instrumented with eight equally spaced circumferential strain gages. The average of these strains was compared to the axisymmetric strain that is predicted by theory and was also used as the membrane strain for a Southwell-type analyses to predict perfect shell buckling characteristics from experimental data from imperfect specimens.

In summary, the main work on this thesis was to conduct a large series of experiments in an effort to verify the results of theoretical elastic stability analyses methods that have been adapted for laminated cylindrical shells subjected to hydrostatic pressure. Since shell buckling characteristics are highly susceptible to laminate imperfections, geometrical deviations, and residual stresses, the results of this testing depended greatly on the effectiveness of the specimen manufacturing method. The fabrication technique chosen for this project consistently produced specimens of high circularity, but the following defects were found to varying extents in all the cylinders: wrinkled fibers, non-uniform resin distribution, voids and delaminations. In several of the specimens noticeable defects, especially severely wrinkled plies, were apparently responsible for large degradations in the buckling strengths of these cylinders.

Although these circular cylindrical shells exhibit significant buckling sensitivity to geometric shape



imperfections just like isotropic shells, in general, laminated composites offer the opportunity to reduce these effects by selecting appropriate fiber orientations. An overall goal of this entire analytical and experimental test program is to develop and verify a method to optimize the selection of ply orientations in order to achieve the most efficient hull for specific requirements. Before optimization routines can be applied to numerical or closed form solutions, there must be confidence that these solutions are fairly accurate and can at least rank various laminate configurations correctly. Four different laminates were chosen to be evaluated by experimental test methods in an effort to test the analyses:

- o 1:1 specially orthotropic -  $[90_3/0_3]_s$  ,
- o 2:1 specially orthotropic -  $[90_4/0_2]_s$  ,
- o quasi-isotropic -  $[90_2/(\pm 30)_2]_s$  ,
- o interleaved (unsymmetric) orthotropic -  $[90_2/0]_{4r}$  .

By testing multiple specimens of each type, and comparing the rankings with the results of the analysis, insight into the correctness of the theoretical methods was obtained.

Another significant contribution of this hydrostatic testing results from the extensive strain gage instrumentation that was utilized on each cylindrical specimen. On the centerline of every specimen were placed eight circumferential strain gages at 45° separation and two axial strain gages at 180° separation. Readings from these gages provided the



ability to validate the assumptions of buckling prediction theories, to investigate the applicability of alternative methods of stability determination, and to provide insight into the mode shapes into which the cylinders buckled.

In the 1930's, R.V. Southwell proposed a method to determine the buckling strength of an ideally straight column by analysis of test data taken from a column with initial curvature [6]. In the 1950's, G.D. Galletly and T.E. Reynolds proposed that an extension of this method may be used to determine the elastic stability of ring-stiffened cylinders [7]. The applicability of this method to determine the stability of composite laminated cylinders was investigated using the strain data collected during the hydrostatic pressure tests.

By isolating the bending strain from the membrane strain at the eight locations around the centerline of the specimens and applying elementary concepts that relate the local radial deflections to the changes in circumference, a deduction was made of the buckling mode shape of each of the specimens. These mode shape deductions are compared to those assumed and predicted by the analysis methods.



## 2. ANALYTICAL BACKGROUND

This section addresses the significant issues in material science and in structural stability pertinent to the failure of laminated, fiber reinforced composite cylinders subjected to external hydrostatic pressure. Designing with laminated composite materials offers the opportunity to achieve specific structural properties through proper selection of:

- o the system of resin, fibers and enhancing agents;
- o processing and production techniques;
- o individual ply orientations.

To make these selections the designer must consider concerns ranging from the micromechanical bonding of the fibers and the matrix, to the ability of the structural fabrication technique produce highly circular cylinders. This chapter attempts to bring together some of the information and experience that have been gained in these broad fields. Only by making the material scientist and the naval architect aware of the other's knowledge and concerns, can all the benefits presented by the utilization of composite materials in submersible pressure hull design and construction be realized.

The discussion first addresses the material science concerns, beginning with the micromechanical factors controlling the compressive failure of fiber reinforced laminated composites, and leading to a macromechanical treatment of Classical Laminate Theory.



The discussion then covers the major structural concerns, starting with the axisymmetric compression of circular cylinders, progressing through the compression of thin rings to the elastic stability theories for long cylindrical shells.

The two fields merge with a coverage of a classical buckling analysis method for laminated cylinders, that is based on Donnell's stability theory. Figure 2.1 shows the coordinate system and dimensional nomenclature used in this analysis. Next, brief coverage is given of some recent finite element studies on this subject.

Finally, a modified Southwell-type method is presented that should be universally applicable to a wide range of isotropic and anisotropic material systems. Additionally, a method is proposed whereby the bending strain data can be used to deduce the number of circumferential waves in the actual buckling mode shape of a cylindrical specimen.

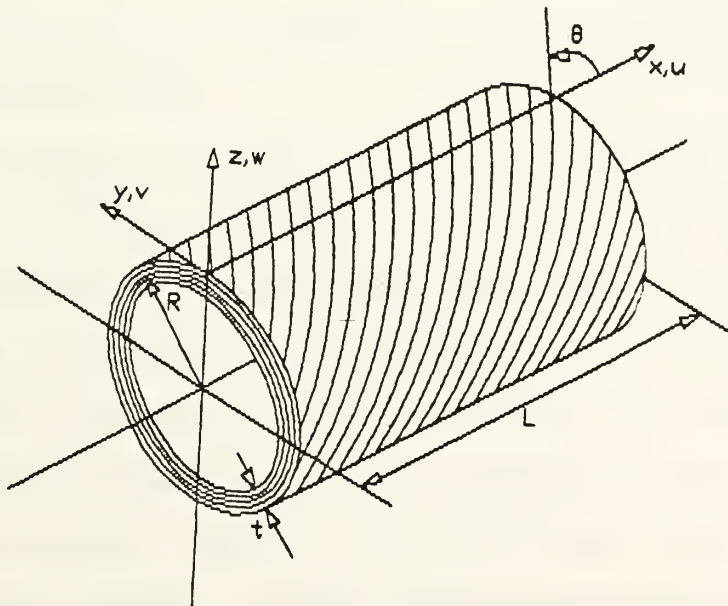


Figure 2.1. Diagram of the coordinate system used in the analysis.



## 2.1. Compressive Strength of Composite Laminates

The compressive response of fiber-reinforced composite materials is still one of the least understood in the field of composites today. The compression failures of composite laminates can be categorized into the following mechanisms: "global Euler buckling, microbuckling, transverse tension, fiber kinking, fiber compression failures, matrix compression failures, and delamination." [8] The compression failure modes of fibers, matrices and unidirectional composites are illustrated in Figures 2.2 and 2.3, which were taken from reference 11. The predominant mechanism is determined by factors such as the individual properties of each of the constituent materials, the orientation of the plies within the laminate, the geometry of the specimen, the method of load application, any waviness and misalignment of the fibers, the presence of voids and discontinuities in the matrix, and any stress concentrations.

If the fibers are weak enough in compression, they could fail due to compression before the onset of buckling and cause ultimate failure of the laminate. But unlike tension, the compressive strength of most composites is limited more by the properties of the matrix than the fiber reinforcement. Microbuckling can begin to occur because the resin is soft, initiating ultimate failure, even when the fibers are not weak in compression. Other reasons the matrix may not be able to



provide adequate lateral support to the fiber are: proximity to a free surface, the formation of lateral splitting, a high void content, or environmental softening. Desirable matrix properties include a moderate amount of stiffness and toughness, but not an excess. Elastic microbuckling is the dominant failure mode when either the fibers have no initial misalignment or the matrix is very soft. The low compressive strengths of fiber reinforced composites may also be the result of kink band formation, an occurrence that was predicted by theory and is now possible to observe experimentally. This type of compression failure results from fiber misalignment and involves plastic deformation of the resin.

Microbuckling. Fiber buckling theories are based on the stability of fibers in a flexible matrix. The fibers may buckle in either of two modes: (1) when the fiber volume fraction is greater than 30 percent, the fibers tend to buckle in phase (shear mode), and (2) when the fiber volume is less than 30 percent, the fibers tend to buckle out-of-phase (extensional mode) [9]. In a study of the effects of various constituent properties, fiber arrays, and bowed, unbonded and misaligned fibers, Greszczuk concluded that the microbuckling models cannot predict the failure of non-idealized, actual composites. He stated further that low-modulus resins result in microbuckling failure, but when higher modulus resins are used the failure mode changes and



the compressive strength of the fiber reinforcement controls the failure [10].

Kink Band Formation. When the resin system is adequately stiff and there exists any fiber waviness, regardless of the mode of incipient failure, final failure occurs as the formation of kink bands. Chaudhuri conducted an analytical study to identify the basic failure mechanisms of graphite/epoxy cylinders with thick walls under hydrostatic compression [11]. He identified the dominant compressive failure mode for thick composite cylinders to be the "formation and propagation of fiber kink bands at the microscopic level, triggered by the fiber misalignment defects formed during the manufacturing process, leading to the shear crippling failure at the macroscopic level." He found that this kinking was the lowest energy compression failure mode at the microlevel of graphite/epoxy composites, and was limited by the initial fiber misalignment, the ultimate fiber strain and the two transverse shear moduli,  $G_{LT}$  and  $G_{TT}$ , of the laminate.

Chaudhuri's study is important because it shows that kink band formation is a distinct and lower energy failure mode than elastic microbuckling, not due solely to the effect of plasticity in the presence of initial fiber misalignment. Chaudhuri also noted that the ratio of hoop to axial layers did not strongly influence the compressive strength of the thick-walled ( $R/t \leq 6$ ) composite cylinders he investigated.



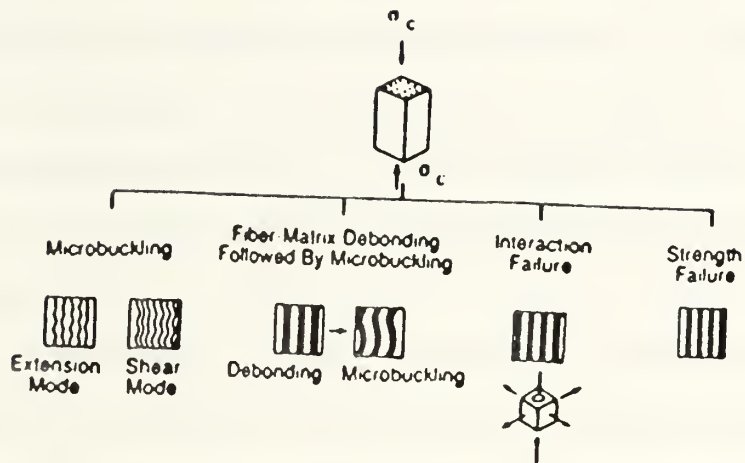


Figure 2.2. Compression failure modes of unidirectional composites according to Greszczuk [11].

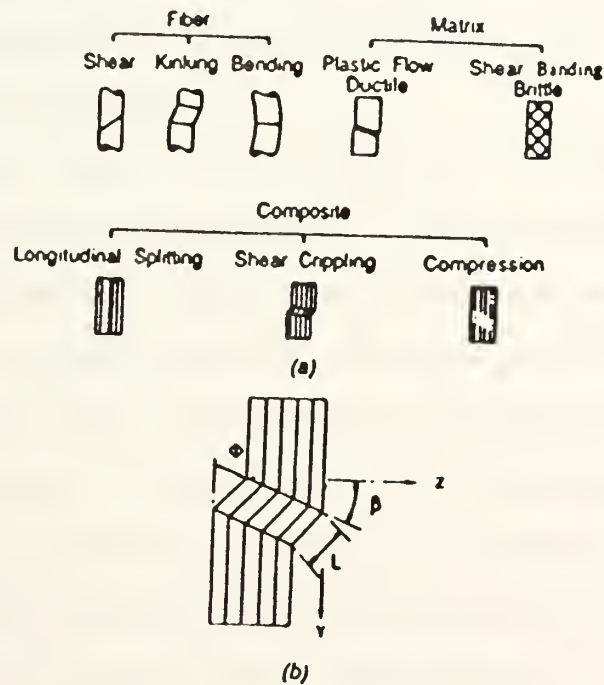


Figure 2.3. (a) Compression failure modes of fibers, matrices and unidirectional composites according to Hahn and Williams; (b) kink band geometry according to Chaudhuri [11].



Higher toughness usually means fiber kinking will occur at lower strains, but lower toughness (i.e. higher modulus) usually means that there is less resistance to delamination propagation. Therefore, there must be a tradeoff between the delamination associated with higher modulus resins and the earlier (i.e. at lower strains) microbuckling initiation found with tougher resins.

Shuart presented a linear analysis of short-wavelength modes shapes for off-axis and angle-ply graphite/epoxy laminates and a non-linear analysis of laminate stresses, out-of-plane displacements, and interlaminar shear strains [12]. He showed that significant interlaminar shearing strains develop before short-wavelength buckling, and he described a compression failure criterion that included both these failure mechanisms.

Even though fibers do not creep, all polymer matrices exhibit viscoelastic creep behavior which is affected by water absorption. Mechanical impact damage and exposure to high temperatures can aggravate this problem. Irion and Adams presented results that indicate that longitudinally reinforced graphite composites, in general, do not creep any significant amount. They found that transversely reinforced graphite composites exhibited long periods at high strains with no creep followed by abrupt jumps. Because few of their specimens attained steady-state creep and also due to the fact that the strain versus time plots displayed extensive amounts of



irregularities, they inferred that local failures were occurring almost continually, but after initiation the failures were quickly arrested [13].

Transverse tensile stress in unidirectional composites has been proposed as a reason experimental compression failures occur at much lower loads than predicted by theory. Even though this stress is small, unidirectional composites have low transverse strength.

In view of all this the expected failure sequence for laminated shells constructed from plies of unidirectional graphite fiber-reinforced composites with fiber volume fractions greater than 30%, and loaded in hydrostatic compression can be summarized as follows: "microbuckling in a shear mode (in-phase buckling) will occur, initiated by regions of local inhomogeneities (voids, stress concentrations, areas of weak matrix, free boundaries), and lead to final failure in the form of fiber kinking or fiber overstressing in bending." [8]

A major limiting factor on the compression strength of laminated composites is the technique of fabrication. Manufacture of the specimen has significant effect on the composite's compressive response because the presence of local inhomogeneities and defects, which are difficult to model and otherwise account for, influence the compressive failure mechanisms on the microstructural level more than any of the other stress state failure mechanisms. Therefore, the chosen



method of fabrication must result in a low void content (less than 2 %), because otherwise the fibers located adjacent to a void will not have sufficient lateral support. Laminates must also be fabricated with very low amounts of fiber misalignment (compressive strength can be highly sensitive to fibers out of alignment as little as 2°). Some research suggests that processing with high fiber content (greater than 60%) may result in lower void contents and, therefore, more precise fiber alignment.

The 5208 epoxy resin used in the fabrication of the cylinders for this present study has a high modulus, with failure strains of 1.4%. This low resin toughness has a detrimental effect on the progression of the failure. Studies have shown that compression failure of brittle laminates, such as T300/5208, is quite sudden, and that it is very difficult to arrest the resulting fiber kinking [14]. Sinclair and Chamis conducted compression tests on unidirectional T300/5208 graphite/epoxy laminates and their results were divided into a high-strength group where failure was predicted by fiber compressive failure, a medium strength group that was predicted by flexure or delamination, and a low strength group that was predicted by Euler Buckling [15].



## 2.2. Classical Laminate Theory

Before discussing the elastic stability of composite pressure hulls, a brief overview of Classical Laminate Theory (CLT) is given. The concept of equivalent moduli for orthotropic cylinders is also developed to enable relationships designed for isotropic rings and cylindrical shells to be adapted, without excessive complexity, to the case of the laminated composite rings and cylindrical specimens tested in this research.

For laminated orthotropic materials the constitutive relationship between stress and strain is complicated by the directional nature of the individual plies in the laminate. The elastic modulus for isotropic materials is replaced by an ABD matrix that contains information on the extension, shear and bending behavior of the laminate and the coupling between the extension, shear and bending. The normal presentation of this constitutive relation is

$$\begin{Bmatrix} N_x \\ N_y \\ N_{xy} \\ - \\ M_x \\ M_y \\ M_{xy} \end{Bmatrix} = \begin{bmatrix} A_{11} & A_{12} & A_{16} & | & B_{11} & B_{12} & B_{16} \\ A_{21} & A_{22} & A_{26} & | & B_{21} & B_{22} & B_{26} \\ A_{61} & A_{62} & A_{66} & | & B_{61} & B_{62} & B_{66} \\ - & - & - & + & - & - & - \\ B_{11} & B_{12} & B_{16} & | & D_{11} & D_{12} & D_{16} \\ B_{21} & B_{22} & B_{26} & | & D_{21} & D_{22} & D_{26} \\ B_{61} & B_{62} & B_{66} & | & D_{61} & D_{62} & D_{66} \end{bmatrix} \begin{Bmatrix} \epsilon_{xx}^o \\ \epsilon_{yy}^o \\ \gamma_{xy}^o \\ - \\ \kappa_x \\ \kappa_y \\ \kappa_{xy} \end{Bmatrix} \quad (1)$$



where

$$A_{ij} = \sum_{k=1}^N Q_{ij}^k (z_k - z_{k-1}) \quad (2)$$

$$B_{ij} = \frac{1}{2} \sum_{k=1}^N Q_{ij}^k (z_k^2 - z_{k-1}^2) \quad (3)$$

$$D_{ij} = \frac{1}{3} \sum_{k=1}^N Q_{ij}^k (z_k^3 - z_{k-1}^3) \quad (4)$$

In general, the  $B_{ij}$  terms couple the bending and stretching effects. If the laminate is symmetric about the middle plane, there is no such coupling and thus  $B_{ij}=0$ . In specially orthotropic laminates, which are cross-ply laminates composed of plies oriented at  $90^\circ$  relative to each other, there is no coupling between bending and twisting effects, and, therefore,  $A_{16}=A_{26}=D_{16}=D_{26}=0$ .

To enable comparison of the relationships in the following sections for the axisymmetric compression and elastic stability of long composite cylinders with the experimental results, equivalent properties for an orthotropic cylindrical shell were developed.

The membrane constitutive relations for an orthotropic material, where the bending response and extension/shear coupling are neglected, are



$$\begin{Bmatrix} N_x \\ N_y \\ N_{xy} \end{Bmatrix} = \begin{bmatrix} A_{11} & A_{12} & 0 \\ A_{12} & A_{22} & 0 \\ 0 & 0 & A_{66} \end{bmatrix} \begin{Bmatrix} \epsilon_x^o \\ \epsilon_y^o \\ \gamma_{xy}^o \end{Bmatrix} \quad (5)$$

This is inverted to solve for the strains, such that

$$\begin{Bmatrix} \epsilon_x^o \\ \epsilon_y^o \\ \gamma_{xy}^o \end{Bmatrix} = \begin{bmatrix} a_{11} & a_{12} & 0 \\ a_{12} & a_{22} & 0 \\ 0 & 0 & a_{66} \end{bmatrix} \begin{Bmatrix} N_x \\ N_y \\ N_{xy} \end{Bmatrix} \quad (6)$$

where

$$\begin{aligned} a_{11} &= \frac{A_{22}}{A_{11} A_{22} - A_{12}^2} \\ a_{12} &= \frac{-A_{12}}{A_{11} A_{22} - A_{12}^2} \\ a_{22} &= \frac{A_{11}}{A_{11} A_{22} - A_{12}^2} \\ a_{66} &= \frac{1}{A_{66}} \end{aligned} \quad (7)$$

For the case of hydrostatic loading,

$$\begin{aligned} N_x &= \sigma_x t = \frac{pR}{2} \\ N_y &= \sigma_y t = pR \end{aligned} \quad (8)$$



and thus

$$\epsilon_y^o = \left[ \frac{-\frac{1}{2} A_{12} + A_{11}}{A_{11} A_{22} - A_{12}^2} \right] p R \quad (9)$$

and the equivalent modulus in the hoop direction is therefore,

$$\overline{E}_y = \frac{A_{11} A_{22} - A_{12}^2}{-A_{12} \frac{t}{2} + A_{11} t} \quad (10)$$

Similarly, the equivalent modulus in the axial direction is

$$\overline{E}_x = \frac{A_{11} A_{22} - A_{12}^2}{A_{22} \frac{t}{2} - A_{12} t} \quad (11)$$

and the equivalent Poisson's ratio is

$$\overline{\nu} = \frac{A_{12}}{A_{22}} = \nu_{12} \quad (12)$$

These expressions can be used later with the experimental results, to check the effective properties of the cylindrical specimens as fabricated. Note that these relations only apply to the case of hydrostatic loading, for other loading conditions other equivalent moduli must be developed.



### 2.3. Axisymmetric Compression of Cylindrical Shells

It has been said that axisymmetric yield failure is the most important mode of failure of externally loaded pressure vessels because a "sensible design should eliminate failure due to instability." [16] This is lofty goal for thin-skinned pressure vessels because initial geometric imperfections on the order of a tenth of the thickness can cause a catastrophic loss of buckling resistance of pressure vessels when subjected to external water pressure.

One of the earliest solutions for the axisymmetric deformation of circular cylinders under external loading was published by von Sanden and Gunther in 1920 [17]. Their original work unfortunately had two signs interchanged in the formula for circumferential stress, which can give incorrect values if used unknowingly. Also, these authors did not take into account the beam-column effect and its associated non-linear deformations, that was later introduced by Salerno and Pulos [18] and refined by Ross [23] into the form

$$\frac{d^4 w}{dx^4} + 4\alpha^4 \beta^2 \frac{d^2 w}{dx^2} + 4\alpha^4 w = \frac{12(1-\nu^2)\xi}{t^2 R^2} \quad (13)$$



where

$$\begin{aligned}\alpha^4 &= \frac{3(1-\nu^2)}{R^2 t^2} \\ \beta^2 &= \frac{pR^3}{2Et} + \frac{t^2 \nu}{12(1-\nu^2)} \\ \xi &= \frac{pR^2(1-\frac{\nu}{2})}{Et}\end{aligned}\tag{14}$$

Ross gives the complete solution, but here is presented only the solution for our case of a circular shell element, stiffened by equal-strength frames located at its ends ( $x=0,L$ ), and deformed symmetrically about the midspan,

$$w = A_1 \cosh\left[F_1\left(x-\frac{L}{2}\right)\right] \cos\left[F_2\left(x-\frac{L}{2}\right)\right] + A_2 \sinh\left[F_1\left(x-\frac{L}{2}\right)\right] \sin\left[F_2\left(x-\frac{L}{2}\right)\right] + \xi\tag{15}$$

where

$$F_1 = \alpha\sqrt{(1-\alpha^2\beta^2)} \quad F_2 = \alpha\sqrt{(1+\alpha^2\beta^2)}\tag{16}$$

and  $A_1$  and  $A_2$  are functions of  $F_1$  and  $F_2$  that reflect the characteristics of the end frame and the boundary conditions assumption that  $dw/dx=0$  where the edge connects to the end frame ( $x=0,L$ ). The variation of the hoop and axial stress along the shell is due to the radial contraction, the Poisson's effect of the axial compression, and the beam-column



effect. These are expressed in the following relationships for hoop stress and axial stress, respectively, where the last term is the beam-column effect and is positive in the inner fibers and negative in the outer fibers.

$$\text{HoopStress: } \sigma_y = -\frac{Ew}{R} - \frac{pRv}{2t} \pm \frac{Et}{2(1-v^2)} \left( \frac{w}{R^2} + v \frac{d^2w}{dx^2} \right) \quad (17)$$

$$\text{AxialStress: } \sigma_x = -\frac{pR}{2t} \pm \frac{Et}{2(1-v^2)} \left( \frac{vw}{R^2} + \frac{d^2w}{dx^2} \right) \quad (18)$$



## 2.4. Elastic Stability of Long Cylindrical Shells

The discussion of the elastic stability of laminated composite shells begins with a review of classical buckling theories for isotropic shells of revolution. This paper addresses only cylindrical shells whose thickness  $t$  is small compared to the other dimensions of the shell, especially the radius of curvature. The discussion begins with a thin ring under symmetric two-point compression and works toward the theories for a cylinder of length  $L$  and radius  $R$ .

The theory for thin isotropic circular rings under compressive loading was presented by S.P. Timoshenko in his classic text on elastic stability [19]. A summary of that analysis is given, and extended for the case of laminated composite rings. The relationships obtained here will be used in the analysis of the results obtained from the two-point compression testing of 1/2 inch ring specimens that were cut from the excess ends of each cylinder.

Consider a isotropic circular ring of unit width, subjected to a two-point compression load  $P$  as shown in figure 2.3. The bending moment at A (and at B) is denoted  $M_o$  and the moment at an arbitrary location  $\theta$  is

$$M = M_o + \frac{PR}{2} (1 - \cos\theta) \quad (19)$$

The differential equation for the radial deflection of this



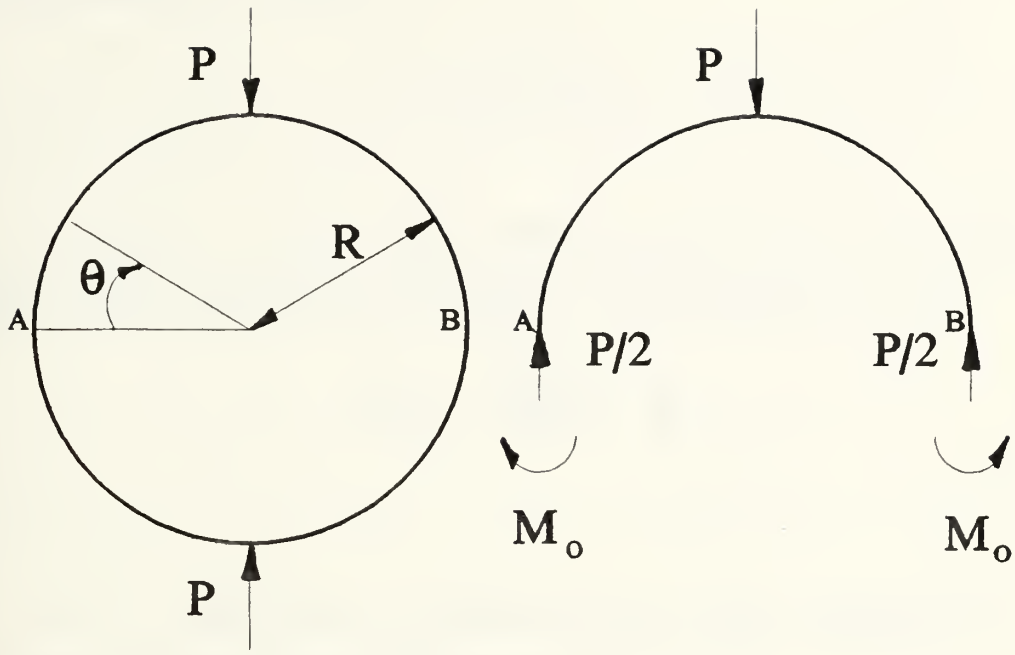


Figure 2.4. A ring of radius  $R$  compressed by two forces  $P$  acting along a diameter.

ring at any point  $\theta$  due to this loading is

$$\frac{d^2w}{d\theta^2} + w = -\frac{M_o R^2}{EI} - \frac{PR^3}{2EI} (1 - \cos\theta) \quad (20)$$

From the symmetry of the problem where

$$\frac{dw}{d\theta} = 0 \quad \text{at } \theta = 0 \text{ and } \theta = \frac{\pi}{2} \quad (21)$$

the general solution of equation 20 is found to be

$$w = \frac{PR^3}{4EI} \left[ \cos\theta - \frac{M_o}{4PR} - 2 + \theta \sin\theta \right] \quad (22)$$

Timoshenko then applied Castigliano's theorem to the strain



energy expression to get

$$M_o = \frac{PR}{2} \left( \frac{2}{\pi} - 1 \right) \quad (23)$$

Of interest to us is the radial deflection at the point of load application ( $\theta=\pi/2$ ), which from equation 22 is

$$w \Big|_{\theta=\frac{\pi}{2}} = \frac{PR^3}{4EI} \left( \frac{\pi}{2} - \frac{4}{\pi} \right) \quad (24)$$

where  $w < 0$  indicates the shortening of the diameter or deflection inward toward the center.

For the case of a thin ( $R \gg t$ ) laminated composite ring, a two-point, symmetric compressive force has a negligible direct effect on the stress on the inner and outer surfaces at point A, and this stress, therefore, is almost entirely due to the bending moment resulting from that applied point force. Additionally the compressing ring is assumed to undergo cylindrical bending ( $\kappa = 0$ ) and not anticlastic bending. Under these conditions, equation 1 can be simplified to

$$\begin{Bmatrix} M_x \\ M_y \end{Bmatrix} = \begin{bmatrix} D_{11} & D_{12} \\ D_{12} & D_{22} \end{bmatrix} \begin{Bmatrix} \kappa_x \\ \kappa_y \end{Bmatrix} \quad (25)$$

With cylindrical bending and negligible Poisson's effect, we get that



$$M_y = D_{22} \kappa_y \quad (26)$$

From the definition of curvature as the second derivative of the displacement we see that effectively,

$$D_{22} \sim \frac{EI}{b} \quad (27)$$

$$M_y \sim \frac{M_o}{b}$$

Substituting this effective bending stiffness of the laminated ring,  $D_{22} \cdot b = EI$ , into Timoshenko's formula for an isotropic ring, equation 24, and solving for  $D_{22}$  gives

$$D_{22} = 0.0744 \frac{R^3}{b} \left( \frac{P}{w} \right) \quad (28)$$

On the inner and outer surfaces the strain is related to the curvature, such that

$$\epsilon_y = \epsilon_y^o + \kappa_y z_{upper} \quad (29)$$

where  $\epsilon_y^o$  is negligible for this loading, as explained above, and  $z_{upper} = t/2$  on the surfaces. Combining equations 23, 26 and 29 gives a relationship for the hoop strain on these surfaces in terms of the applied compressive load  $P$ , such that

$$\epsilon_y = \mp 0.1817 \frac{t}{2} \frac{PR}{D_{22} b} \quad (30)$$



Solving for  $D_{22}$  gives

$$D_{22} = \mp 0.0908 \frac{Rt}{b} \left( \frac{P}{\epsilon_y} \right) \quad (31)$$

Therefore, we now have a way to approximate the  $D_{22}$  of the ring with the slope of the load versus displacement plot, equation 28, and with the slope of the load versus strain plot, equation 31. These experimentally determined  $D_{22}$ 's can be compared to the one obtained from CLT and the properties of T300/5208. The complete ABD matrices for each of the laminate types were developed in this way and are contained in Appendix E. This comparison provides insight into the actual bending stiffness properties of each of the laminate types as fabricated.

Next, consider now how the radial deflection in the ring under the two-point, symmetric loading would be changed if a hydrostatic pressure of magnitude  $p$  was applied. This uniform external pressure produces a compressive force  $S = pR$  in the ring of unit width. This force combined with the symmetric, two-point loading considered above produces the deflection expressed by

$$w = \frac{2PR^3}{\pi EI} \sum_{n=2,4,\dots}^{n=\infty} \frac{(-1)^{n/2} \cos n\theta}{(n^2-1)^2 \left[ 1 - \frac{SR^2}{(n^2-1)EI} \right]} \quad (32)$$



This means that each term in  $w$  increases as the compressive force  $S$  increases, becoming indefinite when

$$S \rightarrow \frac{(n^2-1)EI}{R^2} \quad (33)$$

In this case the critical compressive force occurs when  $n=2$ , therefore

$$w = - \frac{2pR^3}{9\pi EI} \frac{\cos 2\theta}{\left(1 - \frac{S}{S_{crit}}\right)} \quad (34)$$

This thin ring analysis can now be extended to the buckling of long circular cylinders under uniform external pressure. The critical pressure  $p_{crit}$  on an elemental ring of unit width of the cylinder is obtained by considering poisson's effects that were not a part of the isolated ring above, i.e. substitute  $E/(1-\nu^2)$  for  $E$  and  $t^3/12$  for  $I$ .

$$p_{crit} = \frac{E}{4(1-\nu^2)} \left(\frac{t}{R}\right)^3 \quad (35)$$

This calculated critical pressure is applicable as long as the compressive stress does not exceed the material's proportional limit.

One of the most significant contributions to this subject was the general theory of shell instability developed by W.



Koiter in 1945 [20]. In his thesis, Koiter demonstrated conclusively that initial geometric imperfections play a dominant role in reducing the buckling load of shell structures. This helped explain the scatter in experimental buckling test results and the general inability of researchers to experimentally attain theoretically predicted critical pressures. The greatest detriment to achieving theoretical buckling pressure predictions is imperfections in the shape of the shell. Koiter showed that in isotropic shells an imperfection amplitude of just 10% of the wall thickness of the shell can result in as large as a 40% reduction in its buckling strength. This can be uncontrollable in thin-skinned shells with  $R/t \gg 10$  like those studied here. More recent work by Koiter and others has led to theories where the effect of small but finite imperfections are included in the stability analysis. These give the designer the ability to account for geometric imperfections that can be assumed to be present in the as-manufactured pressure vessel. Noteworthy of these is an equation derived by Kendrick [21] which describes the stress in an isotropic cylinder due to eccentricities, such that

$$\sigma_y = \frac{pR}{t} + \frac{pv}{2} \left( \frac{\pi R}{L} \right)^2 + \frac{Et}{2R^2(1-\nu^2)} \left[ n^2 - 1 + \nu \left( \frac{\pi R}{L} \right)^2 \right] C_o \left( \frac{p}{p_{crit} - p} \right) \quad (36)$$

where  $C_o$  is the amplitude of the initial deviation in a mode shape  $\cos(n\theta)$ . The most important term in this equation is



$$C_o \left( \frac{P}{P_{crit} - P} \right) \quad (37)$$

which shows that the hoop stress is directly proportional to the amplitude of the initial eccentricities in the cylinder. It also verifies that a failure envelope exists for a cylinder under external hydrostatic pressure because the stress becomes singular as the critical buckling pressure is approached.



## 2.5. Classical Buckling Analysis of Composite Shells

This section reviews some of the more prominent theories on the buckling stability of laminated composite cylindrical shells. These theories are referred to as "classical" because they all relate the concepts of Classical Laminate Theory (CLT) to one or more of the classic elastic stability theories. The analysis begins with circular cylinders constructed of orthotropic layers and is based on work presented by R.M. Jones. Next, the analysis considers the introduction of angle plies and is based on work by Booten and Tennyson. Lastly, the analysis proposes the application of optimization techniques to laminate orientation selection and is based on the recent work of several different authors, most notably Sun. Please note that subscripts following a comma represent partial differentiation by that subscript. For example, the term  $N_{,x}$  is equivalent to the expression  $\partial N_x / \partial x$ .

In 1968, Robert M. Jones presented an exact solution for the buckling of a circular cylindrical shell with multiple orthotropic layers under any combination of axial compression and lateral pressure [22]. Jones showed that previous attempts to predict the buckling behavior of multilayered shells were erratic because they neglected the coupling between bending and extension, which his theory considered. He based his work on Donnell's stability differential equations for circular cylindrical shells, with an implied membrane



prebuckled shape and simply supported end conditions.

By applying the Kirchhoff-Love hypothesis, the three-dimensional orthotropic elasticity relations were reduced to two-dimensional stress-strain relations for the  $k^{\text{th}}$  layer. The variations in stresses in the  $k^{\text{th}}$  layer during buckling are

$$\begin{aligned}\delta\sigma_x^k &= Q_{11}^k \delta\epsilon_x + Q_{12}^k \delta\epsilon_y \\ \delta\sigma_y^k &= Q_{12}^k \delta\epsilon_x + Q_{22}^k \delta\epsilon_y \\ \delta\tau_{xy}^k &= Q_{33}^k \delta\gamma_{xy}\end{aligned}\tag{38}$$

and the variations in strains during buckling are

$$\begin{aligned}\delta\epsilon_x &= \epsilon_1 + z\kappa_1 \\ \delta\epsilon_y &= \epsilon_2 + z\kappa_2 \\ \delta\gamma_{xy} &= \epsilon_3 + z\kappa_3\end{aligned}\tag{39}$$

where  $\epsilon_1$ ,  $\epsilon_2$ , and  $\epsilon_3$  are the variations in reference surface strains, and  $\kappa_1$ ,  $\kappa_2$ , and  $\kappa_3$  are the variations in reference surface curvature, such that

$$\epsilon_1 = u_{,x} \quad \epsilon_2 = v_{,y} + \frac{w}{R} \quad \epsilon_3 = u_{,y} + v_{,x}\tag{40}$$

and

$$\kappa_1 = -w_{,xx} \quad \kappa_2 = -w_{,yy} \quad \kappa_3 = -2w_{,xy}\tag{41}$$

Thus the variations in stresses in the  $k^{\text{th}}$  layer can be expressed



$$\begin{aligned}\delta\sigma_x^k &= Q_{11}^k (\epsilon_1 + z\kappa_1) + Q_{12}^k (\epsilon_2 + z\kappa_2) \\ \delta\sigma_y^k &= Q_{12}^k (\epsilon_1 + z\kappa_1) + Q_{22}^k (\epsilon_2 + z\kappa_2)\end{aligned}\tag{42}$$

$$\delta\tau_{xy}^k = Q_{33}^k (\epsilon_3 + z\kappa_3)$$

These variations of stresses over the shell layers during buckling are then integrated to give the variations of forces and moments during buckling;

$$\delta N_x = A_{11}\epsilon_1 + A_{12}\epsilon_2 + B_{11}\kappa_1 + B_{12}\kappa_2\tag{43}$$

$$\delta N_y = A_{12}\epsilon_1 + A_{22}\epsilon_2 + B_{12}\kappa_1 + B_{22}\kappa_2\tag{44}$$

$$\delta N_{xy} = A_{33}\epsilon_3 + B_{33}\kappa_3\tag{45}$$

$$\delta M_x = B_{11}\epsilon_1 + B_{12}\epsilon_2 + D_{11}\kappa_1 + D_{12}\kappa_2\tag{46}$$

$$\delta M_y = B_{12}\epsilon_1 + B_{22}\epsilon_2 + D_{12}\kappa_1 + D_{22}\kappa_2\tag{47}$$

$$\delta M_{xy} = B_{33}\epsilon_3 + D_{33}\kappa_3\tag{48}$$

These force and moment resultants, which account for the coupling between bending and extension, only require four independent material properties,  $E_{xx}^k$ ,  $E_{yy}^k$ ,  $G_{xy}^k$ , and  $\nu_{xy}^k$ , per layer.

L.H. Donnell proposed the following stability



differential equations for circular shells subjected to combined axial compression and lateral pressure [23],

$$\delta N_{x,x} + \delta N_{xy,y} = 0 \quad (49)$$

$$\delta N_{xy,x} + \delta N_{y,y} = 0$$

$$- \delta M_{x,xx} + \delta M_{xy,xy} - \delta M_{yx,xy} - \delta M_{y,yy} + \frac{1}{R} \delta N_y + \overline{N}_x w_{,xx} + \overline{N}_y w_{,yy} = 0 \quad (50)$$

Substituting into these equations, the variations of the in-plane forces per unit length and the variations of the moments per unit length, equations 43-48, together with the previous stress-strain and strain-displacement relationships, equations 40-42, gives three stability differential equations in terms of the displacements,  $u$ ,  $v$  and  $w$ :

$$\begin{aligned} L_{11}u + L_{12}v + L_{13}w &= 0 \\ L_{21}u + L_{22}v + L_{23}w &= 0 \\ L_{31}u + L_{32}v + L_{33}w &= 0 \end{aligned} \quad (51)$$

where  $L_{ij}$  are appropriate partial differential operators, see reference 22.

There are sixteen possible force and geometric boundary conditions of which a combination of four constitutes a defined problem. Our main interest is in simply supported ends, such that,

$$\delta N_x = v = w = \delta M_x = 0 \quad (52)$$



These four conditions are satisfied by the following buckling displacements:

$$\begin{aligned}
 u &= \bar{u} \cos\left(\frac{m\pi x}{L}\right) \cos\left(\frac{ny}{R}\right) \\
 v &= \bar{v} \sin\left(\frac{m\pi x}{L}\right) \sin\left(\frac{ny}{R}\right) \\
 w &= \bar{w} \sin\left(\frac{m\pi x}{L}\right) \cos\left(\frac{ny}{R}\right)
 \end{aligned} \tag{53}$$

where the overline indicates the amplitude. Placing these expressions into equation 51, leaves the following relationship, whose determinant must be zero to obtain a nontrivial solution:

$$\begin{bmatrix} F_{11} & F_{12} & F_{13} \\ F_{21} & F_{22} & F_{23} \\ F_{31} & F_{32} & \left\{ F_{33} - \bar{N}_x \left( \frac{m\pi}{L} \right)^2 - \bar{N}_y \left( \frac{n}{R} \right)^2 \right\} \end{bmatrix} \begin{Bmatrix} \bar{u} \\ \bar{v} \\ \bar{w} \end{Bmatrix} = 0 \tag{54}$$

This results in the following stability criterion, which we shall refer to as "Jones' Equation":

$$\bar{N}_x \left( \frac{m\pi}{L} \right)^2 + \bar{N}_y \left( \frac{n}{R} \right)^2 = F_{33} + F_{23} \left( \frac{F_{13}F_{12} - F_{11}F_{23}}{F_{11}F_{22} - F_{12}^2} \right) + F_{13} \left( \frac{F_{12}F_{23} - F_{13}F_{22}}{F_{11}F_{22} - F_{12}^2} \right) \tag{55}$$

where



$$F_{11} = A_{11} \left( \frac{m\pi}{L} \right)^2 + A_{66} \left( \frac{n}{R} \right)^2 \quad (56)$$

$$F_{12} = F_{21} = (A_{12} + A_{66}) \left( \frac{m\pi}{L} \right) \left( \frac{n}{R} \right) \quad (57)$$

$$F_{13} = F_{31} = \frac{A_{12}}{R} \left( \frac{m\pi}{L} \right) + B_{11} \left( \frac{m\pi}{L} \right)^3 + (B_{12} + 2B_{66}) \left( \frac{m\pi}{L} \right) \left( \frac{n}{R} \right)^2 \quad (58)$$

$$F_{22} = A_{22} \left( \frac{n}{R} \right)^2 + A_{66} \left( \frac{m\pi}{L} \right)^2 \quad (59)$$

$$F_{23} = F_{32} = (B_{12} + 2B_{66}) \left( \frac{m\pi}{L} \right)^2 \left( \frac{n}{R} \right) + \frac{A_{22}}{R} \left( \frac{n}{R} \right) + B_{22} \left( \frac{n}{R} \right)^3 \quad (60)$$

$$\begin{aligned} F_{33} = & D_{11} \left( \frac{m\pi}{L} \right)^4 + 2(D_{12} + 2D_{66}) \left( \frac{m\pi}{L} \right)^2 \left( \frac{n}{R} \right)^2 + D_{22} \left( \frac{n}{R} \right)^4 \\ & + \frac{A_{22}}{R^2} + \frac{2B_{22}}{R} \left( \frac{n}{R} \right)^2 + \frac{2B_{12}}{R} \left( \frac{m\pi}{L} \right)^2 \end{aligned} \quad (61)$$

The buckling load under hydrostatic pressure is obtained by substituting the following load factors:

$$\overline{N}_y = \frac{pR}{t} \quad \overline{N}_x = \frac{pR}{2t} \quad (62)$$



Jones' contribution was instrumental because it introduced the effect of the coupling between bending and extension that exists due to the presence of the multiple orthotropic layers in laminated, composite shells. The more difficult questions of initial geometrical and material imperfections and prebuckling deformations were not considered.

In 1978, M. Booten and R.C. Tennyson conducted a study that considered the behavior of laminated anisotropic cylinders with small axisymmetric shape imperfections [24]. Their analysis used exact boundary conditions and nonlinear prebuckling deformations, and comparisons were made with experimental data. These authors concluded that the effect of varying the fiber angle on the interactive buckling behavior of laminated cylinders with "perfect" geometry and "less than perfect" axisymmetry is significant. In a later work with Hansen [25], Tennyson demonstrated that the buckling strength of an axially loaded cylindrical shell could be increased significantly through a judicious choice of laminate configuration. This has naturally lead to the topic of optimization.

Composite materials offer the designer the ability to tailor material properties to the specific application. In filamentary composites, such as graphite-epoxy, this involves ply angle selection. where designers aspire for the capability to select optimal ply angle distributions for specific



geometries and load conditions. In the past ten years several studies have been conducted into laminate optimization for cylindrical shells.

In 1981, Y.S. Nshanian of the then U.S.S.R. and M. Pappas examined the optimization of the ply angle distribution across the thickness of composite shells for buckling and vibration considerations [26]. They proposed methods to determine the optimal ply angle variation through the thickness of symmetric angle-ply shells of uniform thickness. Using a mathematical programming algorithm, the procedure attempted to maximize the buckling load of a thin, simply-supported, circular, cylindrical, angle-ply shell. Their results showed significant gains using optimal variable ply angle configurations, as compared to ones with an optimal constant ply angle. But reference shells with variable but non-optimal angle-ply configurations ( $0^\circ/90^\circ$  and  $90^\circ/0^\circ$ ) were often near optimal in performance and always superior to optimal conventional angle-ply shells.

In 1987, Sun and Hansen attempted to maximize the buckling load of a laminated-composite, circular-cylindrical shell as a function of ply orientation [27]. They used a two-step optimization routine with a first step random search to determine an initial guess and a second step systematic search based on work by Powell [28]. The optimization routines were applied to the finite difference solutions to von Kàrmàn-Donnell non-linear shell strain-displacement



relations. Experiments were conducted on selected, optimal, four-ply, graphite/epoxy cylinders and compared to certain reference laminates. The experimentally determined buckling load under external pressure for the optimized cylinder was 3.19 times as high as the  $[0/90]_s$  reference cylinder, but no  $[90/0]_s$  reference cylinders, with hoop plies on the outer and inner surfaces, were tested under external pressure.

In 1989, Sun presented another optimization study using linear theory and the same two-step optimization method [29]. The study assumed the cylinders were constructed of  $N$  orthotropic plies with the same thickness, with the  $i^{\text{th}}$  ply containing an equal number of fibers in the  $+\theta_i$  and  $-\theta_i$  directions uniformly distributed through the ply's thickness. This eliminates the stiffness coefficients of the laminate  $A_{16}$ ,  $A_{26}$ ,  $B_{16}$ ,  $B_{26}$ ,  $D_{16}$ , and  $D_{26}$ . This assumption is valid for laminates with many  $+\theta$  and  $-\theta$  plies of thicknesses much smaller than the thickness of the laminate. It serves only as an approximate result for laminates with relatively few plies, such as the 4-ply ones Sun tested and the 12-ply laminates tested here.



## 2.6. Finite Elements Analysis of Composite Shells

In 1984, Abu-Farsakh and Lusher investigated the buckling behavior of glass-reinforced cylindrical shells under combined axial compression and external pressure [30]. Initial imperfections, load-deflection response, and buckling modes and loads were determined experimentally for 20 specimens and compared to the results of a finite element analysis (FEA). The FEA predicted lower buckling loads than were experimentally measured. They concluded that the size of the mesh must produce a higher number of divisions circumferentially than the number of circumferential buckling waves to obtain reasonable results.

As a prelude to the hydrostatic testing outlined in this report, extensive finite element analysis work was completed by T. Perry at the University of Massachusetts, Lowell, Massachusetts [5]. The suitability of three finite element software packages were evaluated for use in this project, EMRC NISA, Algor's SUPERSAP, and HKS's ABAQUS. ABAQUS, which has anisotropic material capability for buckling and non-linear analysis, proved to be the best of the three packages. ABAQUS finite element models for specially orthotropic, orthotropic, quasi-isotropic, and isotropic cylinders were run using the material properties of T300/5208 graphite/epoxy and simply supported boundary conditions. The models were created using 16 circumferential by 10 longitudinal (16c×10l) parabolic 5



degree of freedom/node elements for a total of 2560 degrees of freedom (dof). The FEA gave stiffer results by as much as 25% over the classical analysis using Jones' equation described above. Trends were evident but they were sometimes contrary to those predicted by Jones' analysis. The present experimental test program aims to determine which method, classical analysis or FEA, produces the best results, both in accurately predicting buckling strengths and in the relative ranking of different laminate types.



## 2.7. Southwell-type Analysis of Elastic Stability

In 1932, R.V. Southwell, in an attempt to find "the practical value of a theory of elasticity," proposed a procedure to analyze test data from an elastic column with initial curvature in an effort to determine the buckling characteristics of a perfectly straight column [6]. This procedure was an attempt to validate theories of elastic stability experimentally, realizing that "(1) the finite strength of actual materials, and (2) the unavoidable imperfections of workmanship" prevent the practical realization of elastic stability's concept of a "critical load." In the method, the central deflection of the column was plotted against a load-normalized deflection and the slope of the best straight line drawn through the test data was interpreted as the critical buckling load of the a perfectly straight column. Southwell foresaw that the basic concepts of this method should be widely applicable to structural stability problems wherever "inaccuracies in the specimen or in the experimental apparatus introduce displacements which increase continuously with the load."

Recognizing its wide applicability to elastic stability problems, in 1955, Galletly and Reynolds developed an extension of Southwell's method that could be used to determine the elastic general instability pressure of ring-stiffened cylindrical shells subjected to external hydrostatic



pressure [7]. In this procedure the applied hydrostatic pressure was plotted against the circumferential bending strain that existed largely due to the initial out-of-roundness of the test specimens.

L.H. Donnell concluded back in 1938 that Southwell's straight-line plot method was probably not applicable to curved structures because the deformed shape of curved structures was not a developable surface and the corresponding differential equations would be nonlinear [31]. Galletly and Reynolds showed that although the plot of pressure versus the reciprocal of the bending strain due to out of roundness was not linear, it was so slightly curved as the buckling pressure was approached that it could be closely approximated by a straight line. Another paper, by Horton and Cundari, demonstrated using previously published experimental data and theoretical analysis that the method was "of absolute generality," and they concluded that "theories for perfect bodies ... not in agreement with experimental values derived on the basis of Southwell type plots must be considered inadequate, incomplete or in error." [32]

Galletly and Reynold's method was based on small-deflection theory where displacements and strains grow indefinitely large as the buckling pressure is approached. Because strains are easier to measure experimentally than displacements and intercepts are easier to objectively determine than asymptotic slopes, they plotted the reciprocals



of the strain quantities versus pressure rather than displacement versus pressure like Southwell had originally.

An explanation of the method of applying Southwell's concepts that was used to analyze the strain data from this test program is presented graphically in the next three figures. Figure 2.5 shows some typical circumferential strain data plotted versus the applied hydrostatic pressure. The curved lines show the variation of the circumferential strain with pressure at three individual points on the circumference of a cylindrical specimen ( $0^\circ$ ,  $45^\circ$ , and  $90^\circ$  relative to each other). These curves become hyperbolic as the critical load is approached, but notice that they can be approximated by straight lines for a large portion of their length, as shown by the dashed lines. The slopes of these straight lines are different at each different location around the cylinder due to the varying amounts of local eccentricities. Galletly and Reynolds illustrated that the average of a large number of evenly distributed circumferential strain gage readings closely approximates the axisymmetric circumferential strain predicted by the Equation 13. This membrane strain can be considered as the elastic circumferential strain that would exist in a perfect structure whose radius is being uniformly compressed. The individual circumferential strains that actually occur on the cylinder are due to a combination of this membrane strain and the bending strain induced by the initial local eccentricities in the circular cylindrical shape



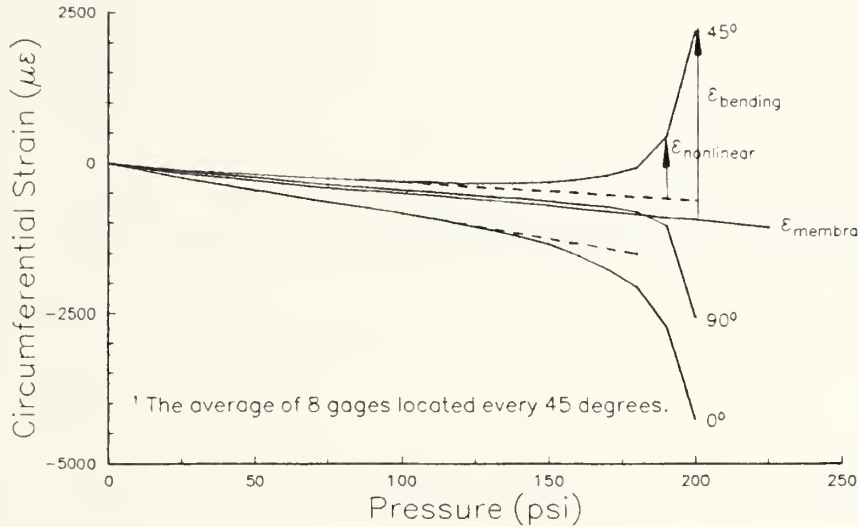


**Figure 2.5.** Typical plot of circumferential strain versus applied hydrostatic pressure, showing extraction of bending and nonlinear strains.

of the structure. We therefore consider the average of the experimental strains as the membrane strain,  $\epsilon_{\text{membrane}}$ , and the difference between this and the actual individual strain gage readings as the local bending strain,  $\epsilon_{\text{bending}}$ , as shown in Figure 2.5.

A plot of the bending strain versus the applied pressure,  $p$ , is nonlinear and  $\epsilon_{\text{bending}}$  asymptotically approaches infinity at certain values of  $p$ , the first of which is the minimum elastic buckling pressure,  $p_{\text{crit}}$ . The other values of  $p$  where  $\epsilon_{\text{bending}}$  becomes infinite do not occur in reality and therefore, a plot of the reciprocal of the experimentally measured bending strain,  $1/\epsilon_{\text{bending}}$ , versus the applied pressure will be curve that intercepts the  $p$ -axis at  $p_{\text{crit}}$ , the minimum buckling



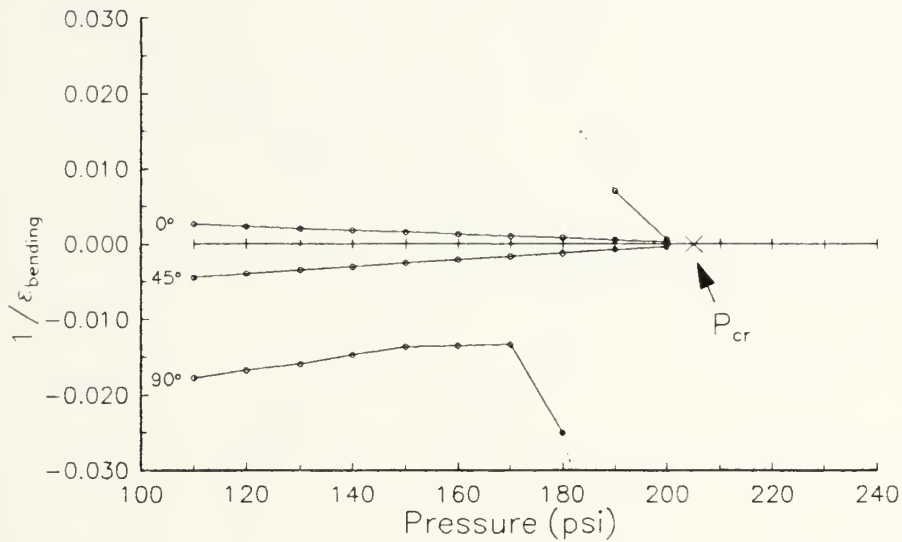


**Figure 2.6.** Plot of  $1/\epsilon_{\text{bending}}$  versus pressure to determine a cylinder's critical buckling pressure.

pressure of a perfect cylinder.

Referring again to Figure 2.5, the gages located at the relative locations of  $0^\circ$  and  $45^\circ$  behave in a manner that makes this method of determining  $p_{\text{crit}}$  feasible. However, the fact that the strains from the gage located at  $90^\circ$  cross the membrane strain line prevents the utilization of data from this gage in this exact method. This is because where  $\epsilon$  equals  $\epsilon_{\text{membrane}}$  the value of  $1/\epsilon_{\text{bending}}$  becomes infinite. The Southwell plot of all three gages where  $\epsilon_{\text{average}} = \epsilon_{\text{membrane}}$  is shown in Figure 2.6.

One way to be able to use the readings from all "good" gages is to plot the reciprocal of only the nonlinear component of the local bending strain, instead of the bending



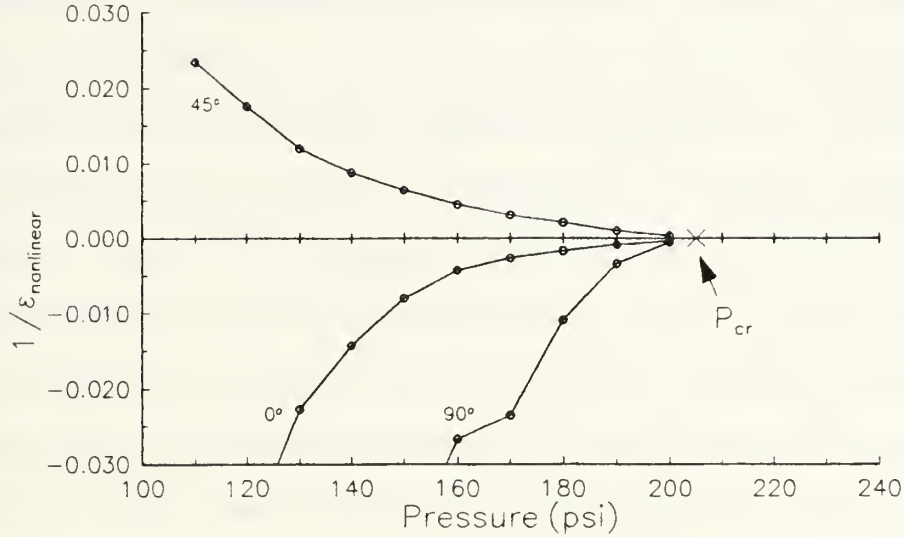


Figure 2.7. Plot of  $1/\epsilon_{\text{non-linear}}$  versus pressure to determine a cylinder's critical buckling pressure.

strain itself. In Figure 2.5, the strain at each gage is noticed to be very linear for the first 50 to 75 psi of pressure. The dashed straight lines are extensions of this linear portion of the strain readings. We can, therefore, break each bending strain response curve into a linear portion and a nonlinear portion we will call  $\epsilon_{\text{nonlinear}}$ , such that:

$$\epsilon_{\text{bending}} = cP + \epsilon_{\text{nonlinear}} \quad (63)$$

Where  $c$  is the constant slope of the dashed line. A plot of  $\epsilon_{\text{nonlinear}}$  versus the pressure also, as expected, becomes infinite at the critical buckling pressure. The three gages of Figure 2.5 were used in this manner to create the plot of  $1/\epsilon_{\text{nonlinear}}$



versus  $p$  in Figure 2.7.

When one recognizes that the above deduction makes no assumptions or references to the material characteristics of the cylinder, the applicability to the difficult problem of laminated fiber reinforced composite cylinders is realized. These methods were used in an attempt to validate previous theoretical and finite element analysis of laminated composite cylinders, using strain data collected from the hydrostatic test of composite cylindrical specimens. Predicting the critical buckling pressure during a test before the onset of failure is also a possibility with this method. It is proposed that a method could be developed whereby strain data from a pressure hull loaded to only a percentage of its predicted buckling load could be used to predict how that cylinder will behave at pressures approaching the critical buckling pressure. Development of a method of this type would enable for hull certification and in-service monitoring to determine degradations from impact damage, cyclic loading, etc.



## 2.8. Buckling Mode Shape Analysis

A method is proposed to determine the buckling mode shape of a circular cylinder using the basic concepts that R.V. Southwell presented for relating the radial displacement of a point on a axisymmetrically compressed cylindrical tube to its change in circumference [33]. For this analysis, the radial displacement is assumed to occur in a plane perpendicular to the longitudinal axis, and the circular cross-section is assumed to remain circular. The fractional contraction of the circumference results in a new radius ( $R-w$ ), and can be expressed as an axisymmetric circumferential strain,

$$\epsilon_y = \frac{2\pi(R-w) - 2\pi R}{2\pi R} = -\frac{w}{R} \quad (64)$$

This can be converted into an expression for the radial displacement in terms of just the nominal radius  $R$  and the uniform circumferential strain  $\epsilon_y$ ,

$$w = -\epsilon_y R \quad (65)$$

The actual circumferential strain at any point on a cylinder being compressed nonuniformly can be broken into a membrane strain that would define the uniform contraction in the radius and a bending strain that would be the local contraction or extension relative to this uniform change. Therefore, by



looking at just the affect of the bending strain at several points around the circumference, an idea of the number of circumferential buckling waves can be deduced.

This method is applied to each of the specimens using the eight circumferential strain gage readings at the last pressure where all gages were recorded prior to buckling failure. To better illustrate the deformed shaped the radial deflections were magnified from 200 to 500 times normal size.

These mode shape plots are contained in Appendix C. The odd-numbered figures contain the variations of bending strain with pressure at the noted locations around the circumference of each specimen and the even-numbered figures contain polar plots of the deduced mode shapes with the magnified radial deflections.

Application of the above analysis to these bending strains and magnifying the radial displacements, even though it does not give absolute deflections, does make the buckling mode shape clearly apparent. This experimentally derived mode shape can then be used directly in the classical and finite element buckling analyses, or as a verification of the analyses' circumferential buckling wave assumptions.



### 3. EXPERIMENTAL PROCEDURE

The main contribution of this thesis is the results obtained from the hydrostatic pressure testing to failure of cylindrical test specimens of various laminate configurations. The purpose of this testing was to experimentally verify the results obtained from classical and finite element buckling analyses. In addition to checking how precisely the analysis methods predict the buckling failure pressures of these relatively simple laminates, these methods must be verified to at least rank the buckling pressures of the different laminate types correctly. The correct ranking is essential to selecting one of these analysis methods as a basis for studies into the optimization of ply orientations for buckling strength.

The test matrix originally called for the testing of at least three 12-ply composite cylinders from each of the four laminate configurations. In all, thirteen cylinders were tested but because of fabrication induced defects only eight specimens were considered "good." The additional 5 defective specimens were tested to failure, but their strain data and comparative value were rejected. These cylinders had noticeable flaws and would normally have been discarded prior to testing, but in order to refine the test set-up and also in an effort to gain an understanding of how these defects affect the failure mechanisms, all were tested, but only the strain data from the good specimens was used in the analysis and



presented in the results.

The strain gage readings taken throughout the hydrostatic tests and the critical buckling loads measured comprise the bulk of the experimental data. The results were tabulated and plotted in various formats, and then analyzed to determine patterns or conclusions about the strength of composite cylinders subjected to external hydrostatic pressure. The experimental results were also compared with the analytical results to check predictions about laminated cylinder buckling strengths and assumptions of buckling mode shapes.

Very little research has been conducted to experimentally determine the behavior of thin-walled composite cylinders of various lay-ups subjected to hydrostatic external pressure to failure, and to compare the results with theoretical predictions. Currently there is only a meager amount of test data on the buckling of thin-walled composite shells under hydrostatic pressure. The data collected and analyzed here is hoped to give a better understanding of the ability to use composites for submersible hull structures. Ultimately, insight is sought into improved ways to select material combinations and laminate configurations that will enable the benefits of laminated composite material technology to be maximized in future design and construction of submersible pressure hulls.



### 3.1. Cylindrical Test Specimens

All of the tested specimens were fabricated from 12-ply laminated circular cylinders with nominal diameters of 5.52 inches, skin thicknesses of 0.072, and lengths of 18 inches.

All the cylinders were constructed of individual plies of T300/5208 graphite/epoxy pre-impregnated unidirectional ply (prepreg uniply). Table 3.1 contains the nominal properties of T300/5208 in this format and the typical properties of various other types of graphite fiber / polymer matrix unidirectional composites, for comparison. These properties were obtained from the Composite Materials Research Group at the University of Wyoming and are for nominal 60% fiber volume composites. Digital micrographs of polished specimens cut from the excess ends of the laminated tubes tested here indicated an average fiber volume of 50%.



Composite Property	AS4/ 3501-6	GY70/ 930	T300/ 5208
$E_{11}$ (Msi)	20.0	47.1	19.0
$E_{22}$ (Msi)	1.3	0.9	1.5
$G_{12}$ (Msi)	1.0	0.6	1.0
$\nu_{12}$	0.30	0.26	0.28
$\alpha_{11}$ ( $10^{-6}/^{\circ}\text{C}$ )	-0.04	-0.48	-0.04
$\alpha_{22}$ ( $10^{-6}/^{\circ}\text{C}$ )	18.0	18.0	18.0
$\sigma_{1t}$ (ksi)	210	110	218
$\sigma_{2t}$ (ksi)	7.5	3.8	5.8
$\tau_{12}$ (ksi)	19.0	3.9	13.9
$\sigma_{1c}$ (ksi)	210	102	218
$\sigma_{2c}$ (ksi)	29.9	5.0	35.7

Table 3.1. Typical Material Properties.

#### A. Fabrication Method

There are several different viable fabrication methods that could have been used to produce the cylindrical specimens for the hydrostatic testing. The primary methods used in the construction of tubes and cylindrical vessels out of laminated composite materials are hand layup with vacuum bag curing, filament winding, and tape winding. Hand layup with vacuum bag curing was not considered to be adequate because it would almost be impossible to control wrinkles and geometric deviations from perfect circularity. As discussed earlier, slight imperfections have a significant effect on the buckling failure characteristics of cylindrical shells in compression.



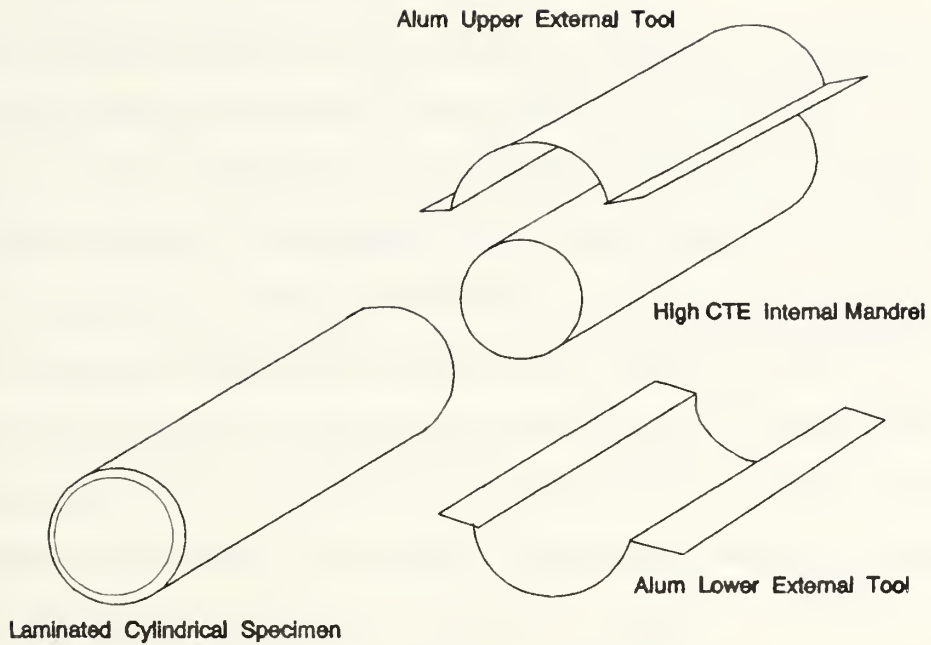


Figure 3.1. The elastomeric tooling fixture used to manufacture the cylindrical test specimens.

These irregularities could be largely eliminated and at least controlled by constructing the specimens with filament winding technique. This fabrication method produces highly circular and wrinkle-free cylinders, but distribution of the fibers could not have been made as uniformly as required. Tape winding, which combines the best attributes of hand layup and filament winding was a technically feasible option, but the cost of a tape winder was prohibitive to project budget constraints. For these reasons, a novel method of constructing the cylindrical specimens with high circularity and minimal laminate defects had to be incorporated. An elastomeric tooling method that involves the use of an expanding internal mandrel and a highly circular external mandrel was chosen to



fabricate the test specimens.

This method calls for an internal mandrel constructed of a high coefficient of thermal expansion (CTE) material which expands in radius during the increased temperature curing cycle. This mandrel is wrapped with thin sheets of elastomer to give a consistent, smooth surface to the final cylinder. Sheets of prepreg uniply are then hand laid up onto the mandrel. The sheets of uniply must be carefully measured, cut and rolled onto the cylinder by one person while the another person makes sure that the lamina lays down smoothly and at the desired angle. After all plies are applied to the internal mandrel, two highly accurately machined semi-circular metal external tools are clamped on. The pressure exerted during the curing process by the expanding high CTE internal mandrel forces the multiple layers of uniply tape up against the stiff, low CTE external tool.

This method proved to consistently create laminated cylindrical specimens with extremely close circular tolerances. The details of the elastomeric tooling fixture used to manufacture the specimens for this research is diagrammed in Figure 3.1. It has an internal mandrel made of a syntactic foam core ( $CTE = 28 \times 10^{-6} \text{ in/in}^\circ\text{F}$ ) that is wrapped with several layers of silicone rubber sheet ( $CTE = 162 \times 10^{-6} \text{ in/in}^\circ\text{F}$ ), and an external tool fabricated from two 1/2" thick, 24" long aluminum pipe halves ( $CTE = 14 \times 10^{-6} \text{ in/in}^\circ\text{F}$ ) which were bored to a .005" circular tolerance.



## B. Laminates Tested

The cylinders each had twelve plies and were constructed out of one of the four following different layups:

$[90_4/0_2]_s$  - 2:1 specially orthotropic

$[90_3/0_3]_s$  - 1:1 specially orthotropic

$[90_2/(\pm 30)_2]_s$  - quasi-isotropic

$[90_2/0]_{4T}$  - interleaved orthotropic

The numbers indicate the orientation of the individual plies, the numerical subscripts indicate the number of plies of that orientation, the alphabetic subscript S indicates that the laminate is symmetrical about the mid-surface, and the 4T indicates that the unsymmetric laminate is constructed of 4 identical plies. Each of these laminates are diagrammed in Figures 2.2, 2.3, 2.4, and 2.5.



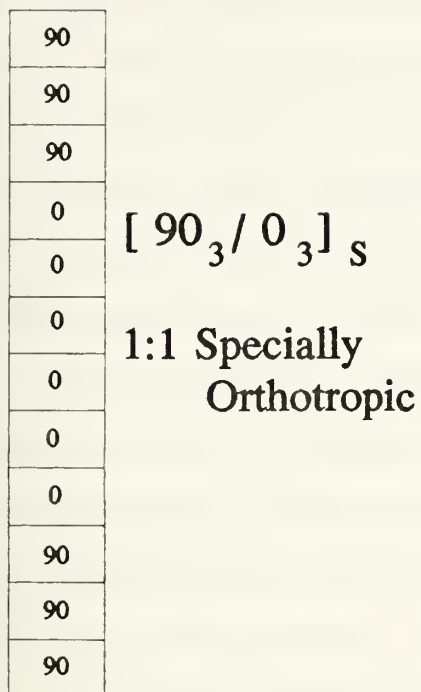


Figure 3.2.

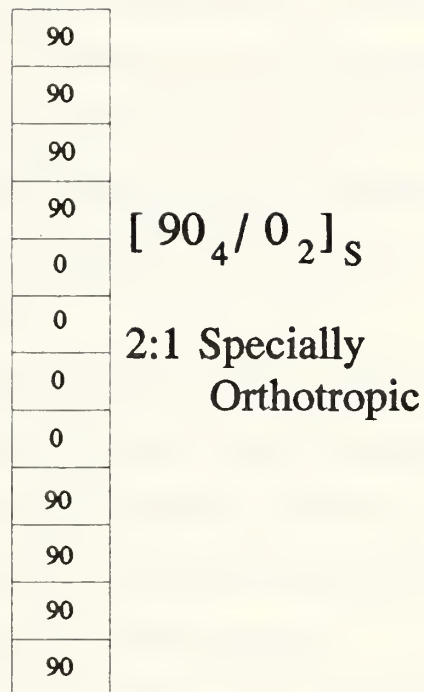


Figure 3.3.

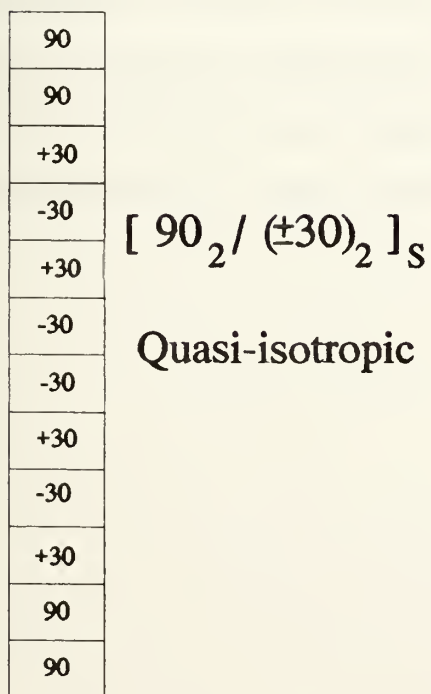


Figure 3.4.

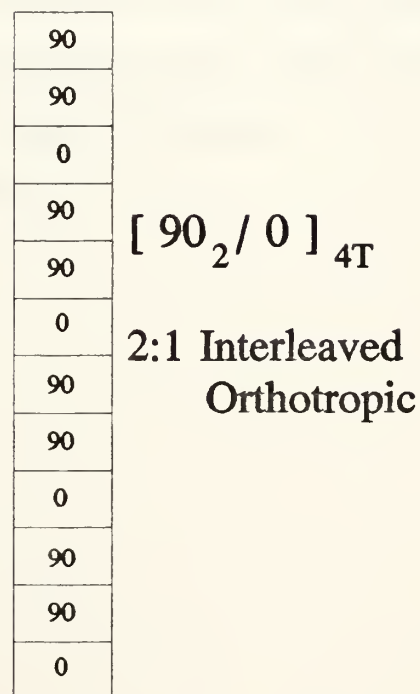


Figure 3.5.



The 1:1 and 2:1 specially orthotropic laminates do not exhibit any stiffness coupling and, therefore, are the easiest of the anisotropic laminates to analyze. This also means that the material does not warp or twist during post-cure cooling. This is not as much of a problem with cylinders as flat plates, but was a concern nonetheless.

The unsymmetric, interleaved orthotropic layup, which is commonly used in industry, has somewhat better interlaminar properties than the specially orthotropic laminates because the perpendicular ply interfaces are distributed through the thickness. This causes a reduction of the interlaminar stresses that cause delamination, a major failure mechanism in laminated composites.

The quasi-isotropic layup was used to compare the composite cylinder failure characteristics to cylinders made from isotropic materials. Laminates made with this type system of ply orientations result in directional stiffness characteristics very close to isotropic.



### 3.2. Hydrostatic Pressure Tests

#### A. Test Set-up and Instrumentation

The hydrostatic testing was conducted in an Atlas 600 psi air pressure chamber located in the Mechanical-Thermal Lab at C.S. Draper Laboratory in Cambridge, MA. Pressure was provided to the chamber via a pressure control system that was accurate to within  $\pm 2$  psi. The cylinders were potted at both ends in specially designed endcaps. The endcaps, shown in figure 2.6, were designed with a slot for potting that has an angled outside edge so that the edges remained circular, and also so that only the outside edge of the tube would actually be in contact with the endcap. Armstrong C7 epoxy was used to pot the tubes in the endcaps. This epoxy was compliant enough to allow the ends of the cylinders to rotate when loaded, simulating simply supported edge conditions.

Each specimen was instrumented along the centerline with 10 Micro Measurements  $\frac{1}{2}$  inch, 120  $\Omega$  strain gages, model number EA-06-500BH-120. Eight of the gages were evenly distributed at 45° separations around the centerline of the specimen, and oriented to read circumferential or hoop strain. The other two gages were positioned on the centerline opposite each other at a 180° separation, and oriented to read axial strain. The gage leads were draw out of the pressure chamber, via breakout boxes, to a ten channel BLH Model 1225 switching and balancing unit, and then to a BLH Model 1200 digital strain indicator.



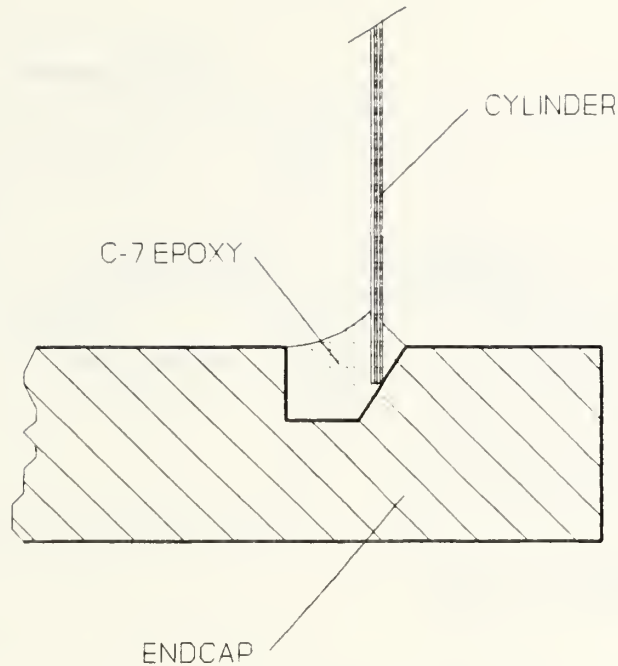


Figure 3.6. Details of cylinder potted in endcap.

The test set-up is diagrammed in Figure 3.7 and a photograph of the facilities is provided in Appendix E.

#### B. Test Procedure

The testing of each cylindrical specimen was conducted by the following procedure:

- o The specimen was placed in the chamber, the strain gage leads were connected to the breakout box, the gages tested for integrity, and a copper bleed-off line was connected to one of the endcaps.
- o The pressure chamber was closed and sealed, and each of gages was manually zeroed with the switching and balancing unit.
- o The pressure in the chamber was increased to 25 psi and



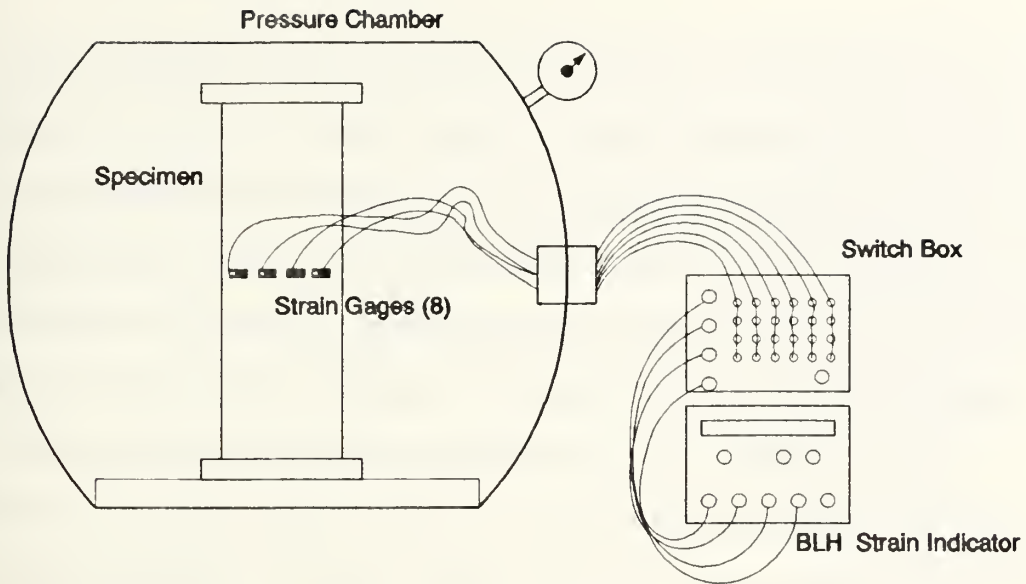


Figure 3.7. Diagram of experimental set-up, showing pressure chamber and instrumentation.

maintained long enough for strain readings to stabilize and to be manually recorded for each individual gage.

o The pressure was increased to 50, 75, 100, 110, and so on at 10 or 5 psi increments until failure, taking readings at each step.



### 3.3. Ring Tests

The external tools that were used in fabrication of the cylinders were 24 inches long but the specimens were only to be 18 inches long. This left 3 inches of excess on each end of the cylinder. Several 1/2 inch rings were cut from the excess end of each cylinder, and these were used to help determine some of the in situ material properties of the specimens.

Two strain gages were applied at the same angular location of each ring, one on the inside and the other on the outside surface, 90° from the point of load application. The rings were then loaded in two point compression on the Instron® 4505 located in the Composite Materials Laboratory of the Material Science and Engineering Department at the Massachusetts Institute of Technology, Cambridge, MA. Measurements of strain and displacement versus load were recorded throughout each of the tests. The data acquisition system consisted of a four channel Micro Measurements strain gage conditioner unit, model 1220A, and a National Instruments Lab-PC integrated data acquisition card.

These ring tests gave some additional mechanical property data for the various laminate configurations in the "as fabricated" condition.



## 4. RESULTS and DISCUSSION

### 4.1. Ring Tests

Throughout the two-point, symmetric compression test of the each 1/2 inch ring, load, strain and displacement data was collected. Plots were made of the load versus displacement and the load versus strain data. The slopes of the load versus displacement curves were used with the relationship of equation 28 to calculate a "w test"  $D_{22}$  for each of the ring specimens. Additionally, the slopes of the strain versus displacement curves were used with the relationship of equation 31 to calculate an " $\epsilon$  test"  $D_{22}$ . These experimentally determined  $D_{22}$ 's were compared with the  $D_{22}$  from CLT contained in the ABD matrices of Appendix E, which were developed using the material properties for T300/5208 given in Table 3.1. This comparison is summarized in Table 4.2 below. The experimental "w-test" and " $\epsilon$ -test" values are seen to agree well with each other, and are in reasonable agreement with the values calculated using CLT.

Because the radius, thickness and width of the ring specimen has a significant impact on equation 31, these dimensions were accurately measured with a micrometer at eight locations around the ring and the average of these values used in calculations. These averaged values for  $R$ ,  $t$  and  $b$  are presented in Table 4.1.



Specimen No.	R [in.]	t [in.]	b [in.]
6	2.759	0.072	0.523
9	2.761	0.070	0.503
12	2.757	0.074	0.516
13	2.759	0.072	0.505
17	2.758	0.077	0.510
18	2.757	0.076	0.506
23	2.760	0.075	0.507

Table 4.1. Dimensions of Ring Specimens.

Specimen No.	P/w	P/ε	D <sub>22</sub> w-test	D <sub>22</sub> ε-test	D <sub>22</sub> CLT
6	147.1	12650	440.1	436.6	526.2
9	116.3	10100	361.6	352.1	526.2
12	128.3	10520	387.5	377.4	574.4
13	134.9	11180	417.5	399.6	574.4
17	126.0	9278	385.9	351.1	445.7
18	147.0	11400	453.3	428.9	445.7
23	93.4	8623	288.5	319.9	407.0

Table 4.2. Predicted and Measured D<sub>22</sub>.



## 4.2. Cylinder Tests

A total of 13 full-length cylindrical specimens were tested to failure, but several of these had noticeable defects and thus only served to refine the test procedure and gain more experience with the graphite/epoxy pressure vessels with large defects. Table 4.3 contains a breakdown of the specimens tested and their critical buckling pressures. This table also gives comments on each "bad" specimen, explaining the details of the problem, such as any noticeable flaws. In all, eight specimens have been tested that were classified as "good". Only the buckling pressures and strain data from these eight specimens were analyzed for this investigation.

#	Type	P <sub>crit</sub>	Notes and Comments	Class
5	1:1	140	Tested with conical steel endcaps.	bad
6	1:1	183		good
7	1:1	95	Creased when clamped into tool.	bad
8	1:1	160	Creased when clamped into tool.	bad
9	1:1	200		good
10	2:1	167	Coated in epoxy due to leakage.	bad
12	2:1	181		good
13	2:1	173		good
15	Unsym	67	[0 <sub>2</sub> /±60 <sub>4</sub> /0 <sub>2</sub> ] <sub>T</sub> . Used steel endcaps.	bad
16	Quasi	165		good
17	Quasi	183	Loaded 50 psi, unloaded, reloaded.	good
18	Quasi	175		good
23	Unsym	152		good

Table 4.3. Summary of all tested specimens.



The original endcaps were designed with large cones to seat the cylinder edges onto and were constructed out of steel. Reproducible end conditions were extremely difficult to create using these steel endcaps. Specimens 5 and 15 were the first two cylinders tested and the conical endcaps were used. The cones on the endcaps seemed to wedge into the cylinders under pressure creating erroneous results. These problems inspired the development of a new endcap design. The details of the potting of the cylinders in these endcaps are shown in Figure 3.6. Because of the change in endcaps the results from the first two cylinders tested were discarded.

Specimen 10 was a very "dry" laminate and had excessive leakage through the plies themselves. This specimen was coated in C-7 epoxy to prevent the pressure from equalizing inside the cylinder and enable testing to be completed. Because of this coating, the results were not considered accurate.

During the manufacture of specimens 7 and 8 the pre-cured laminate that was rolled onto the internal mandrel was too large for the aluminum external tools to be clamped around. These specimens were put into a freezer to induce shrinking and then forcibly clamped into the tools. Both these specimens had creases of the order of the laminate thickness from the pinching of the semicircular aluminum tools. Failure of these specimens under hydrostatic loading was premature and both fractured cleanly down the creases as shown in the photographs in Appendix F. For this reason these specimens were not used



for comparative purposes.

Table 4.4 summarizes the critical buckling pressures that were obtained from Jones' equation, ABAQUS modelling, experimental testing, and Southwell-type analysis for the "good" specimens.

Although the test matrix was not as large as originally planned, "good" data was obtained for two 1:1 specially orthotropic, two 2:1 specially orthotropic, three quasi-isotropic, and one interleaved (unsymmetric) orthotropic specimen. Because of the close similarity between the data from each of the "good" specimens from the same layup, these results can be confidently used to evaluate the analysis methods.

Layup	Cylinder	Jones'	ABAQUS	Test	Southwell
$[90_3/0_3]_s$	6	214	194	183	200
$[90_3/0_3]_s$	9	214	194	200	200
$[90_4/0_2]_s$	12	196	204	181	188
$[90_4/0_2]_s$	13	196	204	173	177
$[90_2/(\pm 30)_2]_s$	16	185	172.5	165	167
$[90_2/(\pm 30)_2]_s$	17	185	172.5	183	183
$[90_2/(\pm 30)_2]_s$	18	185	172.5	175	179
$[90_2/0]_{4r}$	23	164	197	152	155

Table 4.4. Predicted and Measured Critical Buckling Pressures.

#### A. Critical Buckling Pressures

As stated earlier, a major objective of this work is to



verify which of the analysis methods not only best predicts the buckling characteristics, but consistently correctly ranks the stability of each of the laminates used. This latter objective is crucial as these methods are proposed for further studies into optimizing the orientations of the plies in a multi-layered composite cylinder to achieve the highest buckling strength.

Figures 4.1, 4.2, 4.3 and 4.4, contain bar graphs which each present the ranking of the four different laminate types. Figure 4.1 gives the values obtained using Jones' buckling criterion, equation 56, which was derived from Donnell's stability equations and CLT. Figure 4.2 are the values given by the FEA program ABAQUS. Figure 4.3 presents the average critical pressure for each laminate type predicted by the Southwell-type analysis, taken from the plots in Appendix B. Figure 4.4 gives the average experimental buckling pressures for each laminate type as obtained from the hydrostatic tests of the "good" specimens.

These figures show that the ABAQUS finite element analysis program does not rank the laminates correctly. This is a major obstacle to using ABAQUS to optimize the selection of individual ply orientations. The ABAQUS analysis predicts that the orthotropic laminates with two hoop plies for every axial ply will have the greatest buckling strength. It predicts that the 2:1 symmetric specially orthotropic laminate is strongest and that the interleaved, unsymmetric orthotropic



laminate will have a higher critical buckling pressure than either the 1:1 specially orthotropic or the quasi-isotropic laminates. This was not corroborated by the testing.

The Jones' equation analysis predicted that the 1:1 specially orthotropic laminate would give the cylinder the greatest buckling strength, followed by the 2:1 specially orthotropic, the quasi-isotropic, and then the interleaved orthotropic laminates, respectively. This ranking was exactly the same order as the critical pressures measured in hydrostatic tests and predicted by the subsequent Southwell-type analysis. This is a significant finding. Applying optimization techniques to the classical analysis methods of Jones will be much less expensive than to apply similar techniques to the finite element methods of the ABAQUS program. That these classical methods have been shown to correctly rank at least the popular laminate types tested here, means that designers can apply them to optimization studies with a substantial amount of confidence.



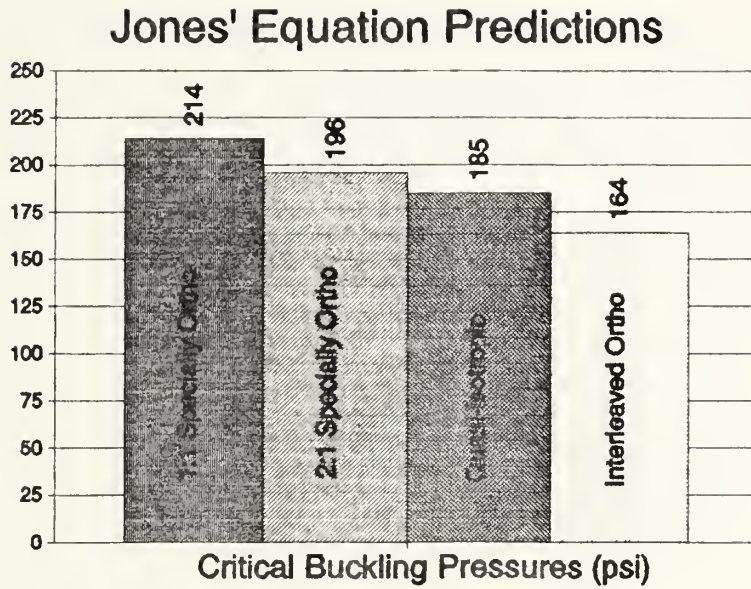


Figure 4.1. Laminate ranking using Jones' Equation.

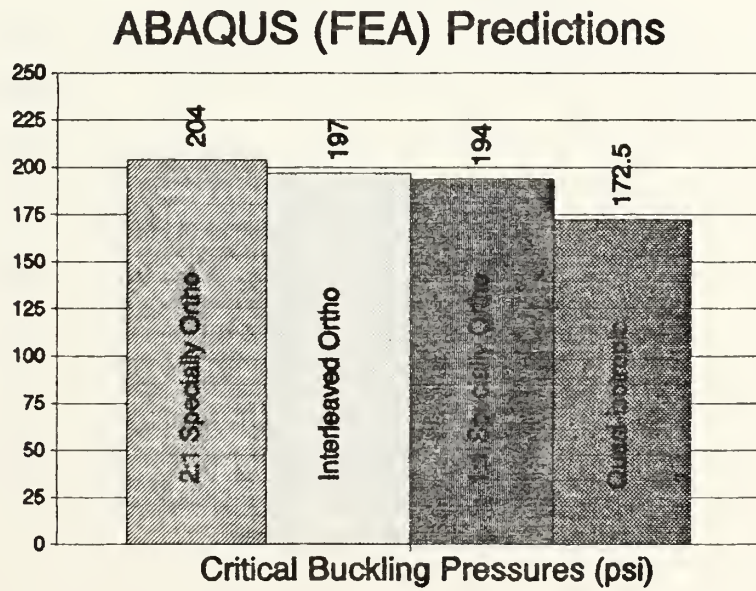


Figure 4.2. Laminate ranking using ABAQUS.



## Southwell Analysis Predictions

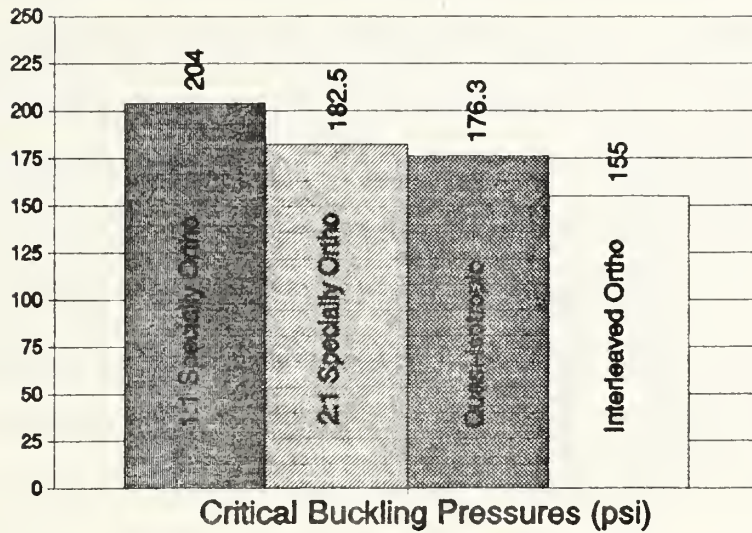


Figure 4.3. Laminate ranking using Southwell-type analysis.

## Average Test Results

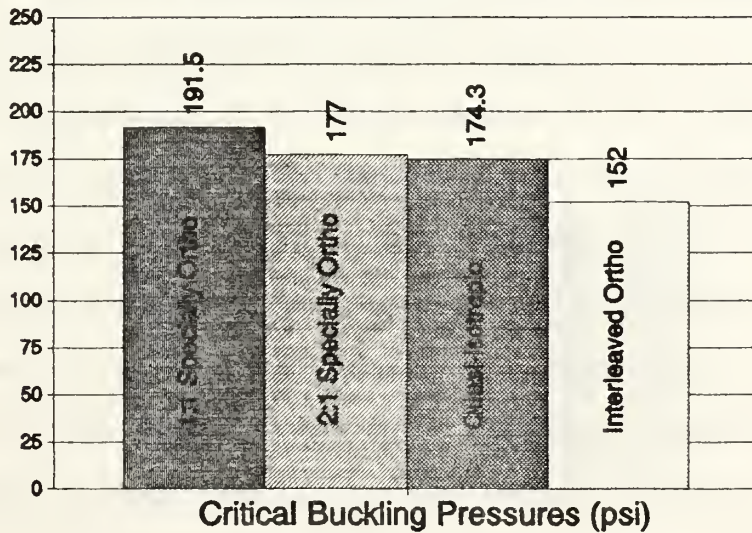


Figure 4.4. Laminate ranking using the results of hydrostatic testing.



Next, the actual critical pressures from the hydrostatic tests are compared to the buckling pressure predictions to verify the accuracy of the various analysis methods. Figures 4.5, 4.6, 4.7 and 4.8 contain bar graphs which each present one laminate type and show a quantitative comparison of the different buckling pressures predicted by the three analysis methods and obtained from hydrostatic testing.

The ABAQUS program was very accurate in its prediction for the cylinders constructed out of the 1:1 specially orthotropic and the quasi-isotropic laminates, but the magnitude of the overestimation of the buckling strength for the 2:1 specially orthotropic and interleaved, unsymmetric orthotropic laminate cylinders prevents this finite element method from being used with any confidence to predict the critical pressures of angle ply laminated cylinders.

Jones' equation gives predictions of the buckling strength larger than those measured experimentally, but within reasonable deviation. It is significant to note the precision and accuracy with which the Jones' equation and the average Southwell-type analysis exhibit, relative to each other. Table 4.5 contains the results of these two analyses which both consider the strength of a "perfect" geometry circular cylinder. It should be noted that the Jones' predictions were for 60% fiber volume laminates, and recently taken digital micrographs of the specimens indicate an average 50% fiber volume. Recalculations using the updated laminate properties



show that the values obtained from the two methods are actually in even better agreement.

Laminate Type	Jones' Equation	Southwell Plot	Percent Difference
1:1 Specially Orthotropic	214	200	+ 7.0 %
2:1 Specially Orthotropic	196	182.5	+ 7.4 %
Quasi-isotropic	185	176	+ 5.1 %
Interleaved Orthotropic	164	155	+ 5.8 %

Table 4.5. Comparison of Jones' Equation and Southwell Plot.



## 1:1 Specially Orthotropic

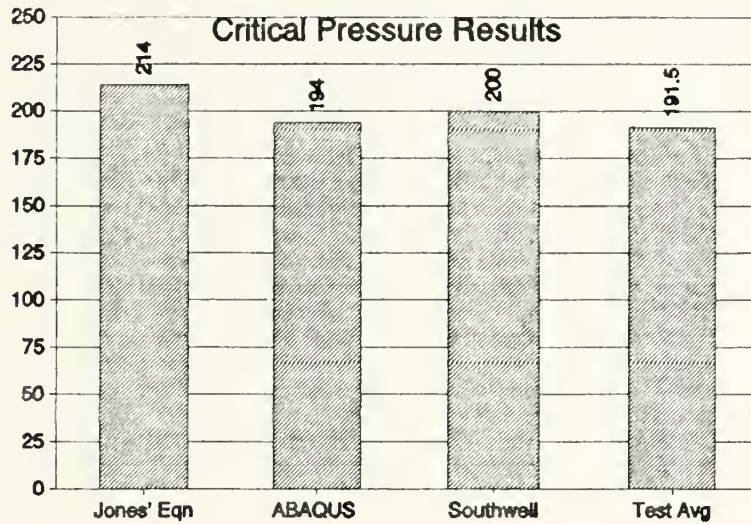


Figure 4.5. Critical buckling pressures for 1:1 Specially Orthotropic laminates.

## 2:1 Specially Orthotropic

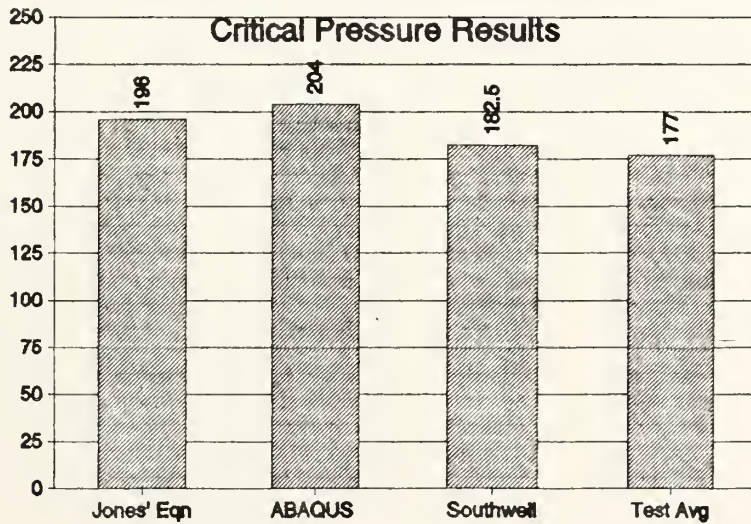


Figure 4.6. Critical buckling pressures for 2:1 Specially Orthotropic laminates.



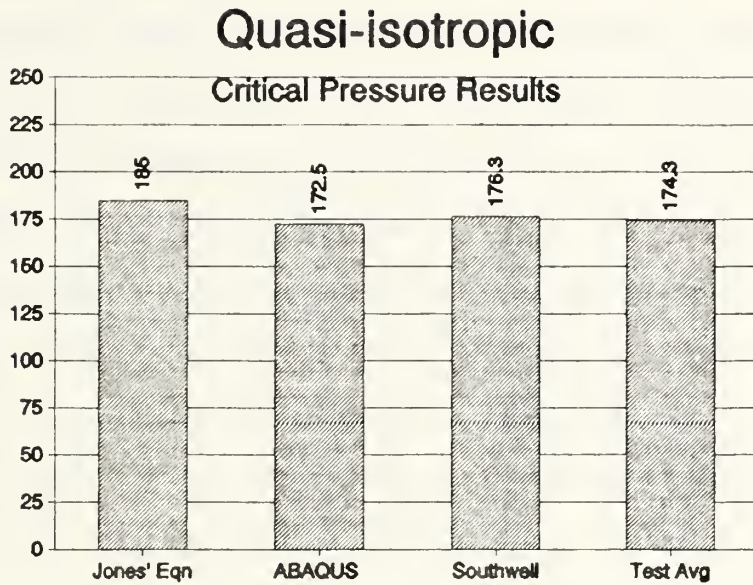


Figure 4.7. Critical buckling pressures for Quasi-isotropic laminates.

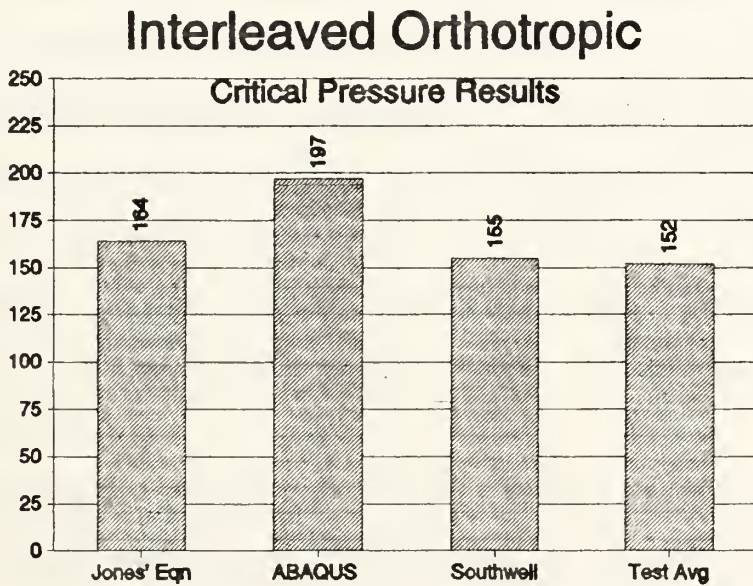


Figure 4.8. Critical buckling pressures for Interleaved Orthotropic laminates.



## B. Axial Strain Response

It was hoped that the two axially mounted strain gages could be used to investigate the beam-column effect of the long cylindrical specimens. The plots of the axial strain responses for all of the good specimens are contained in the even-numbered figures of Appendix A. The axially strains for the 1:1 specially orthotropic specimens seemed to be quite linear with little or no increase in curvature as the critical pressure was approached. The plots of the axial strain response for the 2:1 specially orthotropic, quasi-isotropic, and interleaved (unsymmetric) orthotropic specimens showed the more traditional hyperbolic shape at increased pressures.

## C. Circumferential Strain Response

Plots of the circumferential strain responses from the strain gages located on each of the specimens are contained in the odd-numbered figures of Appendix A. All the cylinders had eight circumferentially-mounted strain gages evenly distributed around the centerline at 45° separations. Note that when one of the plots has less than eight circumferential strain curves, it means that one or more of the gages failed during the test.

The hyperbolic curvature of the circumferential strain response measured by each of the gages, as predicted by theory, is clearly evident in all cases. The individual circumferential strain responses to increasing hydrostatic



pressure can be broken into a membrane and a bending strain response. The bending strain results from the shape change of the circular cylinders' cross-section as the buckling pressure is approached.

This excellent circumferential strain data is a significant contribution of this research, and proved well-worth the time-intensive labor it required to apply the gages, and then to collect and analyze the extensive amount of data that was yielded. Because the eight circumferential strain gages were evenly distributed around each cylinder's centerline, they provided the necessary data to construct detailed Southwell-type plots and to perform an analysis to deduce the buckling mode shape for each cylinder.

#### D. Average Circumferential Strain

By averaging the readings of the eight circumferential gages at each pressure we get a close approximation of the axisymmetric circumferential membrane strain of each of the cylinders as they were compressed. This is the strain response that would exist if the cylinders' cross-section would remain circular throughout the loading.



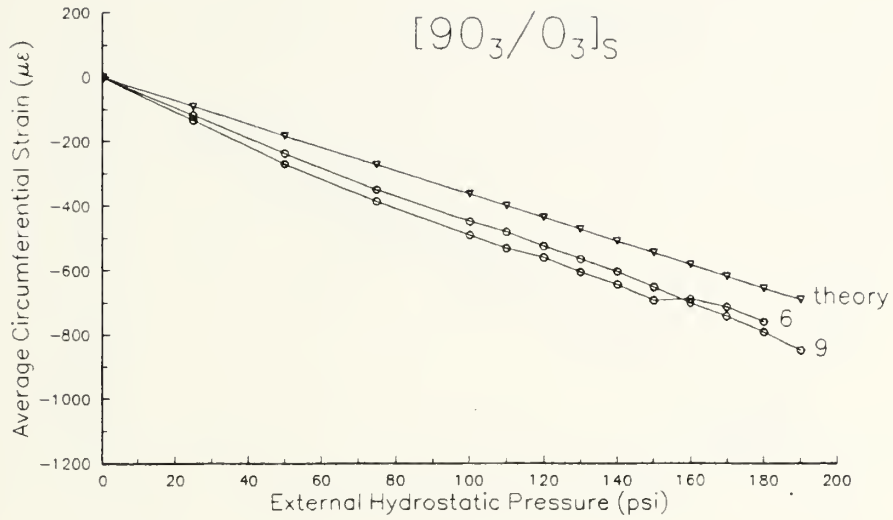


**Figure 4.9.** Axisymmetric circumferential membrane strain response for the 1:1 specially orthotropic cylinders.

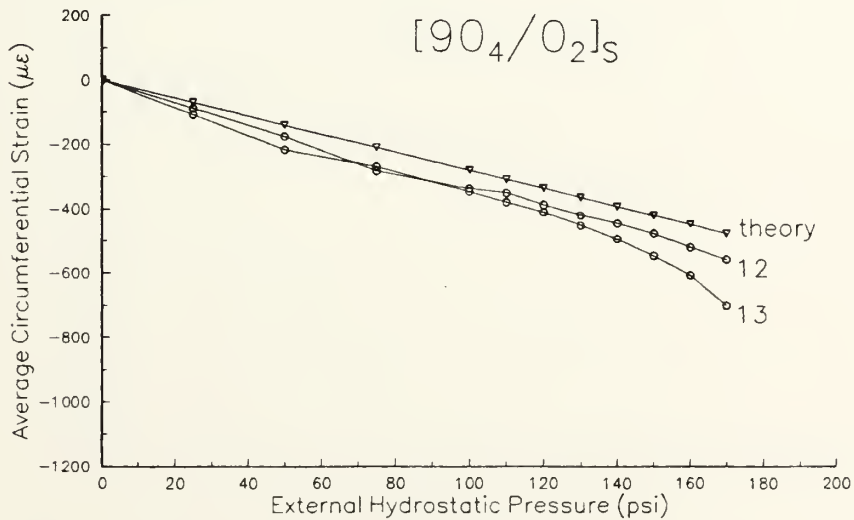


**Figure 4.10.** Axisymmetric circumferential membrane strain response of the 2:1 specially orthotropic cylinders.



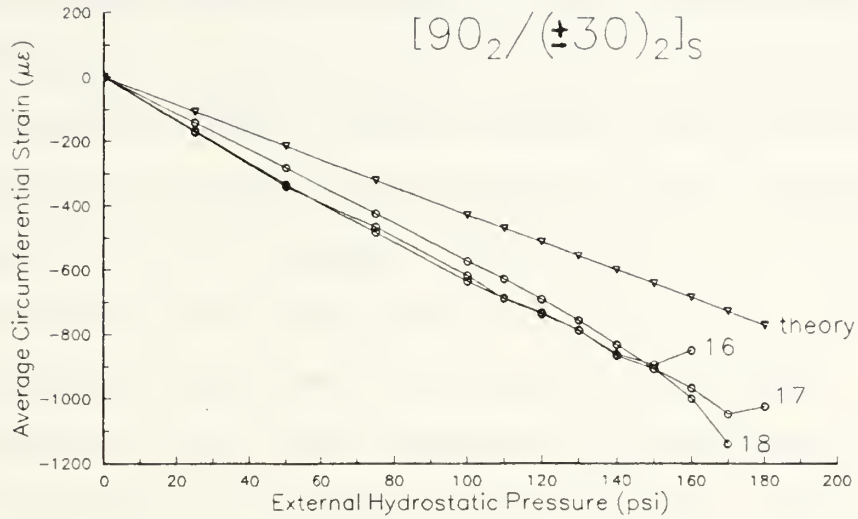


**Figure 4.11.** Axisymmetric circumferential membrane strain response for the quasi-isotropic cylinders.

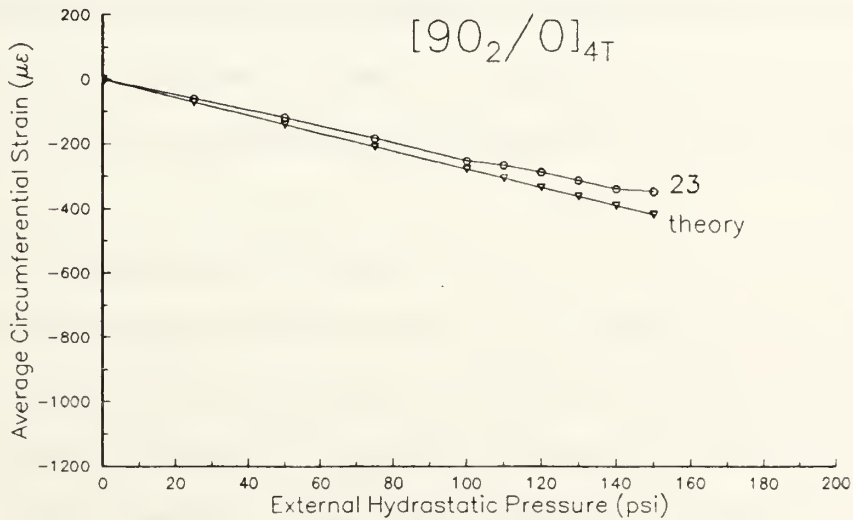


**Figure 4.12.** Axisymmetric circumferential membrane strain response for the interleaved orthotropic cylinder.



To examine how accurately the averages of the eight circumferential strain gage readings approximate the membrane strain, the experimental average of the circumferential strain gage readings is compared to the theoretical axisymmetric circumferential membrane strain response predicted by equation 9 for hydrostatic loading. The curves for each specimen and the theoretical curve for each laminate type, are contained in Figures 4.9, 4.10, 4.11 and 4.12.

These plots show that the average of the eight circumferential strain gage readings from specimens made from the same laminate, are almost exactly the same. These average strains also compare extremely well with the axisymmetric, circumferential membrane strain calculated using the material properties for T300/5208 with 60% fiber volume and equation 9, which is based on CLT. The slight discrepancy could be the result of the fact that the laminates actually had only a 50% fiber volume, not 60% as assumed in the material properties. Additionally, equation 9 does not consider the bending response or the extension/shear coupling in the laminate.

#### E. Modified Southwell Analysis

Using the method described in the section on Southwell analysis, where the reciprocal of the non-linear strain has plotted versus pressure, Southwell-type plots were constructed for each good specimen. The odd-numbered figures of Appendix B show the Southwell plots for each of the specimen over the



same large range of pressure. The even-numbered figures of Appendix B show the details of the Southwell method by displaying only a narrow range of concern for each specimen. The dotted lines on these plots are the extensions of the reciprocals of the non-linear strain curves. Close examination of these plots show the extraordinary small amount of scatter that was involved in the prediction of critical buckling pressures. The values of these predicted buckling pressures for the specimens had they been of perfect geometry is given in the tables and bar charts earlier in this chapter. As noted before, the predictions of Jones' equation were consistently only between 5 to 7.5 percent higher than those obtained from the Southwell plots.

#### F. Mode Shape Deduction from Bending Strains

Using the method outlined in the section on Mode Shape Analysis, the bending strains of each specimen were utilized to deduce the buckling mode shape of each cylinder. The plots of the bending strains and the subsequent variations in shape are contained in Appendix C. The buckling mode shapes are drawn at the last pressure where all the strain gages were read and recorded.



Layup	Specimen	Mode Shape Deduction		
		Test	CLT	FEA
$[90_3/0_3]_s$	6	3	3	2
$[90_3/0_3]_s$	6	3	3	2
$[90_4/0_2]_s$	12	3	3	2
$[90_4/0_2]_s$	13	3	3	2
$[90_2/(\pm 30)_2]_s$	16	3	3	3
$[90_2/(\pm 30)_2]_s$	17	3	3	3
$[90_2/(\pm 30)_2]_s$	18	3	3	3
$[90_2/0]_{4T}$	23	3	3	3

Table 4.6. Predicted and Experimentally Deduced Mode Shapes.

It is significant that each and every specimen, regardless of laminate type, appeared to buckle in a distinctive  $n = 3$ , three lobe mode shape. This was predicted by Jones' equation for all cases, whereas the FEA predicted  $n=2$  to be the lowest energy buckling mode shape for both the 1:1 and 2:1 specially orthotropic cases.

#### G. Failure Progression

The 5208 epoxy matrix used in the laminates tested in this investigation is a very brittle resin, having a low toughness and high modulus (1.4% failure strain). Brittle resins tend to be unable to resist the propagation of delamination, exhibiting quite sudden and uncontrollable failures.

The failure of these T300/5208 laminated cylinders was



exceptionally catastrophic, appearing to happen in microseconds. Attempts were made to film the collapse of the cylinders with a high-speed (250 frames per second) video camera, but even when slowed to one frame per second for viewing the failure sequence was too fast to capture on film.

All the good specimens shattered spectacularly, leaving only very small pieces of intact laminate, large quantities of individual broken fibers, and basically only a dust residue of the resin. Both the specimens that were creased during fabrication (cylinders 7 and 8) fractured cleanly along the crease, leaving large sections of the cylinder relatively intact.



## 5. SUMMARY AND CONCLUSIONS

The hydrostatic tests conducted for this thesis have been successful in achieving the original objectives.

The classical and finite element buckling analysis methods were examined for accuracy and correctness in determining the critical buckling pressure of unstiffened laminated composite cylinders of various layups. From this examination, Jones' equation for the buckling of generally orthotropic cylinders has proven accurate in predicting the buckling loads and correct in the ranking of different laminate types. The validity of this equation which has been experimentally verified, and its relative simplicity make it well-suited for use in optimization programs that could be run economically on personal computers.

A systematic test program was developed whereby cylindrical specimens can be hydrostatically tested to buckling failure under repeatable conditions. The instrumentation used yielded valuable strain data that was used in Southwell-type analysis and also in determining the buckling mode shape of the specimens.

Comparison of the Southwell plots and the Jones' equation predictions, showed the consistency with which this type analysis of circumferential strain data from the test of geometrically imperfect specimen can be used to predict the buckling strength of perfect cylinders. The applicability,



which had previously been shown for isotropic ring-stiffened cylinders, has proven to be applicable to unstiffened cylinders constructed of laminated anisotropic materials as well.

Through careful documentation of the fabrication process and through the utilization of a large diversity of material characterization tests, insight into the role fabrication induced imperfections, residual and interlaminar stresses play in the degradation of pressure hull performance has been gained. In addition, ring compression tests have shown that the bending stiffnesses predicted by classical laminate theory may for symmetric laminates be exaggerated.



## 6. RECOMMENDATIONS

This testing and analysis has shown the large increase in knowledge that can be gained by the extensive strain gage instrumentation. It is recommended that in future testing the pressure be steadily increased and the strains be recorded continuously on a computer data acquisition system. In these tests, the pump on the chamber would kick on and off with quite violent jolts attempting to maintain a steady pressure. This disrupted the stabilization of the strain gages and caused delays before readings could be recorded. The effect of these shocks and delays on the tubes, which is unquantifiable, would be eliminated with continuously increasing pressure loading.

It is believed that by modifying the Southwell and mode shape analysis procedures presented here that a practical method could be developed whereby the compressive buckling strength of individual pressure hulls could be qualified. A properly instrumented pressure hull, tested to only a percentage of its predicted collapse load, would exhibit strains and displacements that may enable the non-destructive verification of predicted collapse loads.

This test series should be extended to angle-ply laminates to check Jones' equation's accuracy for non-orthotropic ply orientations. Notwithstanding the lack of angle-ply testing conducted here, it is recommended that



Jones' equation be utilized in laminate optimization investigations in lieu of finite element methods, which have shown to improperly rank the buckling strength of even the simple laminates tested here.

Graphite/epoxy laminated thin cylindrical shells such as those tested here, have shown to have potential in the design of small submersibles that are only required to operate at shallow depths. It is recommended that in order to avoid catastrophic failure of the hull structure, and subsequent complete loss of the vehicle, that utilization of tougher resins be investigated.



## REFERENCES

1. Gorman, J.J., "Technical Plan for DFY 91 CSR Project C20: Deep Submersible Structures," C.S. Draper Laboratory, Cambridge, MA, August 1990.
2. Smith, C.S., Design of Marine Structures in Composite Materials, Elsevier Science Publishers Ltd., London, 1990.
3. Henault, Mark R., "Buckling and Stress Analysis of a Non-axisymmetric Pressure Hull," Mechanical Engineering Masters Thesis, Massachusetts Institute of Technology, Cambridge, MA, June, 1991.
4. Garvey, R.E., "Hydrotested Thick Composite Cylinders," Proceedings of the 4<sup>th</sup> Annual Thick Composites in Compression Workshop, Knoxville, TN, 1990.
5. Perry, Thomas G., "Laminate Optimization of Advanced Composite Cylindrical Shells to Improve Buckling Characteristics Under External Pressure," Mechanical Engineering Masters Thesis, University of Massachusetts, Lowell, MA, 1992.
6. Southwell, R.V., "On the Analysis of Experimental Observations in Problems of Elastic Stability," Proceedings of the Royal Society, Vol. 135A, 1932.
7. Galletly, G.D. and Reynolds, T.E., "A Simple Extension of Southwell's Method for Determining the Elastic General Instability Pressure of Ring-Stiffened Cylinders Subject to External Hydrostatic Pressure," Proceedings of the Society for Experimental Stress Analysis, Los Angeles, CA, April 1955.
8. Camponeschi, Eugene T., Jr., "Compression Testing of Thick-Section Composite Materials," STP 1110, American Society of Testing Materials, Philadelphia, PA, 1991.
9. Rosen, B.W., "Mechanics of Composite Strengthening," Fiber Composite Materials, American Society for Metals, Metals Park, OH, 1964.
10. Greszczuk, L.B., "Microbuckling of Lamina Reinforced Composites," Composite Materials: Testing and Design (3<sup>rd</sup> Conference), STP 546, American Society for Testing and Materials, Philadelphia, PA, 1974.
11. Chaudhuri, Reaz A., "Prediction of the Compressive Strength of Thick-Section Advanced Composite Laminates," Journal of Composite Materials, Vol. 25, October 1991.



12. Shuart, M.J., "Short-Wavelength Buckling and Shear Failures for Compression-Loaded Composite Laminates," NASA TM-87640, NASA Langley Research Center, Hampton, VA, June 1986.
13. Irion, M.N. and Adams, D.F., "Compression Creep Testing of Unidirectional Composite Materials," Composites, Vol. 12, No. 2, April 1981.
14. Sohi, M.M., Hahn, H.T. and Williams, J.G., "The Effect of Resin Toughness and Modulus on Compression Failure Modes of Quasi-isotropic Graphite/Epoxy Laminates," STP 937, American Society for Testing and Materials, Philadelphia, PA, 1987.
15. Sinclair, J.H. and Chamis, C.C., "Compressive Behavior of Unidirectional Fibrous Composites," Compression Testing of Homogeneous Materials and Composites, STP 808, American Society for Testing and Materials, Philadelphia, PA, 1983.
16. Ross, C.T.F., Pressure Vessels Under External Pressure, Statics and Dynamics, Elsevier Science Publishers Ltd., London, 1990.
17. von Sanden, K. and Gunther, K., "The Strength of Cylindrical Shells, Stiffened by Frames and Bulkheads, Under Uniform External Pressure on All Sides," Translated by E.N. Labouvie, David Taylor Model Basin, March 1952.
18. Salerno, V.L. and Pulos, J.G., "Stress Distribution in a Circular Cylindrical Shell under Hydrostatic Pressure Supported by Equally Spaced Circular Ring Frames," Polytechnic Institute of Brooklyn, Report No. 171-A, June 1951.
19. Timoshenko, Stephen P., Theory of Elastic Stability, McGraw-Hill Book Company, Inc., New York, 1961.
20. Koiter, W., "On the stability of Elastic Equilibrium," Thesis, Delft, H.J., Paris, Amsterdam, 1945; English Translation AFFDL-TR-70-25, February 1970.
21. Kendrick, S., The Stress Analysis of Pressure Vessels and Pressure Vessel Components, Pergamon Press, 1970.
22. Jones, R.M., "Buckling of Circular Cylindrical Shells with Multiple Orthotropic Layers and Eccentric Stiffeners," AIAA Journal, Vol. 6, No. 12, December 1968.



## APPENDIX A

### CIRCUMFERENTIAL AND AXIAL STRAINS



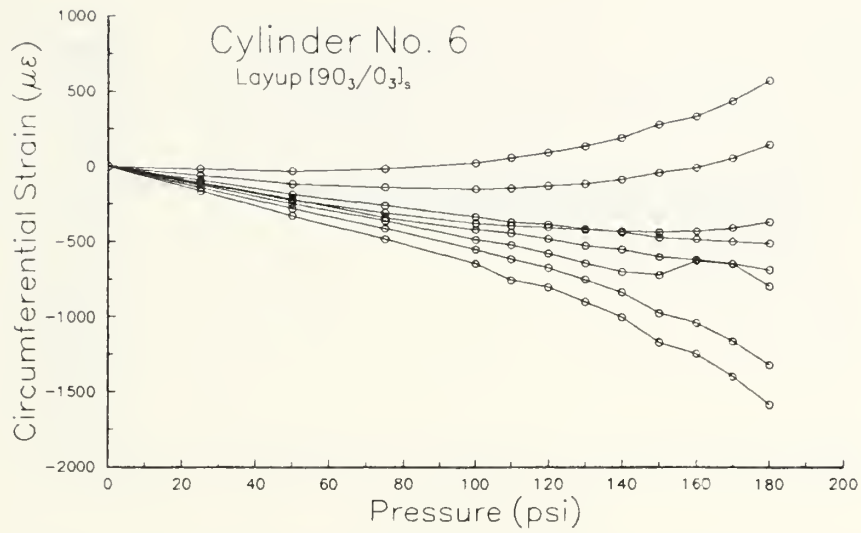


**Figure A.1.** Circumferential Strains around the centerline of cylinder 6.

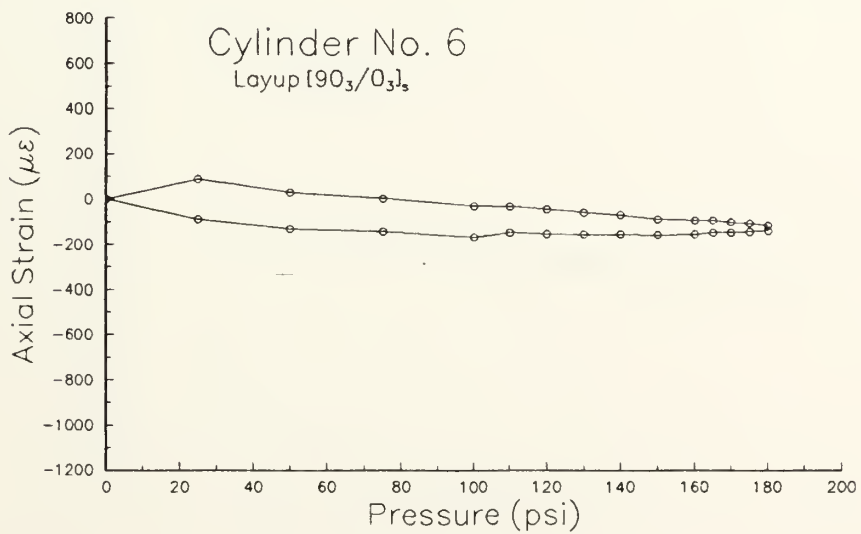


**Figure A.2.** Axial Strains at the center of cylinder 6.



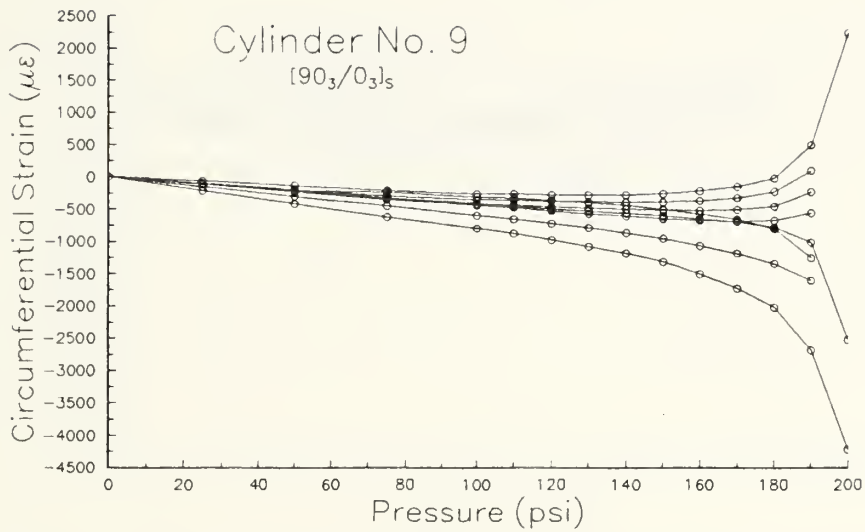


**Figure A.3.** Circumferential Strains around the centerline of cylinder 9.

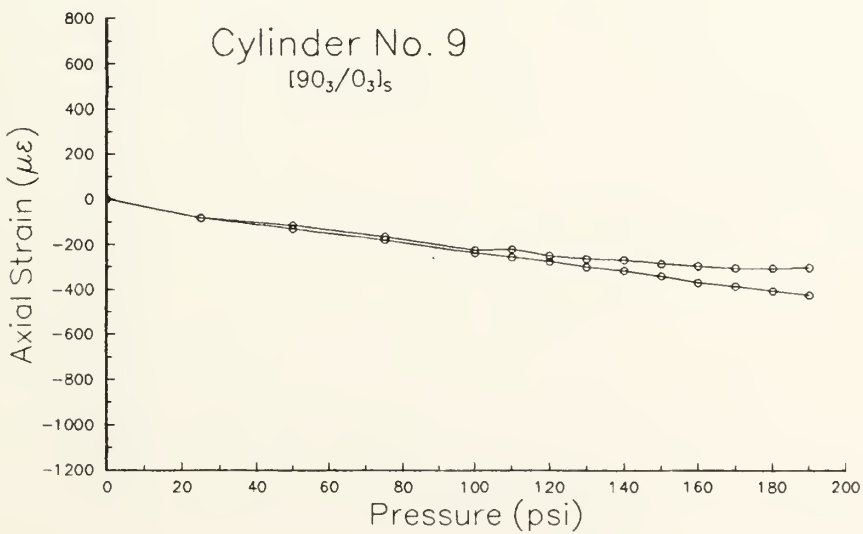


**Figure A.4.** Axial Strains at the center of cylinder 9.



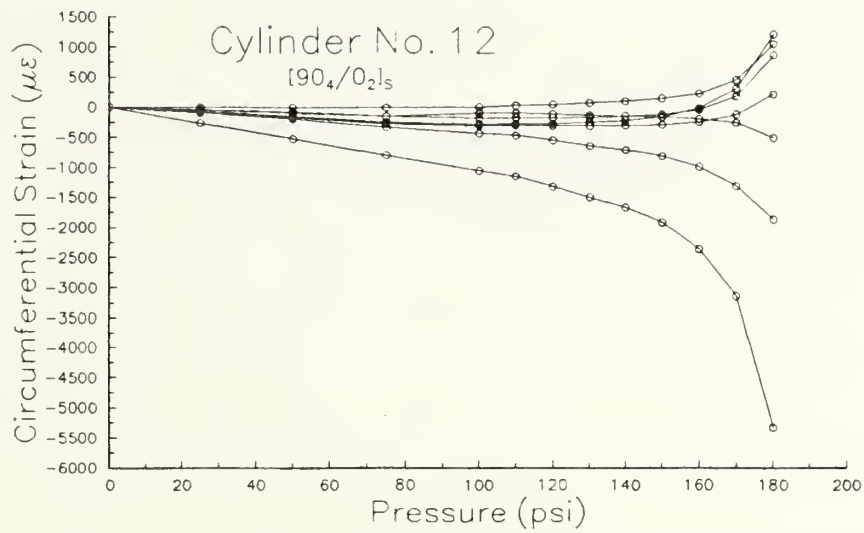


Figure A.5. Circumferential Strains around the centerline of cylinder 12.

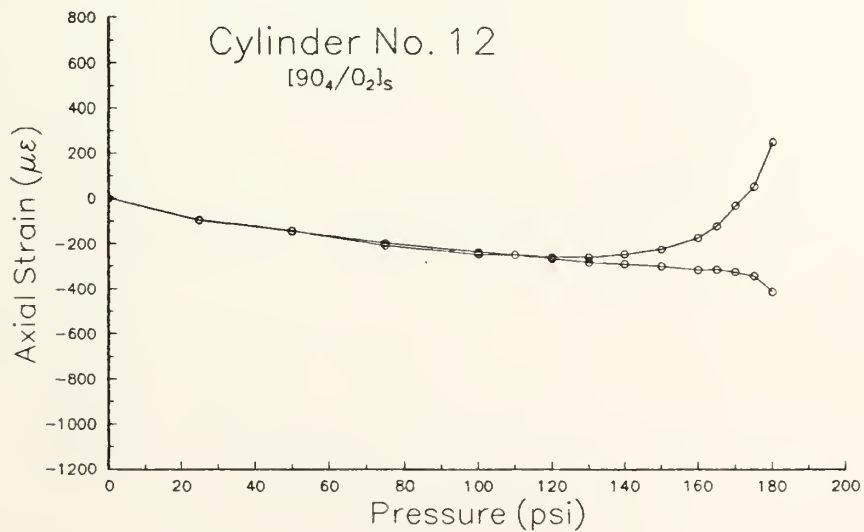
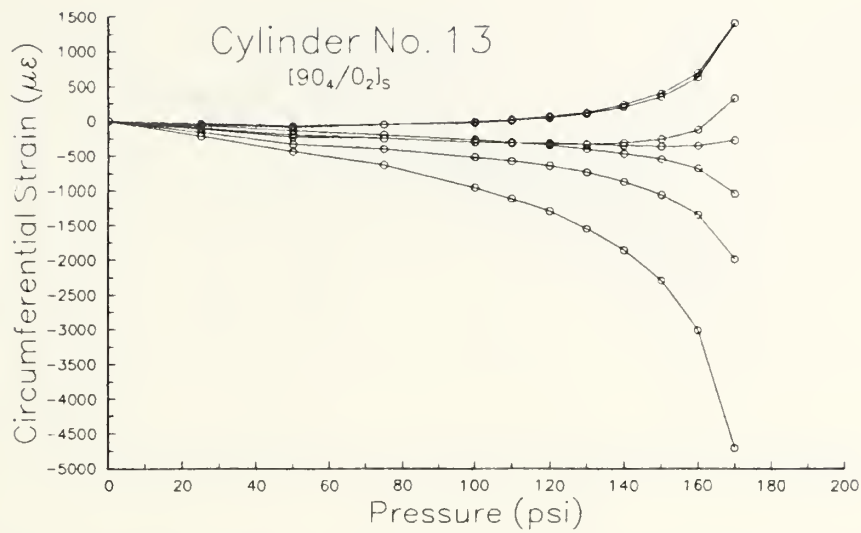
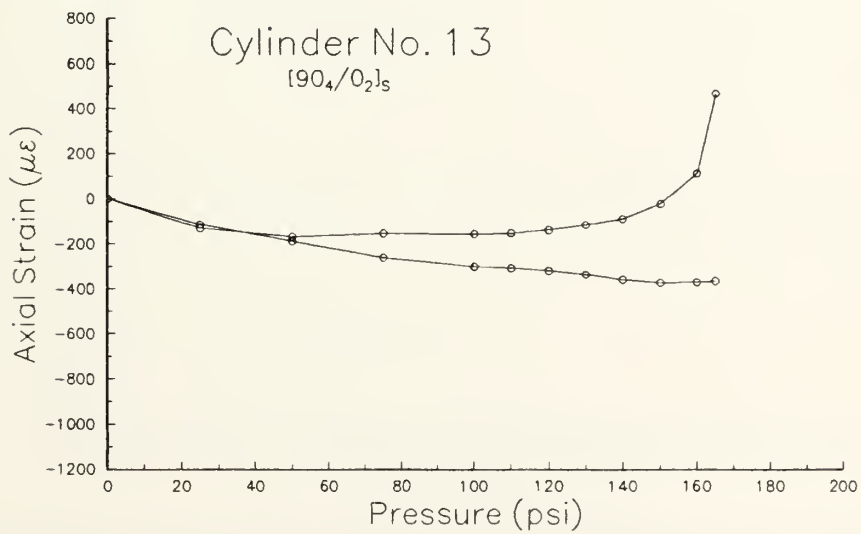


Figure A.6. Axial Strains at the center of cylinder 12.





**Figure A.7.** Circumferential Strains around the centerline of cylinder 13.



**Figure A.8.** Axial Strains at the center of cylinder 13.



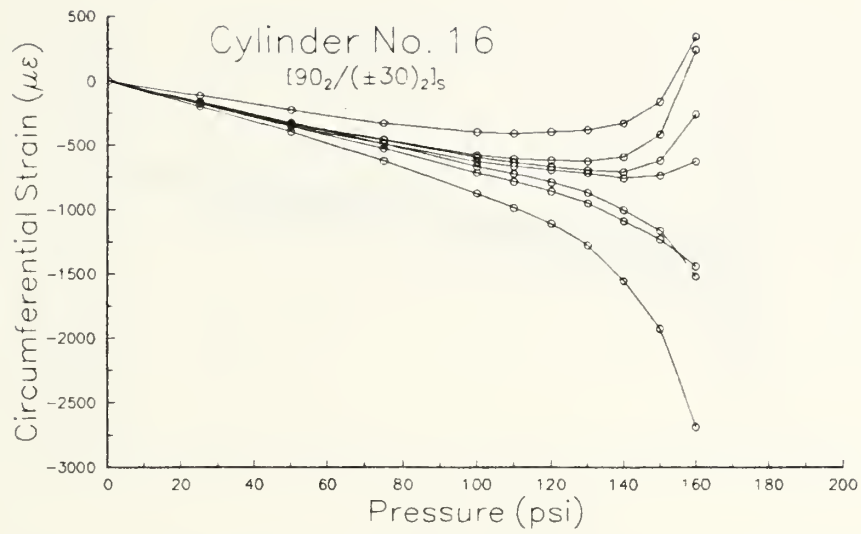


**Figure A.9.** Circumferential Strains around the centerline of cylinder 16.

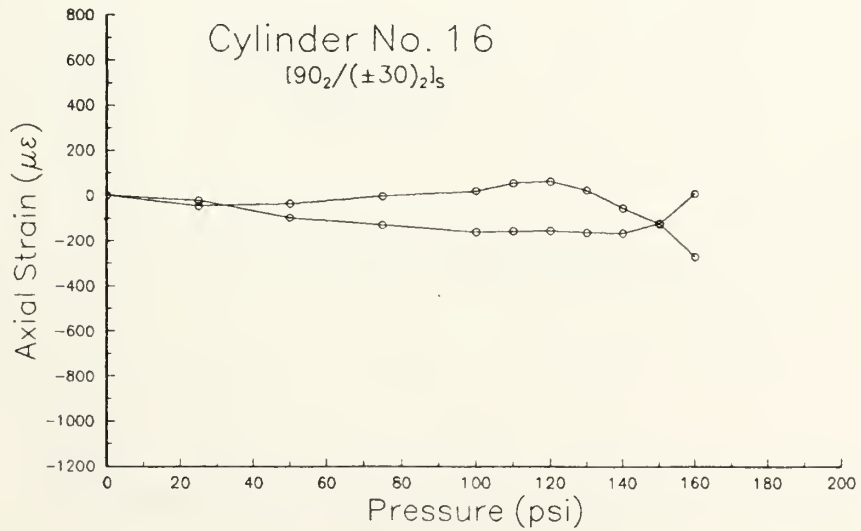


**Figure A.10.** Axial Strains at the centerline of cylinder 16.



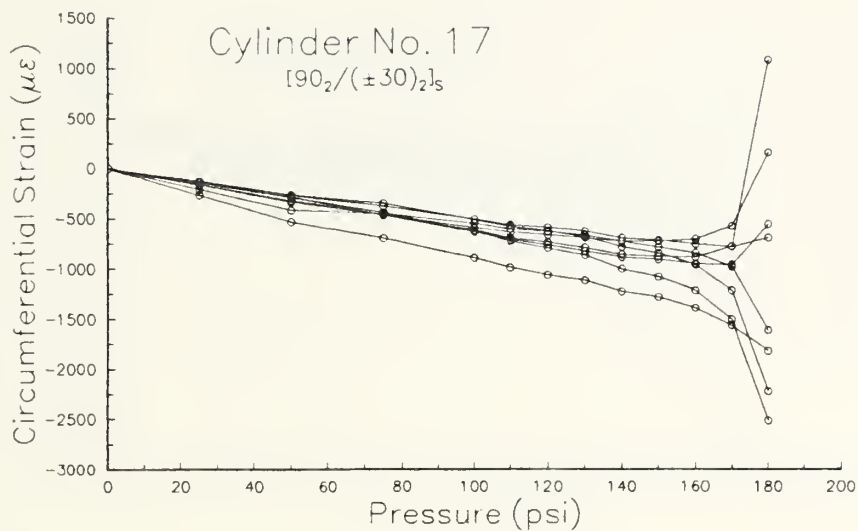


Figure A.11. Circumferential Strains around the centerline of cylinder 17.

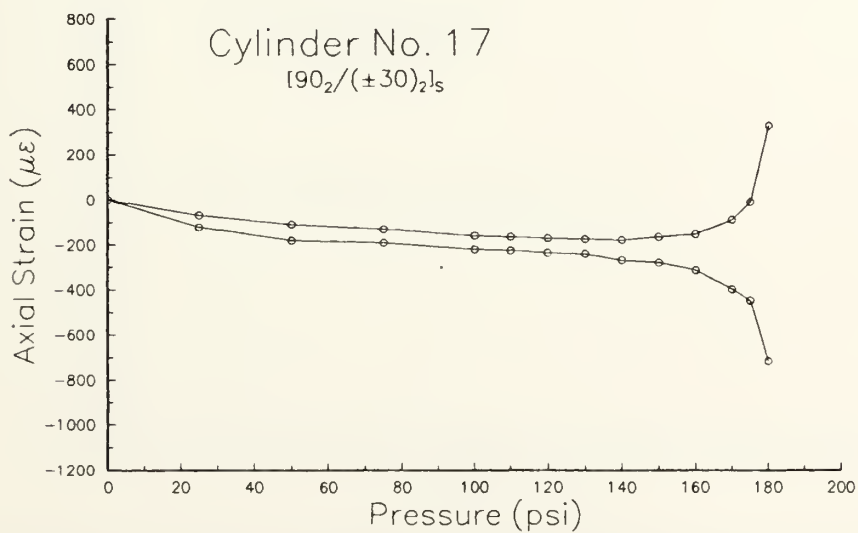
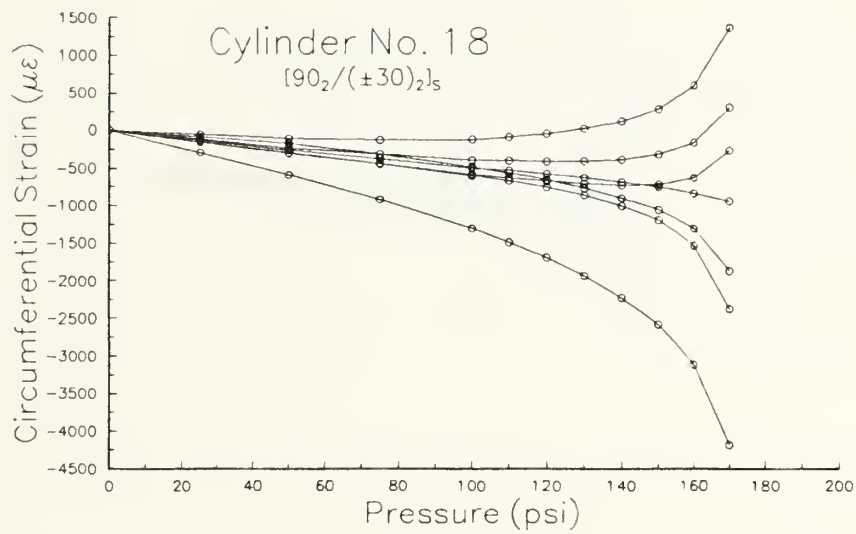
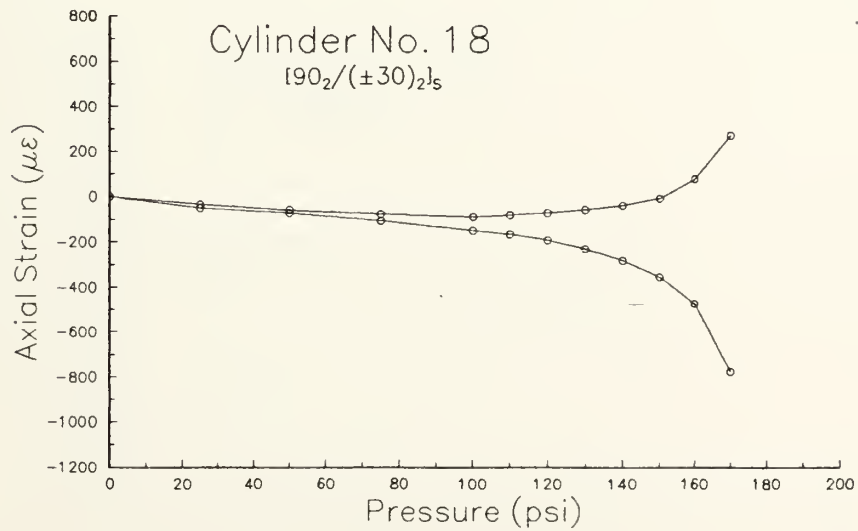


Figure A.12. Axial Strains at the center of cylinder 17.





**Figure A.13.** Circumferential Strains around the centerline of cylinder 18.



**Figure A.14.** Axial Strains at the centerline of cylinder 18.



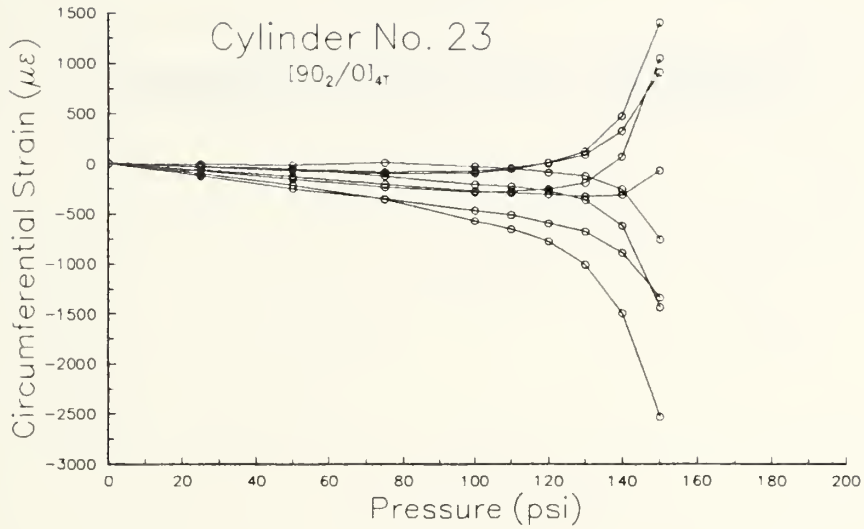


**Figure A.15.** Circumferential Strains around the centerline of cylinder 23.

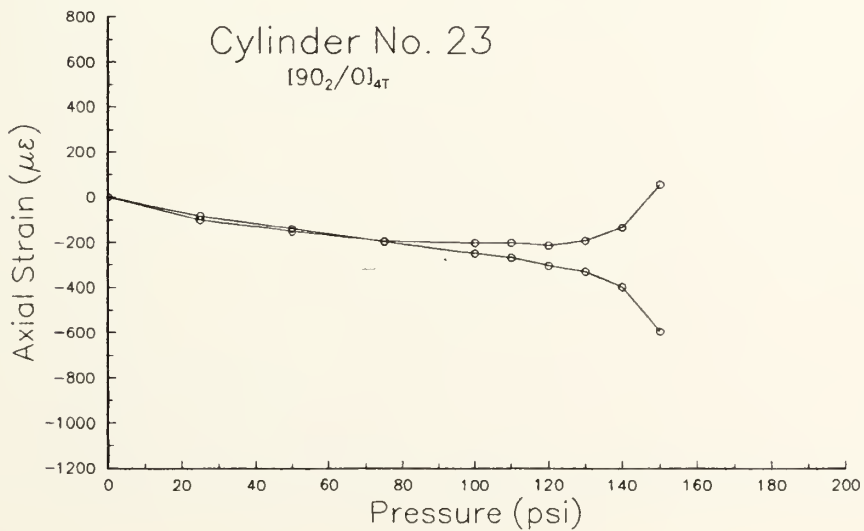


**Figure A.16.** Axial Strains at the center of cylinder 23.



## APPENDIX B

### SOUTHWELL-TYPE ANALYSIS OF STRAINS



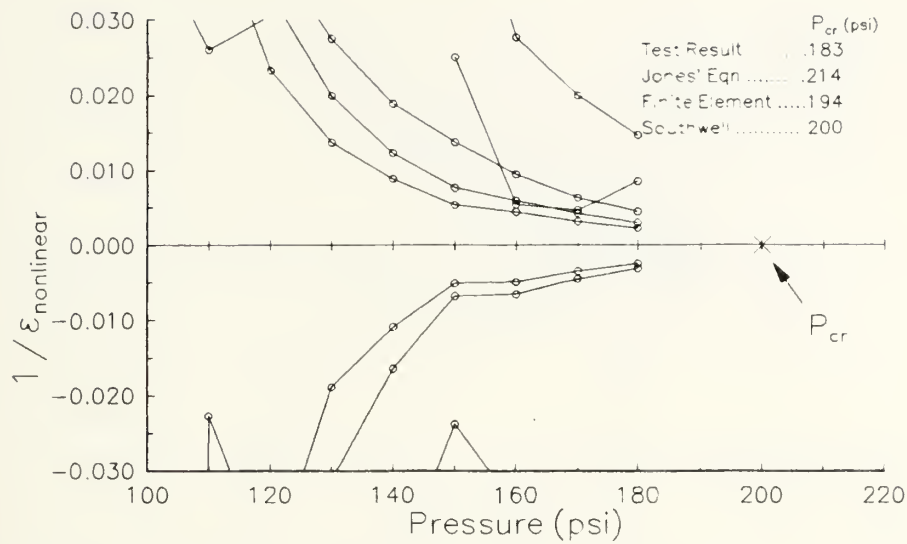


**Figure B.1.** Southwell Plot for Cylinder 6.

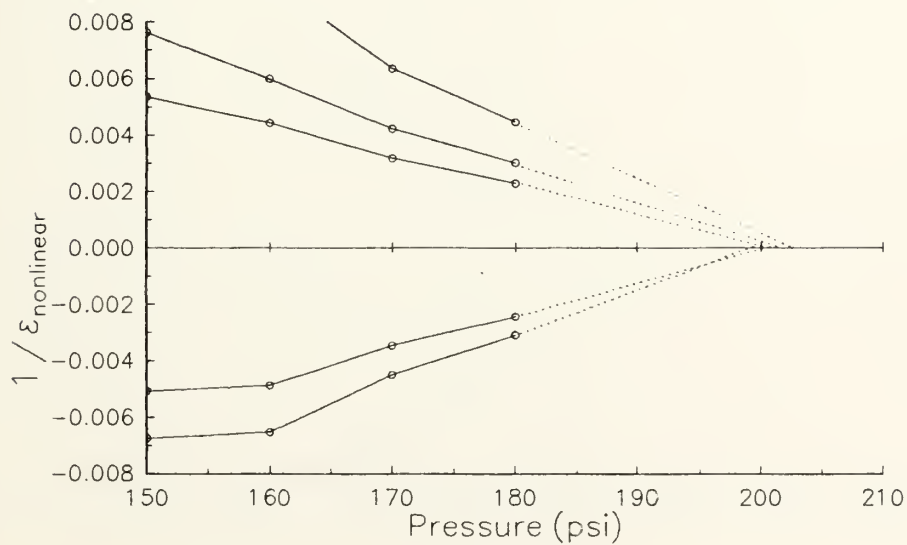


**Figure B.2.** Detail of Southwell Analysis for Cylinder 6.



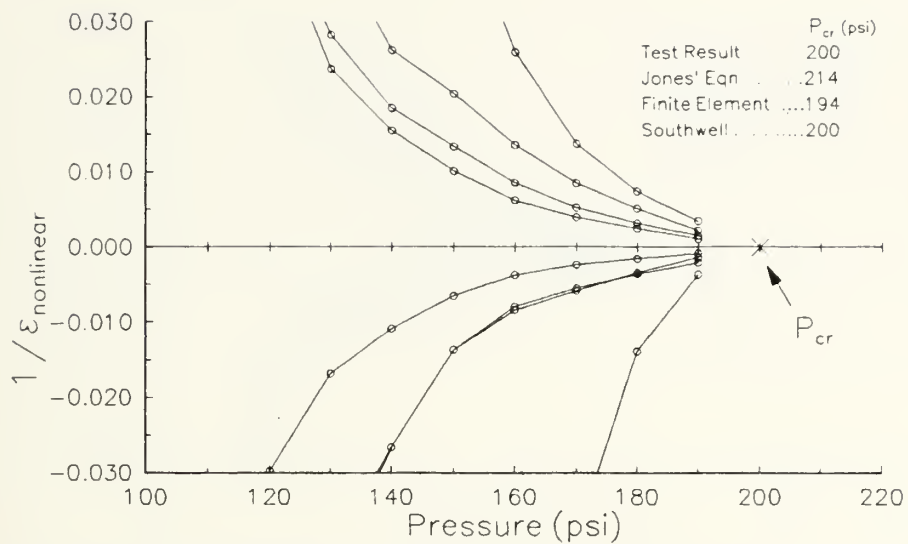


**Figure B.3.** Southwell Plot for Cylinder 9.

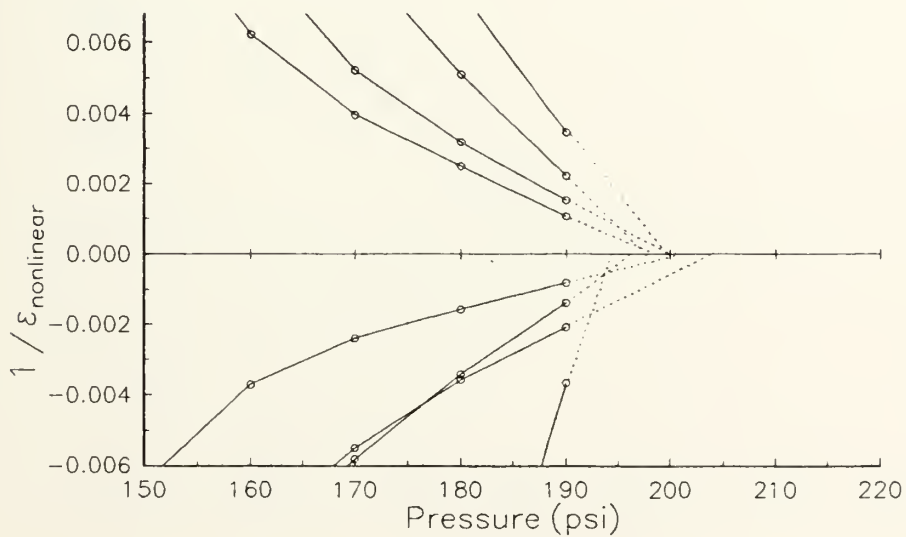


**Figure B.4.** Detail of Southwell Analysis for Cylinder 9.



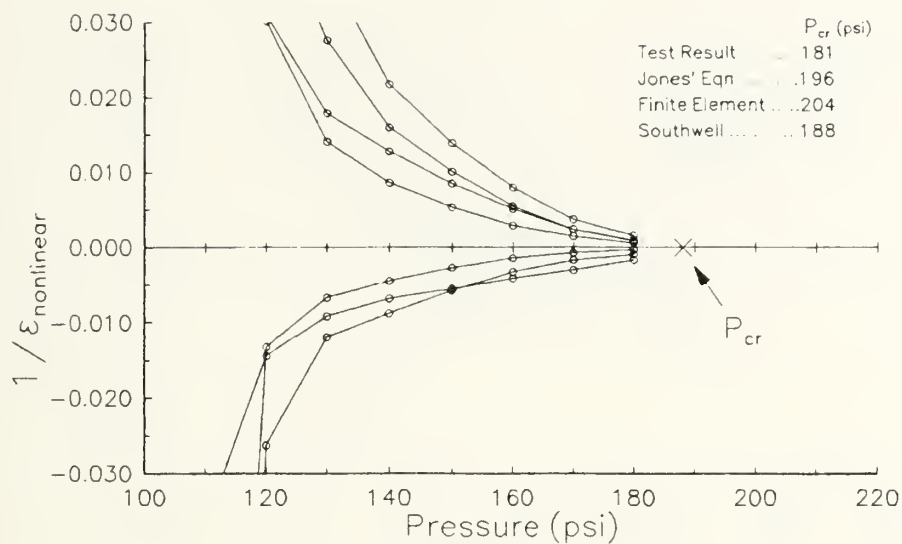


**Figure B.5. Southwell Plot for Cylinder 12.**

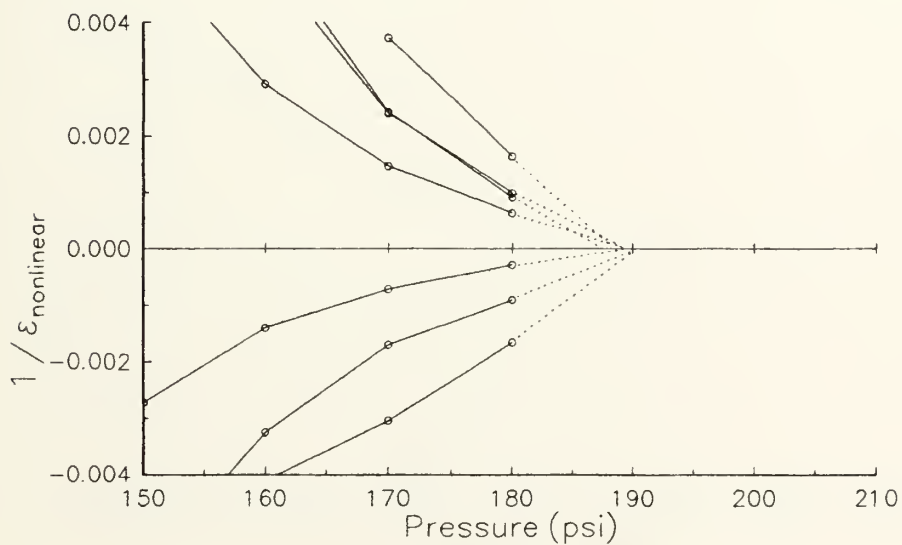


**Figure B.6. Detail of Southwell Analysis for Cylinder 12.**



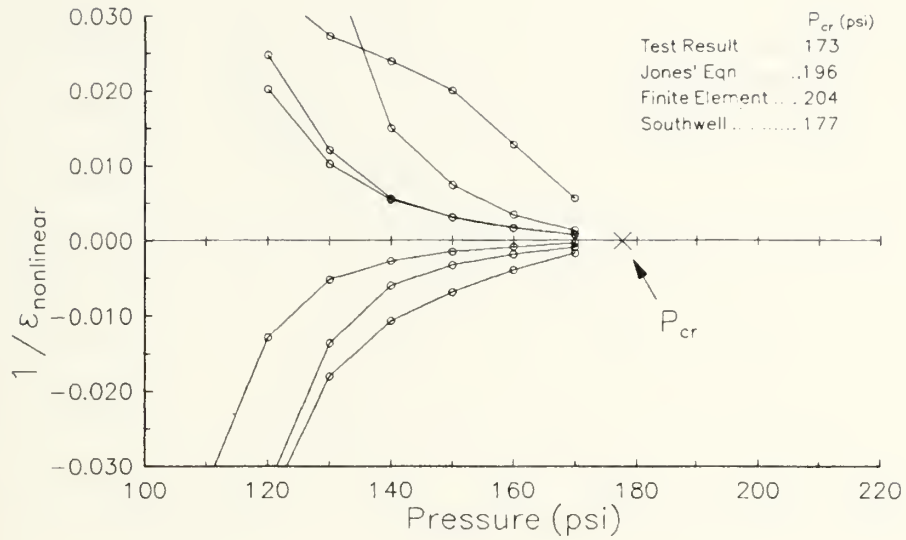


**Figure B.7.** Southwell Plot for Cylinder 13.

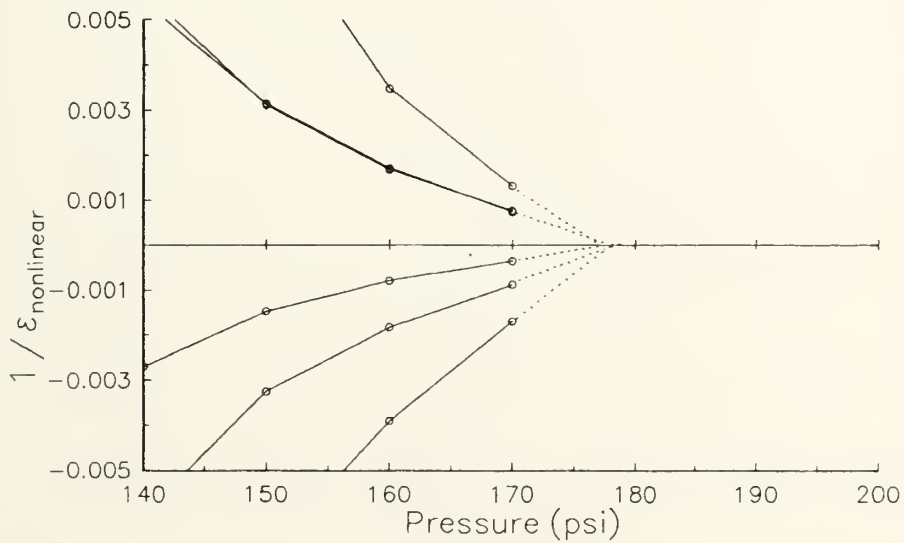


**Figure B.8.** Detail of Southwell Analysis for Cylinder 13.



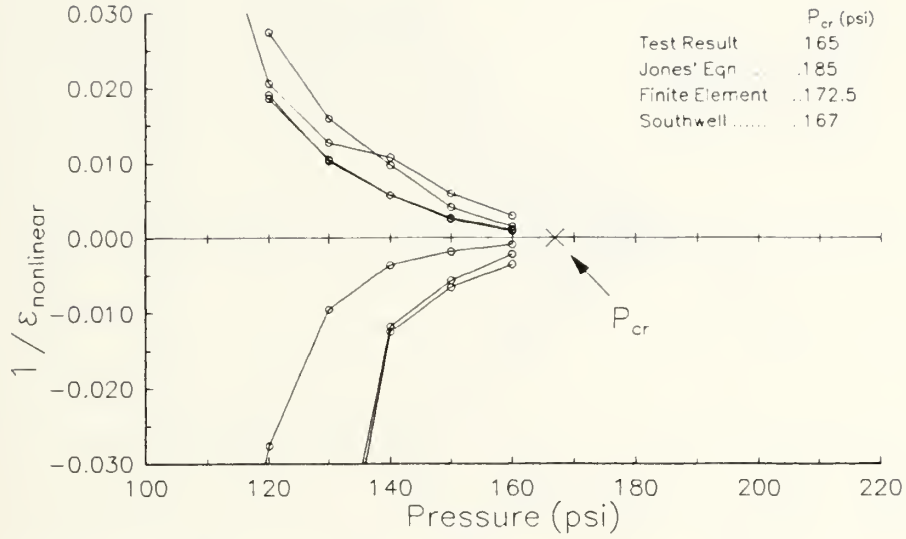


**Figure B.9.** Southwell Plot for Cylinder 16.

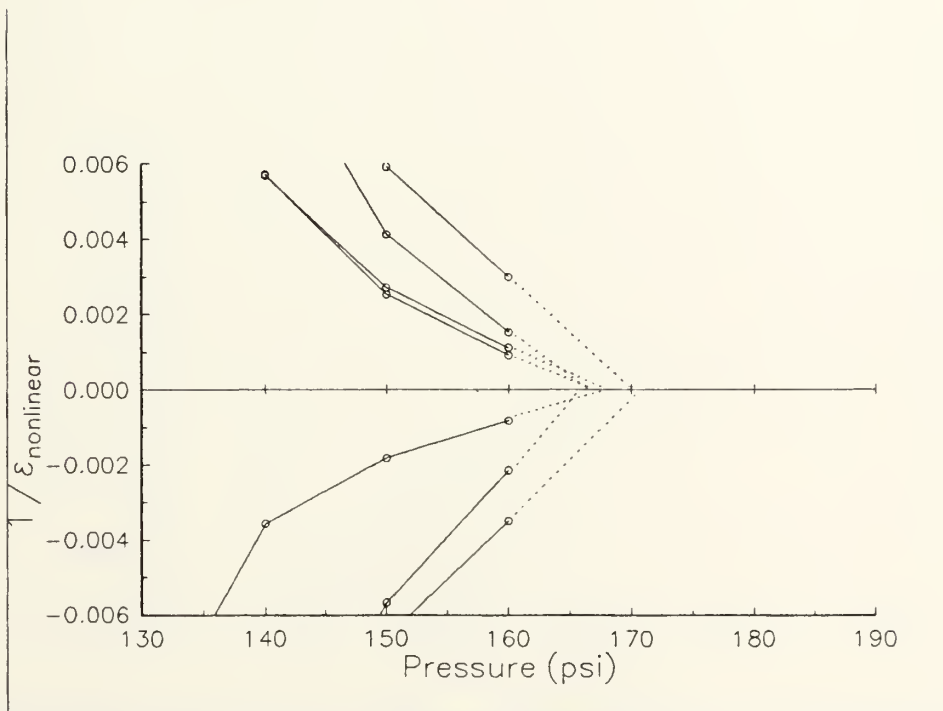


**Figure B.10.** Detail of Southwell Analysis for Cylinder 16.



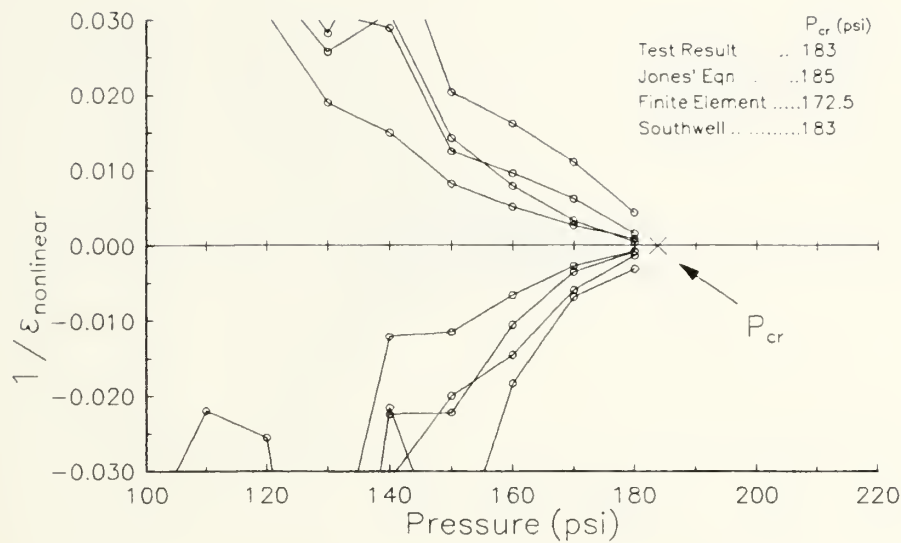


**Figure B.11.** Southwell Plot for Cylinder 17.

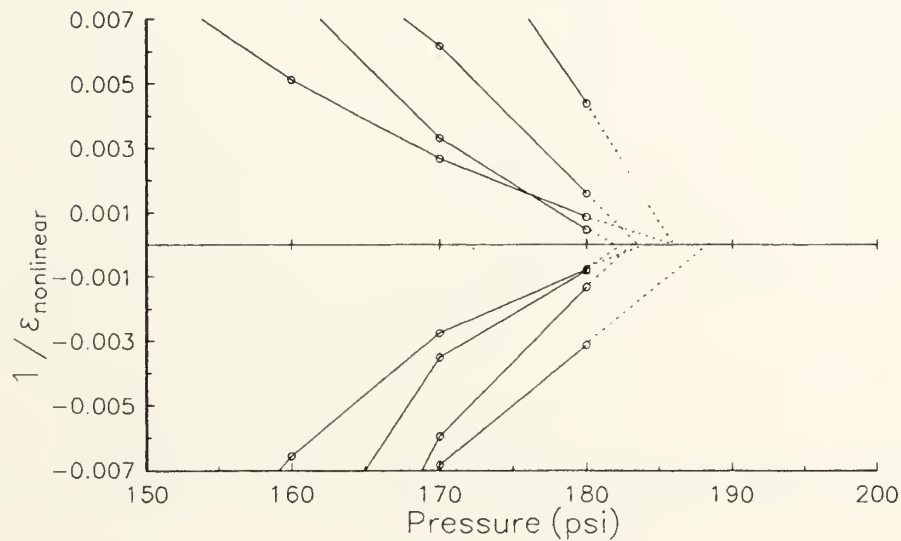


**Figure B.12.** Detail of Southwell Analysis for Cylinder 17.



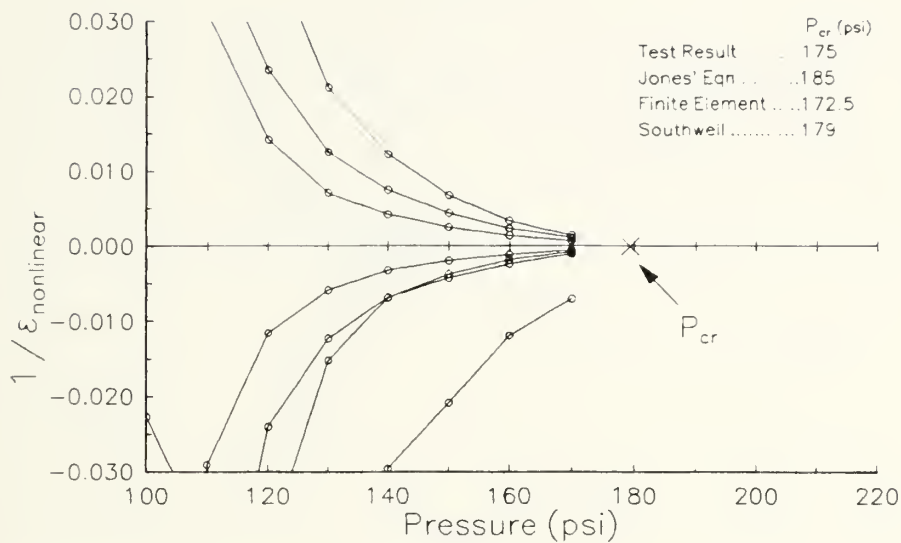


**Figure B.13.** Southwell Plot for Cylinder 18.

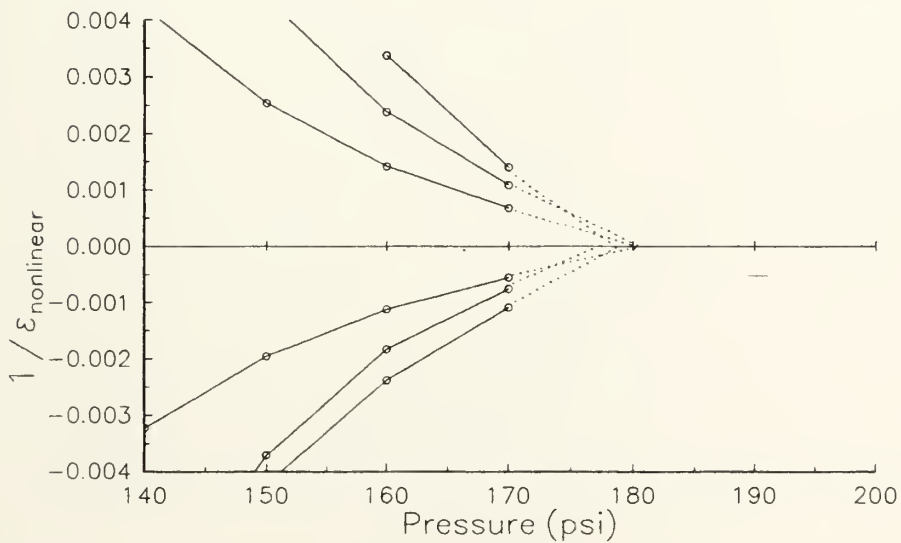


**Figure B.14.** Detail of Southwell Analysis for Cylinder 18.



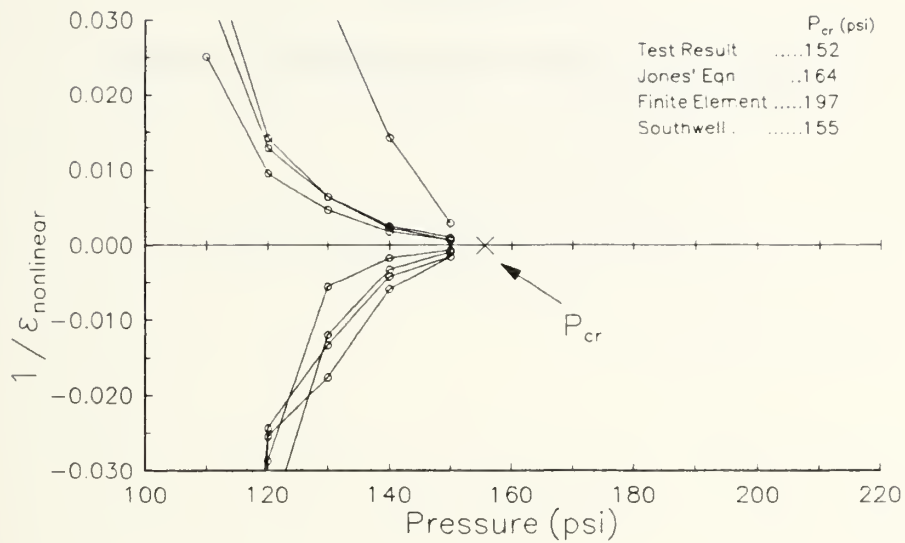


**Figure B.15. Southwell Plot for Cylinder 23.**

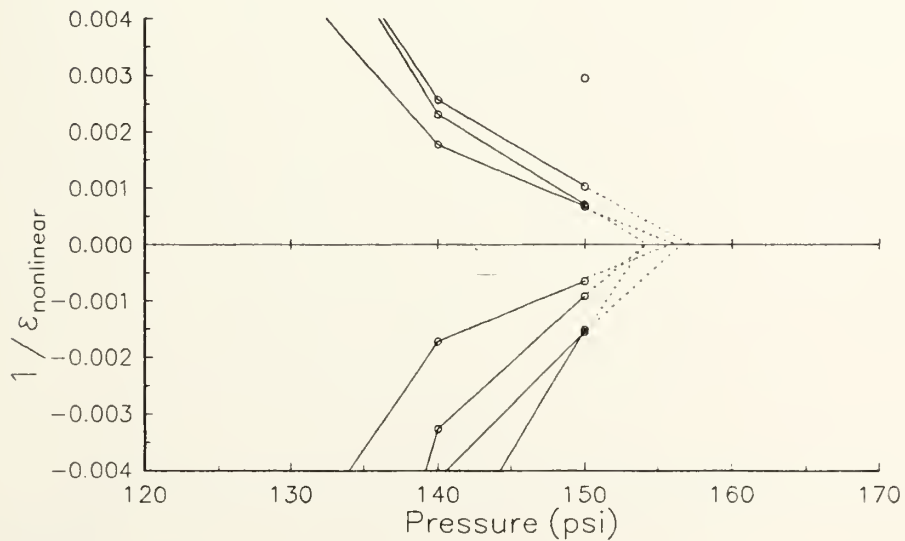


**Figure B.16. Detail of Southwell Analysis for Cylinder 23.**



## APPENDIX C

### BENDING STRAINS AND MODE SHAPE PLOTS



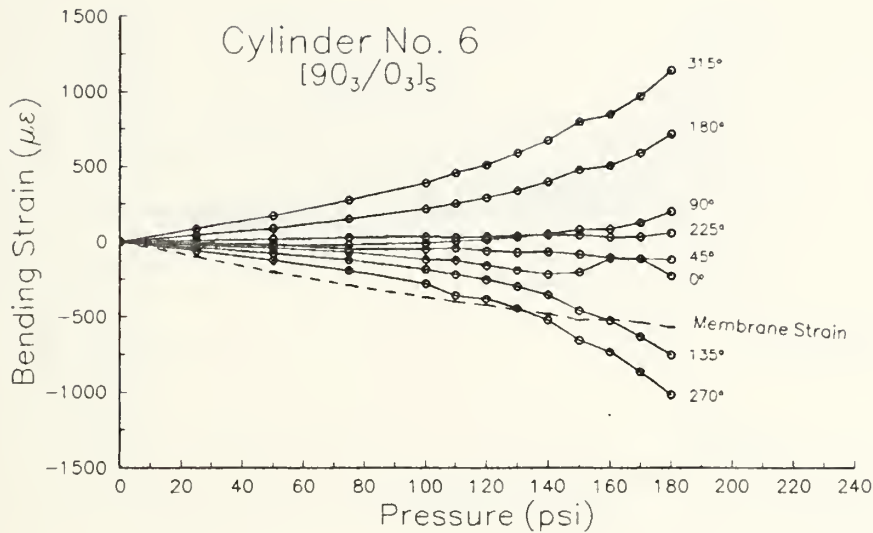
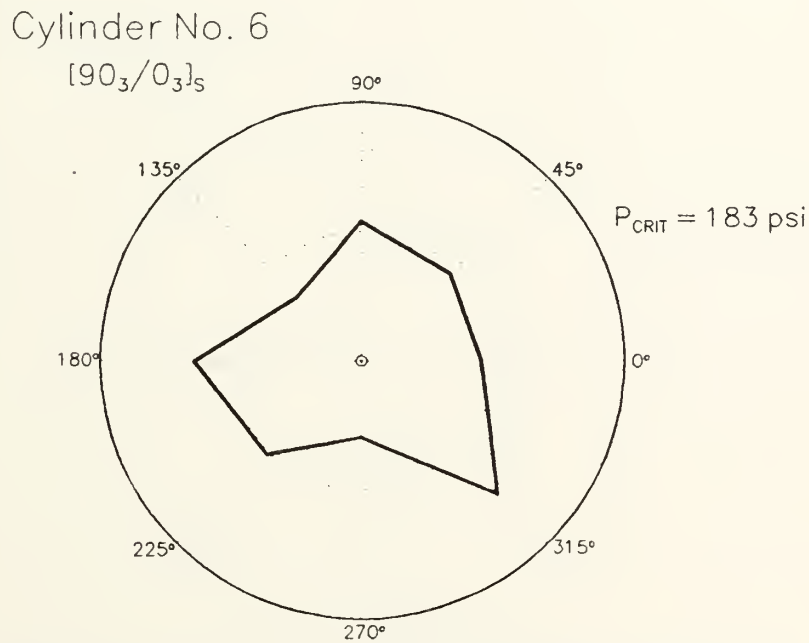


**Figure C.1..** Variation of bending strain with pressure at the noted locations around the centerline of cylinder 6.



\*Radial deflections shown at 180 psi, magnified 400 times.

**Figure C.2..** Shape variation due to bending strain for Cylinder 6.



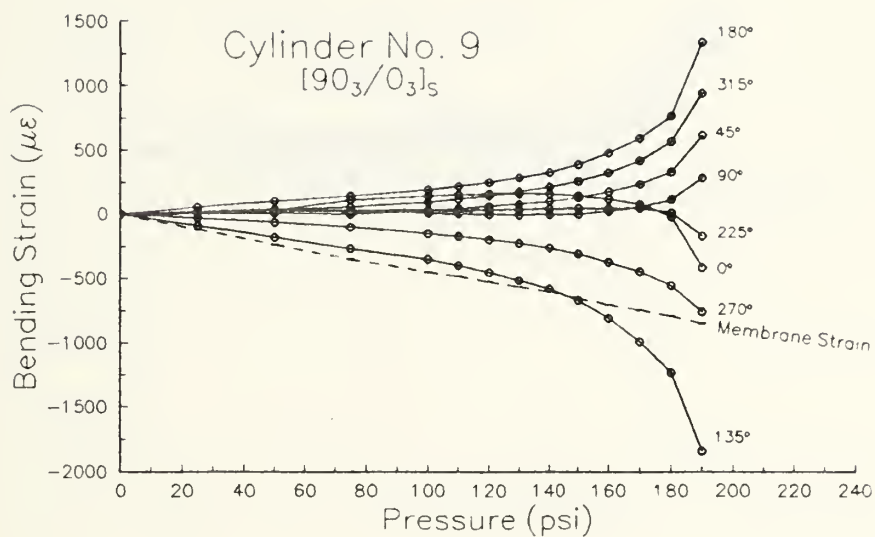
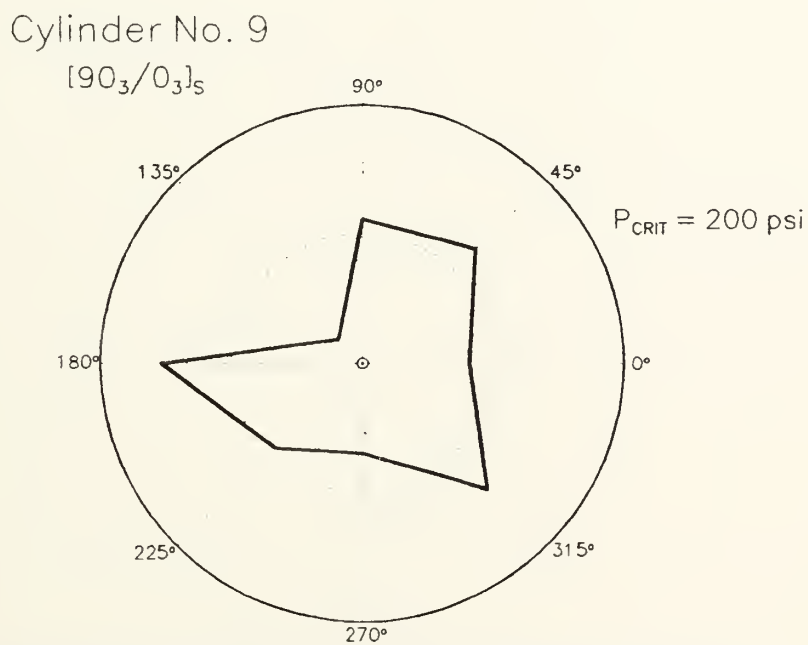


**Figure C.3.. Variation of bending strain with pressure at the noted locations around the centerline of cylinder 9.**



\*Radial deflections shown at 190 psi, magnified 400 times.

**Figure C.4.. Shape variation due to bending strain for Cylinder 9.**



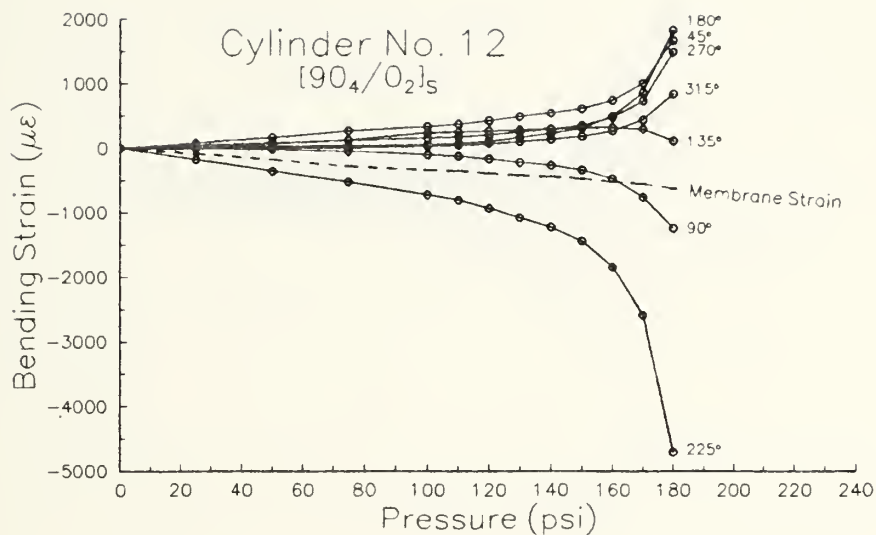
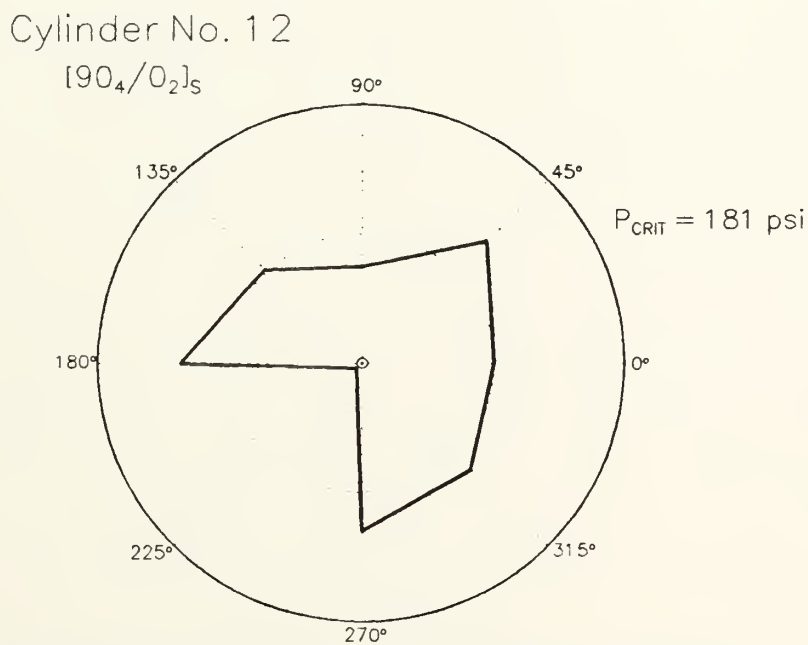


**Figure C.5.. Variation of bending strain with pressure at the noted locations around the centerline of cylinder 12.**



\*Radial deflections shown at 180 psi, magnified 200 times.

**Figure C.6.. Shape variation due to bending strain for Cylinder 12.**



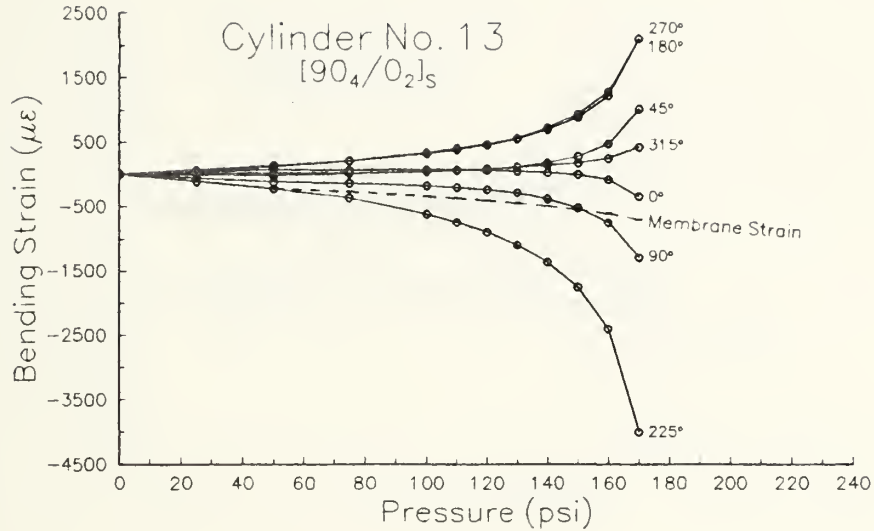
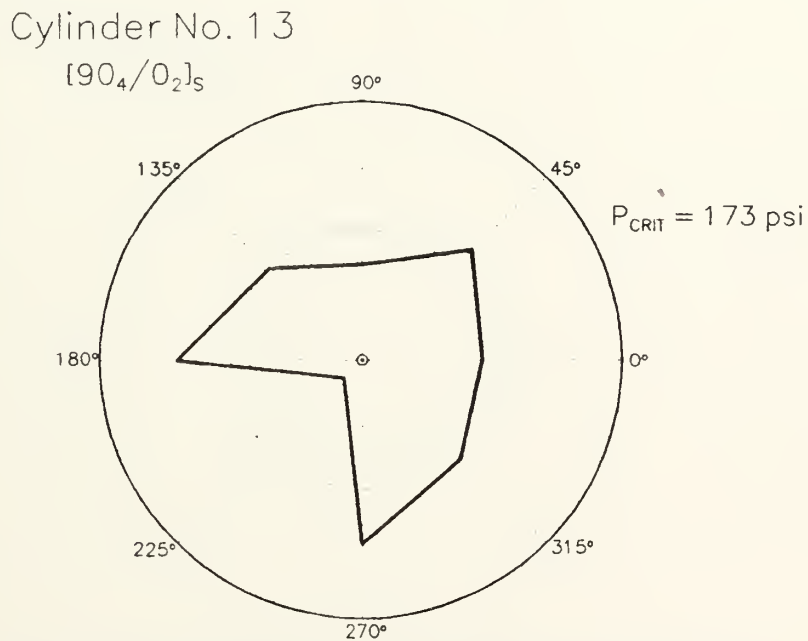


**Figure C.7..** Variation of bending strain with pressure at the noted locations around the centerline of cylinder 13.



\*Radial deflections shown at 170 psi, magnified 200 times.

**Figure C.8..** Shape variation due to bending strain for Cylinder 13.



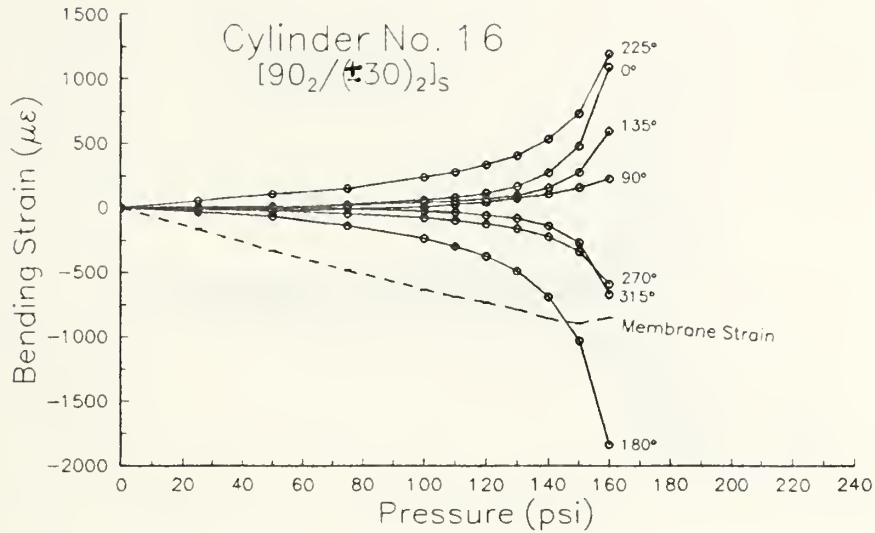
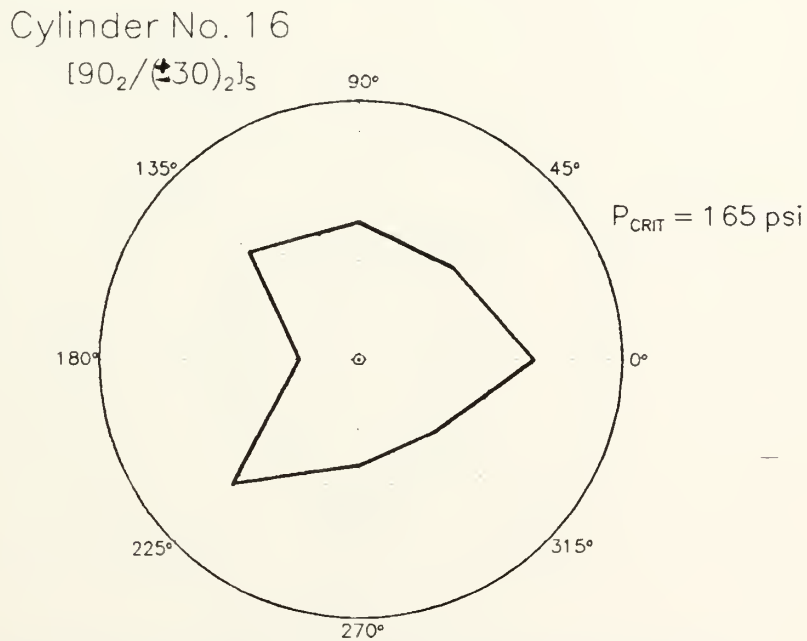


**Figure C.9..** Variation of bending strain with pressure at the noted locations around the centerline of cylinder 16.



\*Radial deflections shown at 160 psi, magnified 300 times.

**Figure C.10..** Shape variation due to bending strain for Cylinder 16.



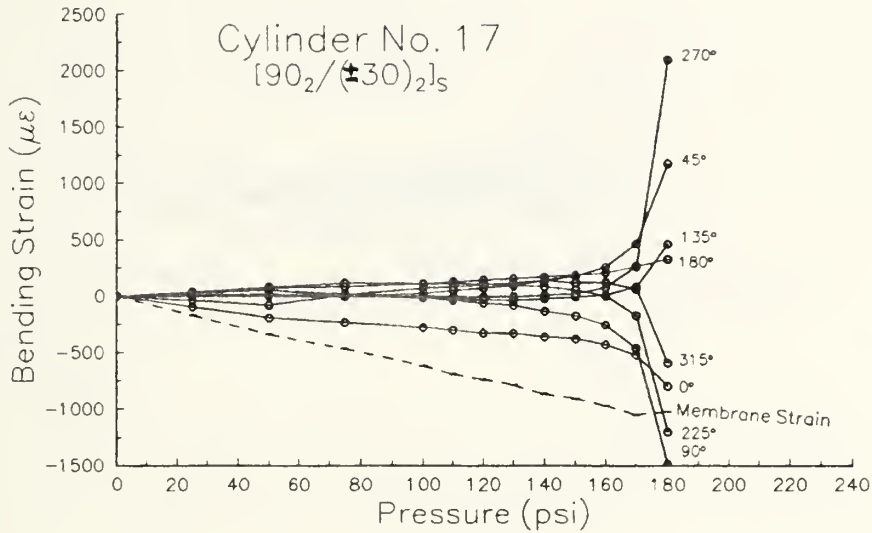
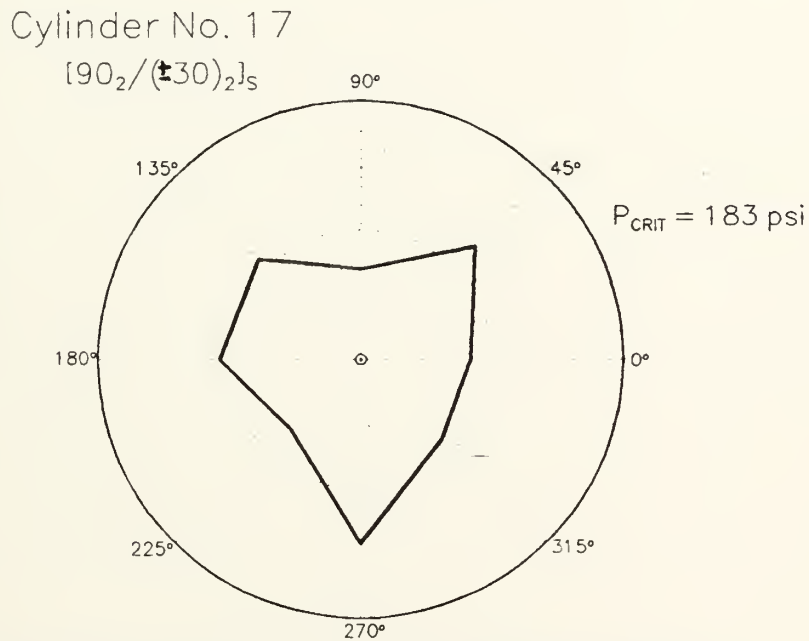


**Figure C.11..** Variation of bending strain with pressure at the noted locations around the centerline of cylinder 17.



\*Radial deflections shown at 180 psi, magnified 200 times.

**Figure C.12..** Shape variation due to bending strain for Cylinder 17.



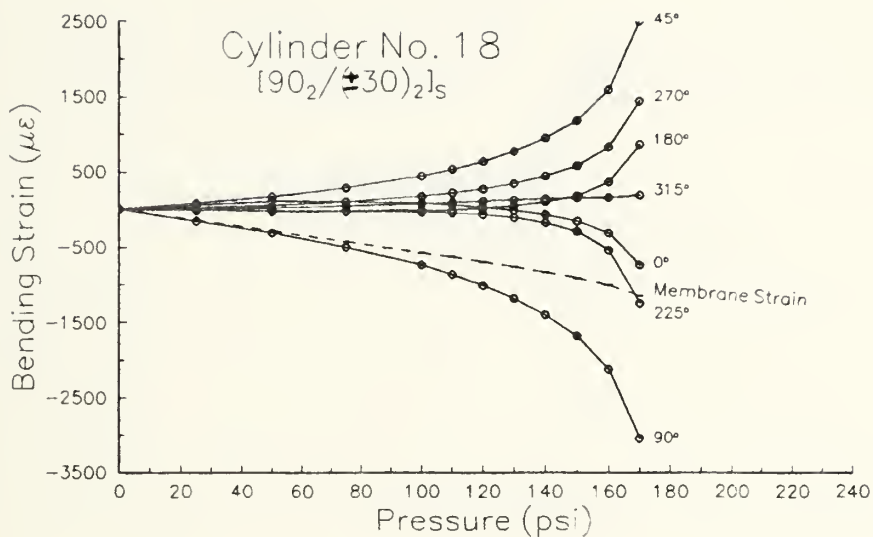
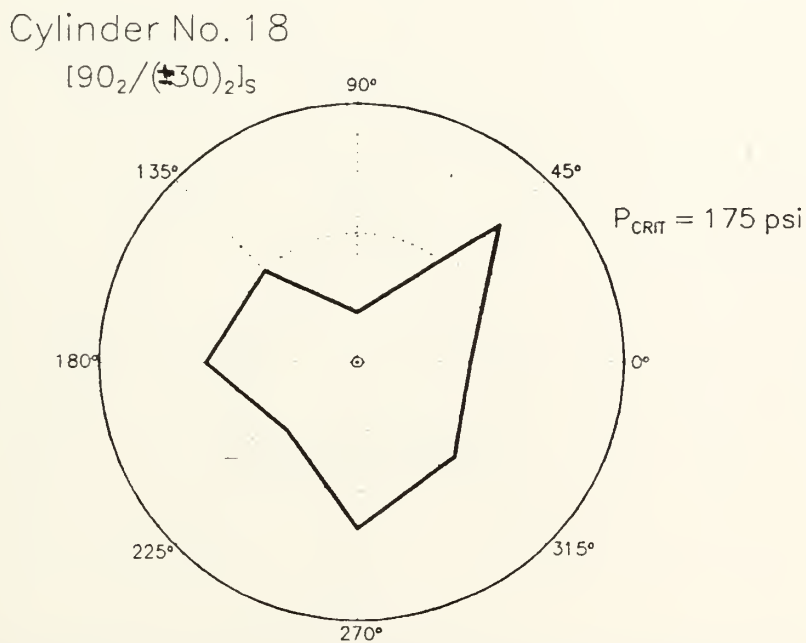


**Figure C.13..** Variation of bending strain with pressure at the noted locations around the centerline of cylinder 18.



\*Radial deflections shown at 170 psi, magnified 200 times.

**Figure C.14..** Shape variation due to bending strain for Cylinder 18.



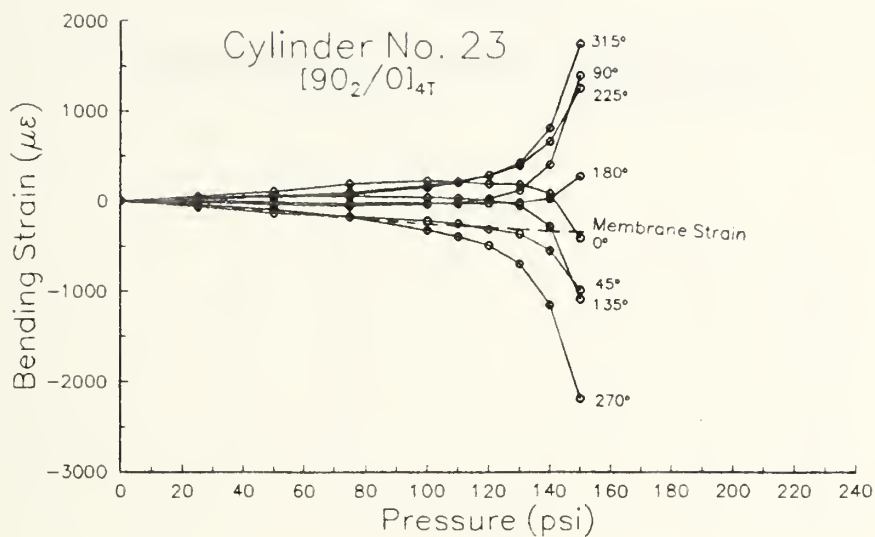
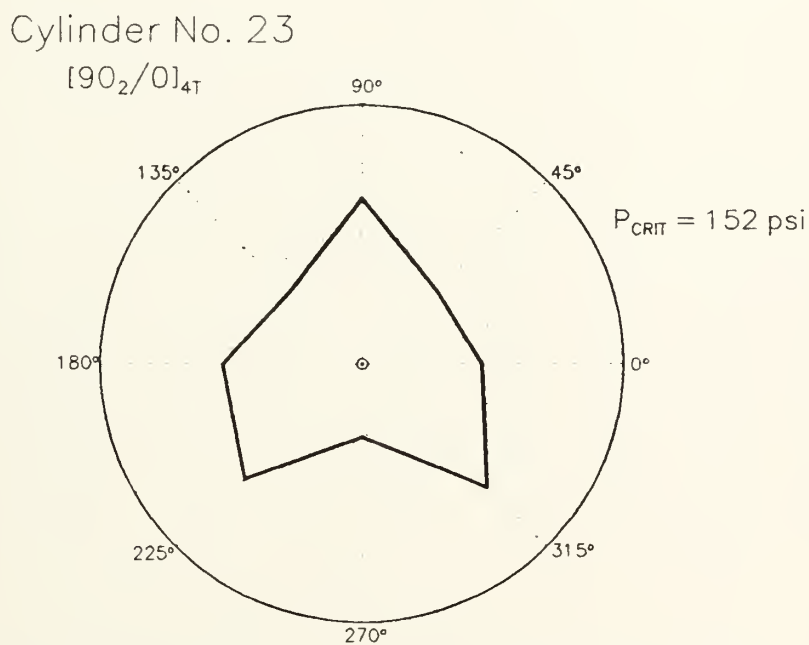


**Figure C.15.. Variation of bending strain with pressure at the noted locations around the centerline of cylinder 23.**



\*Radial deflections shown at 150 psi, magnified 200 times.

**Figure C.16.. Shape variation due to bending strain for Cylinder 23.**



## APPENDIX D

### SPREADSHEETS OF STRAIN GAGE READINGS



## STRAIN GAGE DATA FROM COMPOSITE CYLINDER HYDROSTATIC TEST.

cylinder #	layup	test date
6	[903/03]s	2/19/92

## 1. Raw Circumferential Strain Gage Data.

Pres	A*	B*	C	D	E	F	G	H	J	K
0	8	-2	3	-8	2	6	3	-11	1	9
25	-80	86	-174	-131	-145	-155	-88	-144	-189	-68
50	-124	29	-297	-239	-257	-295	-145	-236	-352	-82
75	-136	0	-413	-367	-343	-428	-170	-314	-510	-68
100	-160	-33	-539	-445	-410	-568	-181	-387	-675	-33
110	-141	-35	-575	-468	-427	-634	-177	-422	-784	2
120	-147	-47	-631	-505	-439	-690	-161	-438	-829	37
130	-148	-61	-695	-550	-455	-767	-145	-466	-925	81
140	-148	-71	-753	-576	-465	-852	-118	-490	-1030	135
150	-151	-91	-775	-627	-472	-995	-73	-527	-1201	223
160	-149	-96	-680	-645	-466	-1056	-41	-538	-1275	276
165	-141	-95	-668	-652	-452	-1104	-14	-542	-1336	321
170	-141	-105	-701	-672	-441	-1181	24	-553	-1425	380
175	-137	-110	-755	-687	-427	-1243	70	-557	-1521	448
180	-132	-118	-849	-711	-401	-1338	115	-564	-1613	517
183									-1730	

## 2. Intercept at P=0 using values at 25 and 50 psi.

	A*	B*	C	D	E	F	G	H	J	K
INT	-36	143	-51	-23	-33	-15	-31	-52	-26	-54

## 3. Zeroed Circumferential Strain Data (using intercept).

Pres	A*	B*	C	D	E	F	G	H	J	K
0	0	0	0	0	0	0	0	0	0	0
25	-44	-57	-123	-108	-112	-140	-57	-92	-163	-14
50	-88	-114	-246	-216	-224	-280	-114	-184	-326	-28
75	-100	-143	-362	-344	-310	-413	-139	-262	-484	-14
100	-124	-176	-488	-422	-377	-553	-150	-335	-649	21
110	-105	-178	-524	-445	-394	-619	-146	-370	-758	56
120	-111	-190	-580	-482	-406	-675	-130	-386	-803	91
130	-112	-204	-644	-527	-422	-752	-114	-414	-899	135
140	-112	-214	-702	-553	-432	-837	-87	-438	-1004	189
150	-115	-234	-724	-604	-439	-980	-42	-475	-1175	277
160	-113	-239	-629	-622	-433	-1041	-10	-486	-1249	330
165	-105	-238	-617	-629	-419	-1089	17	-490	-1310	375
170	-105	-248	-650	-649	-408	-1166	55	-501	-1399	434
175	-101	-253	-704	-664	-394	-1228	101	-505	-1495	502
180	-96	-261	-798	-688	-368	-1323	146	-512	-1587	571
183									-1704	



# STRAIN GAGE DATA FROM COMPOSITE CYLINDER HYDROSTATIC TEST.

cylinder # 9                      layup [903/03]s                      test date 10/31/91

## 1. Raw Circumferential Strain Gage Data.

Pres	A*	B*	C	D	E	F	G	H	J	K
0	-22	-17	-18	3	1	-15	-23	-18	-21	3
25	-104	-98	-312	-145	-184	-263	-147	-156	-194	-130
50	-137	-149	-416	-259	-284	-472	-213	-260	-343	-232
75	-189	-197	-444	-382	-412	-673	-288	-376	-496	-324
100	-247	-256	-513	-454	-526	-856	-339	-471	-645	-381
110	-245	-275	-535	-470	-562	-936	-344	-506	-699	-390
120	-274	-293	-574	-496	-613	-1035	-358	-547	-769	-406
130	-286	-316	-610	-517	-656	-1134	-359	-583	-836	-415
140	-291	-333	-651	-532	-689	-1240	-357	-616	-911	-419
150	-308	-358	-714	-550	-734	-1375	-343	-659	-1006	-421
160	-318	-387	-788	-554	-762	-1564	-302	-708	-1119	-402
170	-327	-403	-868	-538	-773	-1786	-230	-748	-1234	-350
180	-328	-422	-1017	-489	-757	-2077	-104	-832	-1392	-251
190	-325	-443	-1472	-265	-649	-2743	408	-1071	-1653	65
200						-4279	2152	-2583		

## 2. Intercept at P=0 using values at 25 and 50 psi.

	A*	B*	C	D	E	F	G	H	J	K
INT	-71	-47	-208	-31	-84	-54	-81	-52	-45	-28

## 3. Zeroed Circumferential Strain Data (using intercept).

Pres	A*	B*	C	D	E	F	G	H	J	K
0	0	0	0	0	0	0	0	0	0	0
25	-33	-51	-104	-114	-100	-209	-66	-104	-149	-102
50	-66	-102	-208	-228	-200	-418	-132	-208	-298	-204
75	-118	-150	-236	-351	-328	-619	-207	-324	-451	-296
100	-176	-209	-305	-423	-442	-802	-258	-419	-600	-353
110	-174	-228	-327	-439	-478	-882	-263	-454	-654	-362
120	-203	-246	-366	-465	-529	-981	-277	-495	-724	-378
130	-215	-269	-402	-486	-572	-1080	-278	-531	-791	-387
140	-220	-286	-443	-501	-605	-1186	-276	-564	-866	-391
150	-237	-311	-506	-519	-650	-1321	-262	-607	-961	-393
160	-247	-340	-580	-523	-678	-1510	-221	-656	-1074	-374
170	-256	-356	-660	-507	-689	-1732	-149	-696	-1189	-322
180	-257	-375	-809	-458	-673	-2023	-23	-780	-1347	-223
190	-254	-396	-1264	-234	-565	-2689	489	-1019	-1608	93
200						-4225	2233	-2531		



# STRAIN GAGE DATA FROM COMPOSITE CYLINDER HYDROSTATIC TEST.

cylinder # 12      layup [904/02]s      test date 11/15/91

## 1. Raw Circumferential Strain Gage Data.

Pres	A*	B*	C	D	E	F	G	H	J	K
0	-5	2	17178	-14	-6	1	-4	1	-2	-4
25	-104	-94	17194	-62	-115	-94	-96	-130	-71	-92
50	-151	-142	17247	-66	-211	-137	-171	-395	-120	-176
75	-203	-208	17298	-69	-354	-206	-269	-671	-181	-284
100	-244	-247	17346	-58	-459	-148	-303	-924	-202	-314
110	-257	-250	17370	-36	-497	-151	-296	-1018	-198	-314
120	-274	-260	17390	-18	-573	-170	-298	-1188	-198	-323
130	-289	-260	17414	10	-661	-187	-274	-1364	-192	-324
140	-296	-247	17434	37	-733	-202	-242	-1538	-174	-317
150	-306	-225	17453	81	-836	-214	-185	-1783	-146	-303
160	-323	-174	17474	163	-1010	-251	-42	-2229	-71	-261
165	-322	-123	17486	246	-1104	-264	66	-2475	7	-216
170	-332	-32	17500	389	-1334	-313	285	-3012	152	-131
175	-349	54	17511	543	-1522	-377	530	-3522	313	-45
180	-419	251	17521	985	-1889	-565	1182	-5200	840	202
181								-5800		

## 2. Intercept at P=0 using values at 25 and 50 psi.

	A*	B*	C	D	E	F	G	H	J	K
INT	-57	-46		-58	-19	-51	-21	135	-22	-8

## 3. Zeroed Circumferential Strain Data (using intercept).

Pres	A*	B*	C	D	E	F	G	H	J	K
0	0	0		0	0	0	0	0	0	0
25	-47	-48	b	-4	-96	-43	-75	-265	-49	-84
50	-94	-96	a	-8	-192	-86	-150	-530	-98	-168
75	-146	-162	d	-11	-335	-155	-248	-806	-159	-276
100	-187	-201		0	-440	-97	-282	-1059	-180	-306
110	-200	-204	g	22	-478	-100	-275	-1153	-176	-306
120	-217	-214	a	40	-554	-119	-277	-1323	-176	-315
130	-232	-214	g	68	-642	-136	-253	-1499	-170	-316
140	-239	-201	e	95	-714	-151	-221	-1673	-152	-309
150	-249	-179		139	-817	-163	-164	-1918	-124	-295
160	-266	-128		221	-991	-200	-21	-2364	-49	-253
165	-265	-77		304	-1085	-213	87	-2610	29	-208
170	-275	14		447	-1315	-262	306	-3147	174	-123
175	-292	100		601	-1503	-326	551	-3657	335	-37
180	-362	297		1043	-1870	-514	1203	-5335	862	210
181								-5935		



# STRAIN GAGE DATA FROM COMPOSITE CYLINDER HYDROSTATIC TEST.

cylinder # 13                      layup [904/02]s                      test date 10/17/91

## 1. Raw Circumferential Strain Gage Data.

Pres	A*	B*	C	D	E	F	G	H	J	K
0	-4	-6	1	-2	-5	-1	-6	-5	5	4
25	-120	-85	-114	-102	-122	10243	-85	-215	-69	-109
50	-192	-139	-186	-202	-289	-182	-121	-435	-116	-226
75	-267	-174	-249	-261	-366	1009	-107	-633	-80	-251
100	-306	-163	-316	-309	-483	1131	-80	-962	-38	-304
110	-314	-160	-357	-328	-542	1100	-53	-1123	-7	-313
120	-325	-146	-397	-340	-606	1133	-11	-1302	35	-318
130	-341	-123	-451	-341	-696	1133	48	-1549	94	-332
140	-364	-95	-516	-320	-836	1167	146	-1858	205	-348
150	-378	-30	-595	-271	-1024	1201	291	-2298	367	-361
160	-376	105	-732	-138	-1311	1355	568	-3010	659	-354
170	-371	459	-1093	316	-1947	1602	1348	-4699	1378	-274
173								-7500		

## 2. Intercept at P=0 using values at 25 and 50 psi.

	A*	B*	C	D	E	F	G	H	J	K
INT	-48	-31	-42	-2	45		-49	5	-22	8

## 3. Zeroed Circumferential Strain Data (using intercept).

Pres	A*	B*	C	D	E	F	G	H	J	K
0	0	0	0	0	0		0	0	0	0
25	-72	-54	-72	-100	-167	b	-36	-220	-47	-117
50	-144	-108	-144	-200	-334	a	-72	-440	-94	-234
75	-219	-143	-207	-259	-411	d	-58	-638	-58	-259
100	-258	-132	-274	-307	-528		-31	-967	-16	-312
110	-266	-129	-315	-326	-587	g	-4	-1128	15	-321
120	-277	-115	-355	-338	-651	a	38	-1307	57	-326
130	-293	-92	-409	-339	-741	g	97	-1554	116	-340
140	-316	-64	-474	-318	-881	e	195	-1863	227	-356
150	-330	1	-553	-269	-1069		340	-2303	389	-369
160	-328	136	-690	-136	-1356		617	-3015	681	-362
170	-323	490	-1051	318	-1992		1397	-4704	1400	-282
173								-7505		



# STRAIN GAGE DATA FROM COMPOSITE CYLINDER HYDROSTATIC TEST.

cylinder # 16      layup [902/(+\_30)2]s      test date 11/5/91

## 1. Raw Circumferential Strain Gage Data.

Pres	A*	F*	B	C	D	E	G	H	J	K
0	1	4	10	-15343	6	10	13	-8	-2	-7
25	-23	-43	-136	-15504	-132	-139	-186	-105	-184	-185
50	-98	-33	-303	-15574	-310	-310	-385	-218	-361	-347
75	-132	-1	-428	-15625	-445	-431	-610	-325	-536	-514
100	-161	24	-546	-15676	-583	-564	-861	-391	-721	-687
110	-158	58	-577	-15700	-618	-606	-976	-404	-794	-745
120	-156	65	-589	-15718	-646	-635	-1097	-391	-868	-815
130	-164	27	-592	-15743	-671	-662	-1267	-376	-959	-892
140	-166	-52	-561	-15779	-712	-675	-1541	-322	-1095	-1027
150	-124	-124	-387	-15825	-691	-588	-1912	-154	-1241	-1187
160	7	-269	269	-15915	-581	-227	-2674	350	-1449	-1545
165							-5200			

## 2. Intercept at P=0 using values at 25 and 50 psi.

	A*	F*	B	C	D	E	G	H	J	K
INT	52	-53	31	<del>-15434</del>	46	32	13	8	-7	-23

## 3. Zeroed Circumferential Strain Data (using intercept).

Pres	A*	F*	B	C	D	E	G	H	J	K
0	0	0	0		0	0	0	0	0	0
25	-75	10	-167	b	-178	-171	-199	-113	-177	-162
50	-150	20	-334	a	-356	-342	-398	-226	-354	-324
75	-184	52	-459	d	-491	-463	-623	-333	-529	-491
100	-213	77	-577		-629	-596	-874	-399	-714	-664
110	-210	111	-608	g	-664	-638	-989	-412	-787	-722
120	-208	118	-620	a	-692	-667	-1110	-399	-861	-792
130	-216	80	-623	g	-717	-694	-1280	-384	-952	-869
140	-218	1	-592	e	-758	-707	-1554	-330	-1088	-1004
150	-176	-71	-418		-737	-620	-1925	-162	-1234	-1164
160	-45	-216	238		-627	-259	-2687	342	-1442	-1522
165							-5213			
170										
175										
180										
183										



# STRAIN GAGE DATA FROM COMPOSITE CYLINDER HYDROSTATIC TEST.

cylinder # 17      layup [902/(+\_30)2]s      test date 11/8/91

## 1. Raw Circumferential Strain Gage Data.

Pres	A*	B*	C	D	E	F	G	H	J	K
0	-49	-146	-42	-16	-15	8	-13	-47	-31	-42
25	-92	-192	-415	-237	-132	-350	-161	-557	-210	-226
50	-131	-211	-1322	-355	-279	-476	-264	-332	-327	-367
0	30	-101	-642	-6	93	-26	52	-22	31	-13
25	-94	-170	-1210	-226	-113	-255	-143	-692	-178	-203
50	-152	-211	-1477	-396	-257	-397	-277	-323	-340	-413
75	-162	-234	-1643	-522	-414	-582	-391	-412	-484	-448
100	-192	-262	-1839	-650	-598	-748	-518	-571	-638	-543
110	-197	-267	-1937	-697	-698	-827	-573	-641	-713	-600
120	-208	-274	-2009	-721	-768	-880	-603	-692	-759	-629
130	-212	-277	-2061	-752	-839	-941	-643	-751	-810	-665
140	-240	-281	-2173	-789	-974	-1005	-706	-848	-878	-726
150	-251	-268	-2228	-785	-1052	-1026	-731	-912	-902	-782
160	-285	-256	-2338	-763	-1191	-1068	-769	-1026	-907	-839
170	-368	-191	-2508	-635	-1476	-1077	-791	-1280	-794	-976
175	-418	-112	-2589	-470	-1708	-1013	-774	-1506	-602	-1104
180	-686	227	-2761	100	-2483	-671	-704	-2285	1062	-1606
183					-2825					

## 2. Intercept at P=0 using values at 25 and 50 psi.

	A*	B*	C	D	E	F	G	H	J	K
INT	-36	-129	-943	-56	31	-113	-9	-61	-16	7
								(-192@25)		

## 3. Zeroed Circumferential Strain Data (using intercept).

Pres	A*	B*	C	D	E	F	G	H	J	K
0	0	0	0	0	0	0	0	0	0	0
25	-56	-63	528	-181	-163	-237	-152	-496	-194	-233
50	-95	-82	-379	-299	-310	-363	-255	-271	-311	-374
0	0	0	0	0	0	0	0	0	0	0
25	-58	-41	-267	-170	-144	-142	-134	-131	-162	-210
50	-116	-82	-534	-340	-288	-284	-268	-262	-324	-420
75	-126	-105	-700	-466	-445	-469	-382	-351	-468	-455
100	-156	-133	-896	-594	-629	-635	-509	-510	-622	-550
110	-161	-138	-994	-641	-729	-714	-564	-580	-697	-607
120	-172	-145	-1066	-665	-799	-767	-594	-631	-743	-636
130	-176	-148	-1118	-696	-870	-828	-634	-690	-794	-672
140	-204	-152	-1230	-733	-1005	-892	-697	-787	-862	-733
150	-215	-139	-1285	-729	-1083	-913	-722	-851	-886	-789
160	-249	-127	-1395	-707	-1222	-955	-760	-965	-891	-846
170	-332	-62	-1565	-579	-1507	-964	-782	-1219	-778	-983
175	-382	17	-1646	-414	-1739	-900	-765	-1445	-586	-1111
180	-650	356	-1818	156	-2514	-558	-695	-2224	1078	-1613
183					-2856					



# STRAIN GAGE DATA FROM COMPOSITE CYLINDER HYDROSTATIC TEST.

cylinder # 18                      layup [902/(+\_30)2]s                      test date 12/11/91

## 1. Raw Circumferential Strain Gage Data.

Pres	A*	B*	C	D	E	F	G	H	J	K
0	-10	-6	4	2	3	2	-3	-8	3	7
25	-61	-42	-26	-106	-285	79	-153	-155	-143	-164
50	-82	-65	-112	-160	-580	1260	-306	-306	-259	-296
75	-117	-83	-259	-186	-914	1100	-447	-448	-348	-414
100	-161	-94	-427	-179	-1298	1000	-588	-609	-425	-536
110	-177	-87	-509	-145	-1485	993	-634	-678	-433	-566
120	-203	-78	-602	-104	-1691	975	-677	-762	-445	-612
130	-241	-64	-709	-32	-1929	969	-711	-867	-439	-661
140	-293	-46	-841	69	-2221	967	-733	-1011	-416	-721
150	-366	-15	-999	229	-2576	976	-724	-1199	-351	-784
160	-485	71	-1249	545	-3111	1009	-631	-1541	-191	-869
170	-787	263	-1815	1314	-4174	1067	-269	-2385	280	-976
175					-5200					

## 2. Intercept at P=0 using values at 25 and 50 psi.

	A*	B*	C	D	E	F	G	H	J	K
INT	-40	-19	60	-52	10	-1102	0	-4	-27	-32

## 3. Zeroed Circumferential Strain Data (using intercept).

Pres	A*	B*	C	D	E	F	G	H	J	K
0	0	0	0	0	0	0	0	0	0	0
25	-21	-23	-86	-54	-295	1181	-153	-151	-116	-132
50	-42	-46	-172	-108	-590	2362	-306	-302	-232	-264
75	-77	-64	-319	-134	-924	2202	-447	-444	-321	-382
100	-121	-75	-487	-127	-1308	2102	-588	-605	-398	-504
110	-137	-68	-569	-93	-1495	2095	-634	-674	-406	-534
120	-163	-59	-662	-52	-1701	2077	-677	-758	-418	-580
130	-201	-45	-769	20	-1939	2071	-711	-863	-412	-629
140	-253	-27	-901	121	-2231	2069	-733	-1007	-389	-689
150	-326	4	-1059	281	-2586	2078	-724	-1195	-324	-752
160	-445	90	-1309	597	-3121	2111	-631	-1537	-164	-837
170	-747	282	-1875	1366	-4184	2169	-269	-2381	307	-944
175					-5210					



# STRAIN GAGE DATA FROM COMPOSITE CYLINDER HYDROSTATIC TEST.

cylinder # 23                      layup [902/0]4t                      test date 11/22/91

## 1. Raw Circumferential Strain Gage Data.

Pres	A*	B*	C	D	E	F	G	H	J	K
0	5	-331	10	-4	28	26	11	-9	5	-6
25	-96	-414	-82	-92	-96	107	-99	-89	-134	-76
50	-147	-471	-88	-218	-175	81	-163	-119	-241	-112
75	-191	-529	-68	-321	-254	5	-245	-144	-387	-142
100	-199	-581	-104	-436	-303	-77	-312	-137	-601	-139
110	-199	-601	-126	-480	-299	-97	-329	-106	-686	-99
120	-211	-635	-171	-565	-273	-143	-346	-55	-805	-33
130	-188	-661	-203	-645	-209	-233	-363	25	-1037	76
140	-131	-729	-332	-857	50	-488	-350	263	-1524	430
150	59	-926	-834	-1306	1028	-1305	-107	849	-2559	1362
152									-4400	

## 2. Intercept at P=0 using values at 25 and 50 psi.

	A*	B*	C	D	E	F	G	H	J	K
INT	-45	-357	-76	34	-17	133	-35	-59	-27	-40

## 3. Zeroed Circumferential Strain Data (using intercept).

Pres	A*	B*	C	D	E	F	G	H	J	K
0	0	0	0	0	0	0	0	0	0	0
25	-51	-57	-6	-126	-79	-26	-64	-30	-107	-36
50	-102	-114	-12	-252	-158	-52	-128	-60	-214	-72
75	-146	-172	8	-355	-237	-128	-210	-85	-360	-102
100	-154	-224	-28	-470	-286	-210	-277	-78	-574	-99
110	-154	-244	-50	-514	-282	-230	-294	-47	-659	-59
120	-166	-278	-95	-599	-256	-276	-311	4	-778	7
130	-143	-304	-127	-679	-192	-366	-328	84	-1010	116
140	-86	-372	-256	-891	67	-621	-315	322	-1497	470
150	104	-569	-758	-1340	1045	-1438	-72	908	-2532	1402
152									-4373	



## APPENDIX E

### ABD STIFFNESS MATRICES



" 6.

[(90)4/(0)2]s; r = 2.755", l = 18"

Buckling Pressure for a cylinder with dimensions of:

r = 2.75, l = 18.00, t = 0.0720 => Z = 1633. , r/t = 38.

and a load ratio of: Ny = 2.00 Nx = 1.00

Pcr = 218.2 Nx = 300.6 M = 1 N = 2  
ABAQUS Pcr = 242.5

ABD Matrix:

5.3129E+05	3.0428E+04	0.0000	0.0000	0.0000	0.0000
3.0428E+04	9.5390E+05	0.0000	0.0000	0.0000	0.0000
0.0000	0.0000	7.2000E+04	0.0000	0.0000	0.0000
-----					
0.0000	0.0000	0.0000	67.23	13.15	0.0000
0.0000	0.0000	0.0000	13.15	574.4	0.0000
0.0000	0.0000	0.0000	0.0000	0.0000	31.10

[(90)3/(0)3]s; r = 2.755", l = 18"

Buckling Pressure for a cylinder with dimensions of:

r = 2.75, l = 18.00, t = 0.0720 => Z = 1633. , r/t = 38.

and a load ratio of: Ny = 2.00 Nx = 1.00

Pcr = 236.6 Nx = 325.9 M = 1 N = 2  
ABAQUS Pcr = 230.5

ABD Matrix:

7.4260E+05	3.0428E+04	0.0000	0.0000	0.0000	0.0000
3.0428E+04	7.4260E+05	0.0000	0.0000	0.0000	0.0000
0.0000	0.0000	7.2000E+04	0.0000	0.0000	0.0000
-----					
0.0000	0.0000	0.0000	115.4	13.15	0.0000
0.0000	0.0000	0.0000	13.15	526.2	0.0000
0.0000	0.0000	0.0000	0.0000	0.0000	31.10

[(90)2/(130)2]s; r = 2.755", l = 18"

Buckling Pressure for a cylinder with dimensions of:

r = 2.75, l = 18.00, t = 0.0720 => Z = 1633. , r/t = 38.

and a load ratio of: Ny = 2.00 Nx = 1.00

Pcr = 206.6 Nx = 284.6 M = 1 N = 3  
ABAQUS Pcr = 205.4

ABD Matrix:

6.0055E+05	1.7247E+05	0.0000	0.0000	0.0000	0.0000
1.7247E+05	6.0055E+05	0.0000	0.0000	0.0000	0.0000
0.0000	0.0000	2.1404E+05	0.0000	0.0000	0.0000
-----					
0.0000	0.0000	0.0000	141.4	40.42	19.08
0.0000	0.0000	0.0000	40.42	445.7	7.271
0.0000	0.0000	0.0000	19.08	7.271	58.38



Buckling Pressure for a cylinder with dimensions of:

$r = 2.75$ ,  $l = 18.00$ ,  $t = 0.0720 \Rightarrow Z = 1633.$ ,  $r/t = 38.$   
and a load ratio of:  $N_y = 2.00$   $N_x = 1.00$

Pcr = 184.1      Nx = 253.7      M = 1      N = 3  
ABAQUS Pcr = 178.8

ABD Matrix:

5.3129E+05	3.0428E+04	0.0000	2536.	0.0000	0.0000
3.0428E+04	9.5390E+05	0.0000	0.0000	-2536.	0.0000
0.0000	0.0000	7.2000E+04	0.0000	0.0000	0.0000
-----					
2536.	0.0000	0.0000	234.6	13.15	0.0000
0.0000	-2536.	0.0000	13.15	407.0	0.0000
0.0000	0.0000	0.0000	0.0000	0.0000	31.10

Jones [90,90,90,60,30,0,0,15,30,60,75,90];  $r = 2.755$ ,  $l = 18$

Buckling Pressure for a cylinder with dimensions of:

$r = 2.75$ ,  $l = 18.00$ ,  $t = 0.0720 \Rightarrow Z = 1633.$ ,  $r/t = 38.$   
and a load ratio of:  $N_y = 2.00$   $N_x = 1.00$

Pcr = 235.9      Nx = 324.9      M = 1      N = 3  
ABAQUS Pcr = 213.4

ABD Matrix:

5.5408E+05	1.1329E+05	1.1791E+05	1286.	426.1	565.4
1.1329E+05	7.6539E+05	1.1791E+05	426.1	-2138.	934.5
1.1791E+05	1.1791E+05	1.5486E+05	565.4	934.5	426.1
-----					
1286.	426.1	565.4	83.12	35.45	22.95
426.1	-2138.	934.5	35.45	513.9	43.62
565.4	934.5	426.1	22.95	43.62	53.40











Thesis

M5933 Miller

c.1      Hydrostatic testing and  
analysis of graphite-epoxy  
cylinders.

Thesis

M5933 Miller

c.1      Hydrostatic testing and  
analysis of graphite-epoxy  
cylinders.

DUDLEY KNOX LIBRARY



3 2768 00036347 7